



DESIGN AND OPTIMIZATION OF LATTICE STRUCTURES FOR AEROSPACE APPLICATIONS

Enrico Stragiotti

François-Xavier Irisarri¹, Cédric Julien¹ and Joseph Morlier²

1: ONERA - The French Aerospace Lab
DMAS - Département matériaux et structures
92320 Châtillon, France
{francois-xavier.irisarri, cedric.julien}@onera.fr

2: ICA - Institut Clément Ader
ISAE - SUPAERO
31400 Toulouse, France
joseph.morlier@isae-supraero.fr
November 17, 2023

PhD manuscript

ONERA – ISAE Supaero

Colophon

This document was typeset with the help of KOMA-Script and L^AT_EX using the kaobook class.

ONERA – ISAE Supaero

CONTENTS

Contents	iii
List of Figures	v
List of Tables	vii
List of Abbreviations	ix
1 Evaluating discretization approaches for ultralight structure optimization	1
1.1 The formulation of a common problem: volume minimization with stress constraints	1
1.1.1 Continuous discretization Nested Analysis and Design (NAND) minimum volume formulation	2
1.1.2 Truss discretization Simultaneous Analysis and Design (SAND) minimum volume formulation	11
1.2 Comparison between continuous and truss discretization	13
1.2.1 Definition of a common test case	14
1.2.2 Numerical application	15
1.2.3 Discussion	20
1.3 Conclusion	23
2 Enriching the classic TTO formulation with advanced mechanical constraints	25
2.1 Advanced mechanical constraints	25
2.1.1 Minimum slenderness constraints	26
2.1.2 Local and topological buckling constraints	27
2.1.3 Kinematic compatibility constraints	29
2.2 Optimization formulation and solving strategy	30
2.2.1 Optimization strategy	31
2.2.2 First step: SLP optimization	31
2.2.3 Handling local minima: reinitialization strategy	33
2.2.4 Second step: NLP optimization	35
2.3 Numerical application	36
2.3.1 L-shaped beam	37
2.3.2 Ten-bar truss	39
2.3.3 2D cantilever beam	42
2.3.4 Simply supported 3D beam	45
2.3.5 Ten-bar truss with multiple load cases	47
2.4 Conclusion	50
3 Optimizing modular structures	51
3.1 Formulation of a modular structure optimization algorithm	51
3.1.1 Variable linking	51
3.1.2 Topological buckling of modular structures	53
3.1.3 Optimization formulation	53

3.1.4	Sensitivity analysis	55
3.2	Numerical application	56
3.2.1	On the equivalence of multi-load cases and modular structures	56
3.2.2	Parametric study on the number of subdomains and the complexity of the module	58
3.2.3	Comparison with the optimized octet-truss	66
3.2.4	Using multiple module topologies	71
3.3	Conclusion	74
	Bibliography	77

LIST OF FIGURES

1.1	The domain Ω is discretized using $N_e = N_x N_y$ continuous 4-nodes elements.	2
1.2	Kernel of the 2D convolution operator.	4
1.3	A four-node quadrilateral element. GP is the Gaussian integration point for which the equivalent stress is evaluated.	6
1.4	The domain Ω is discretized using a set of straight members connecting a set of nodes. This framework is known as the ground structure.	12
1.5	The optimal structures found by layout optimization tend at Michell-like structures, made up of a very large number of infinitesimal struts [38].	13
1.6	On the left, plot of the L-shape beam test case, on the right the graphical representations of the two discretizations used, the continuous (above) and the truss-like (below).	14
1.7	(a-d) topology optimized structures for different material admissibles $\sigma_L = 10.00, 2.00, 0.40$ and 0.25 , showing a volume fraction of $V_f = 1.60\%, 4.04\%, 18.03\%$ and 34.71% , respectively. (e-h) Von Mises stress distribution of the optimized structures.	16
1.8	The optimized structure for $\sigma_L = 0.2$ with $V_f = 48.08\%$, but does not converge after 7500 iterations.	17
1.9	The optimized structure for $\sigma_L = 10.0$ with $V_f = 1.60\%$. Some of the structure's features present not even a fully-dense element in their thickness.	18
1.10	Linear (a) and logarithmic (b) plot of the volume fraction V_f and the compliance C with respect to the maximum material admissible σ_L for the continuous mesh structures. Areas in red represent the boundaries of the applied method.	18
1.11	Topology (a) and stress (b) plot for the truss-like discretization.	19
1.12	Optimized structure obtained a fully connected ground structure with 13×13 and 7705 candidates.	19
1.13	Linear (a) and logarithmic (b) plot of the volume fraction V_f and the compliance C with respect to the maximum material admissible σ_L for the truss-like structures. Areas in red represent the boundaries of the applied method.	20
1.14	Compliance – Maximum material admissible plot for the continuous and truss discretizations.	21
1.15	Maximum material admissible – Volume fraction plot for the continuous and truss discretizations.	21
1.16	Compliance – Volume fraction plot for the continuous and truss discretizations.	22
1.17	Time – Volume fraction plot for the continuous and truss discretizations.	22
2.1	The three ground structures loaded in compression are used to highlight the topological buckling problem in Truss Topology Optimization (TTO). (a) Two-bar ground structure loaded in compression; (b) single bar ground structure; (c) overlap of the a and b ground structures.	28
2.2	Flowchart of the two-step optimization strategy used to solve Problem \mathbb{P}_1	32
2.3	Linearization of the local buckling constraints for a single bar.	33

2.4	The linearized buckling constraints (blue dashed line) limit the design space of successive iterations when evaluated on compressive bars with very small areas. Additionally, the gradient of the linearized buckling constraint tends to 0.	33
2.5	The reinitialization strategy modifies the linearization point of the members with a small area to promote their reintroduction in the optimization problem.	34
2.6	Flowchart of the Sequential Linear Programming (SLP) strategy with reinitialization used to solve Problem \mathbb{P}_2	35
2.7	Topology of the optimized truss structures for different material admissibles $\sigma_L = 1.0, 0.8, 0.3$ and 0.2 with a minimum slenderness limit $\lambda < 15$	38
2.8	The ten-bar truss ground structure and load case.	39
2.9	Scatter plot of the four benchmarked optimization algorithms on the ten-bar truss. The 2S-5R shows a 100 % convergence rate to the lightest structure found. The dashed lines represent the mean of the distributions.	40
2.10	Volume convergence history for the proposed two-step resolution strategy with one step of reinitialization (2S-1R) for the initialization point a_s^0 . The reinitialization strategy permits to jump from the local minimum (b), with $V = 87857$, to the lighter structure (d), with $V = 85534$. Only the SLP step is plotted because the solution is statically determinate and kinematic compatibility constraints are already satisfied. In red the members loaded in tension, in blue the members loaded in compression.	41
2.11	The 2D cantilever beam load case with a first-order connectivity ground structure. The total number of candidate members is $N_{el} = 90$	42
2.12	(a) Non-Linear Programming (NLP) optimized design of the 2D cantilever beam with a volume of $V = 80.67$ and high number of active and crossing bars $N_{el} = 66$; (b) 2S-5R solution $V = 77.78$ with $N_{el} = 31$. In red the members loaded in tension, in blue the members loaded in compression.	43
2.13	Left: scatter plot of three of the four benchmarked optimization algorithms on the 2D cantilever beam compared to the solution by Achtziger [61]. The dashed lines represent the mean of distributions. Right: histogram of the distribution of the results of the optimization algorithms.	44
2.14	The simply supported 3D beam example with the load case and boundary conditions. In blue we plot the symmetry planes.	45
2.15	Ground structure composed of $N_{el} = 496$ elements of the symmetric portion used to optimize the simply supported 3D beam.	45
2.16	Orthographic views of the topology of the optimized simply supported 3D beam. (a) XZ plane (b) YZ plane (c) XY plane (d) auxiliary perspective view.	46
2.17	Maximum stress constraint value (a) and buckling constraint value (b) plotted on the optimized topology of the simply supported 3D beam.	46
2.18	Ground structure of the ten-bar truss with two applied load cases P_1 and P_2	47
2.19	Maximum stress constraint value (left) and buckling constraint value (right) plotted on the optimized design of the multiple load cases ten-bar truss.	48
2.20	Iteration history of the ten-bar truss with multiple load cases example solved with the 2S-5R algorithm; (a) objective function history for the SLP and NLP step (b) constraint violation for the NLP step.	50

3.1	Notations used for the definition of the variable linking approach used to apply the modularity constraints.	52
3.2	Notations used for the evaluation of the sensitivities for the modular structure optimization based on the variable linking scheme.	56
3.3	Boundary conditions of the multi-subdomains (a) and the multi-load cases (b) test cases.	57
3.4	Optimized structures of the multi-subdomains (a) and the multi-load cases (b) test cases. The resulting module topology is equal for the two cases. In red the bars are in a tensile state, and in blue the bars are in a compressive state.	58
3.5	Symmetric boundary conditions of the simply supported 3D beam. In gray are the symmetry planes of the test case.	58
3.6	Perspective view of the monolithic simply supported 3D beam optimized structure with $V = 9.907 \text{ cm}^3$	58
3.7	Influence of the number of subdomains on the volume of the optimized modular structure.	59
3.8	Influence of the number of subdomains on the computational time of the optimization.	59
3.9	Rendering of the optimized structures with $6 \times 2 \times 3$ (a-e), $12 \times 4 \times 6$ (b-f), $18 \times 6 \times 9$ (c-g), and $30 \times 10 \times 15$ (d-h) subdomains. The module presents a $2 \times 2 \times 2$ complexity.	61
3.10	Influence of the number of subdomains on the loading metrics φ and ψ of the optimized structures.	61
3.11	Stress (a-c) and local buckling (b-d) failure criteria plotted on the monolithic and the $12 \times 4 \times 6 - 3 \times 3 \times 3$ cases.	62
3.12	Rendering of the optimized structures with $2 \times 2 \times 2$ (a-e), $3 \times 3 \times 3$ (b-f), $4 \times 4 \times 4$ (c-g), and $5 \times 5 \times 5$ (d-h) module complexity. The number of subdomains is $6 \times 2 \times 3$	63
3.13	Influence of the module complexity on the volume of the optimized modular structure.	64
3.14	Influence of the module complexity on the computational time of the optimization. . .	64
3.15	Influence of the module complexity on the loading metrics φ and ψ of the optimized structures.	64
3.16	Design of experiments (DOE) response curves and isocurves plot for the volume (a-b) and computational time (c-d).	67
3.17	Main effects plot of volume (a) and computational time (b).	68
3.18	Rendering of a single octet-truss module.	69
3.19	Comparison of the octet-truss structures (a-c-e-g) and the TTO structures (b-d-f-h) for two different numbers of submodules, $6 \times 2 \times 3$ and $12 \times 4 \times 6$	70
3.20	Graphical representation of the given module layout for the simply supported 3D beam.	71
3.21	Orthographic views of the topology of the optimized modular simply supported 3D beam. (a) XZ plane (b) YZ plane (c) XY plane (d) auxiliary perspective view.	72
3.22	Comparison of the volume and computational time of the structure with multiple modules with the monolithic and the fully modular structures.	72
3.23	Stress (a-c) and local buckling (b-d) failure criteria plotted on the multiple and single module modular structures.	73

LIST OF TABLES

1.1	Material data used for the optimizations. The value of the maximum material admissible σ_L is used as the parameter to generate multiple optimized topologies.	15
1.2	Numerical results of the topology optimization method of the L-shape beam load case with varying material admissible σ_L on a 600×600 elements mesh.	17
1.3	Numerical results of the TTO method of the L-shape beam load case with varying material admissible σ_L on a 33×33 ground structure.	19
2.1	Non-exhaustive list of the existing research in Truss Topology Optimization (TTO) with their corresponding scientific contributions.	26
2.2	Values and description of the parameters used for the SLP and NLP optimizations.	38
2.3	Numerical comparison of the effect of the minimum slenderness constraint on the optimization of the 2D L-shaped beam.	39
2.4	Material data used for the ten-bar truss optimization.	39
2.5	Numerical comparison of the four optimization algorithms on the ten-bar truss for 50 different initial points. The 2S-5R algorithm shows a 100 % convergence rate to the lightest structure found. The iteration count and time are from the first initialization point a_s^0	40
2.6	Material data used for the 2D cantilever beam optimization.	42
2.7	Numerical comparison of the 2D cantilever beam of the four algorithms for 100 random initial points. The 2S-5R algorithm shows a good balance between the volume, complexity, and dispersion of the solutions.	43
2.8	Optimal values of the member forces, areas, and volumes of the 2D cantilever beam.	43
2.9	Material data used for the simply supported 3D beam optimization.	45
2.10	Numerical results of the optimization of the simply supported 3D beam.	46
2.11	Numerical comparison of the four optimization algorithms on the ten-bar truss for 50 different initial points.	47
2.12	Comparison of the results of the SLP step and NLP step for the multiple load cases ten-bar truss.	49
2.13	Optimal values of the member forces, areas, and volumes of the members of the ten-bar truss with multiple load cases.	49
3.1	Reminder of the parameters used to set the reinitialization parameters for the modular optimization. The full list of values and tolerances used for the setup of the optimization algorithm can be found in Table 2.2.	56
3.3	57
3.2	Material data used for the modular bridge section 2D structure.	57
3.4	Material data used for the simply supported 3D beam optimization.	58
3.5	Numeric results of the parametric study on the influence of the number of subdomains on the optimized structures.	60
3.6	Numeric results of the parametric study on the influence of the module complexity on the optimized structures.	63
3.7	Coefficients of the quadratic function used to model how the volume V varies with the number of subdomains N_{sub} and the module complexity \bar{n}	65
3.8	Coefficients of the quadratic function used to model how the computational time t varies with the number of subdomains N_{sub} and the module complexity \bar{n}	65
3.9	Numerical results of the comparison between octet-truss and TTO structures.	69

3.10 Numerical results of the comparison between the structure with multiple modules with the monolithic and the fully-modular structures.	74
--	----

LIST OF ABBREVIATIONS

CRM	NASA Common Research Model
DOE	Design of experiments
DOFs	Degrees Of Freedom
DSI	Degree of Static Indeterminacy
FEA	Finite Element Analysis
HS	Hashin-Shtrikman
KS	Kreisselmeier-Steinhauser
LP	Linear Programming
MMA	Method of Moving Asymptotes
MPVCs	Mathematical Programs with Vanishing Constraints
NAND	Nested Analysis and Design
NLP	Non-Linear Programming
RVE	Representative Volume Element
SAND	Simultaneous Analysis and Design
SIMP	Solid Isotropic Material with Penalization Method
SLA	Stereolithography
SLP	Sequential Linear Programming
TTO	Truss Topology Optimization

EVALUATING DISCRETIZATION APPROACHES FOR ULTRALIGHT STRUCTURE OPTIMIZATION

1

The process of topology optimization for a structure involves the selection and sizing of optimal elements within a predetermined set. As discussed in the previous chapter, in our context this set could be composed of either continuum elements (shell or volumetric) or truss-like elements. This chapter aims to assess the suitability and the inherent advantages and disadvantages of both methodologies when optimizing ultralight structures i.e. structures that exhibit an extremely low volume fraction, typically below 1%.

For this purpose, we initially establish a common optimization formulation in Section 1.1. The classic compliance minimization with volume constraint problem is reformulated as a volume minimization problem with maximum stress constraints for both discretizations. Later, this framework is applied to optimize a two-dimensional test case, featuring identical dimensions, loads, and material properties. The outcomes of the comparison of both discretization approaches are presented and discussed in Section 1.2.

1.1 THE FORMULATION OF A COMMON PROBLEM: VOLUME MINIMIZATION WITH STRESS CONSTRAINTS

Two of the most frequently employed formulations for structural optimization are the minimization of volume while adhering to stress constraints and the minimization of compliance under volume constraints. Historically, the volume minimization formulation has been used in the first works of structural optimization of truss structures [2–4]. The problem was initially formulated in terms of member forces, ignoring the kinematic compatibility to obtain a Linear Programming (LP) problem. The formulation was modeled using the Simultaneous Analysis and Design (SAND) approach, where the equations of nodal equilibrium are treated as equality constraints, and where both nodal displacements and the cross-sectional areas of truss members serve as design variables [5].

However, to attain greater design freedom, the structure optimization field later transitioned from truss structures to continuous discretization. While truss structures offered simplicity and ease of analysis, they imposed limitations on design due to their discrete member configurations. The continuum mesh offered instead more versatility [6, 7], and has since been used for multiple different applications, e.g. the design of metamaterials [8, 9] or the simulation of advanced manufacturing constraints [10, 11]. The Simultaneous Analysis and Design (SAND) approach is incompatible with continuum meshes

1.1 THE FORMULATION OF A COMMON PROBLEM: VOLUME MINIMIZATION WITH STRESS CONSTRAINTS 1

1.2 COMPARISON BETWEEN CONTINUOUS AND TRUSS DISCRETIZATION 13

1.3 CONCLUSION 23

Part of the content presented in this chapter has been published and showcased during a conference as:
Stragiotti, E. et al. (2021) "Towards manufactured lattice structures: a comparison between layout and topology optimization", in *AeroBest 2021 International Conference on Multidisciplinary Design Optimization of Aerospace Systems*. Book of proceedings. Lisbon, Portugal: ECCOMAS [1].

2. Dorn et al. (1964), 'Automatic design of optimal structures'

3. Chan (1964), 'Optimum structural design and linear programming'

4. Hemp (1973), 'Optimum Structures'

5. Sankaranarayanan et al. (1994), 'Truss topology optimization with simultaneous analysis and design'

6. Bendsøe et al. (1988), 'Generating optimal topologies in structural design using a homogenization method'

7. Bendsøe (1989), 'Optimal shape design as a material distribution problem'

8. Sigmund (1994), 'Materials with prescribed constitutive parameters'

9. Zhang et al. (2006), 'Scale-related topology optimization of cellular materials and structures'

10. Sigmund (2009), 'Manufacturing tolerant topology optimization'

11. Brackett et al. (2011), 'Topology Optimization for Additive Manufacturing'

1: This preposition holds when referring to the end of the 1980s when computational power was scarce compared to what we have today.

- 12. Tortorelli et al. (1994), 'Design sensitivity analysis'
- 13. Martins et al. (2021), 'Engineering Design Optimization'
- 14. Bendsøe et al. (2004), 'Topology Optimization'

due to its excessive number of variables¹. Given this limitation, a new approach was required to better handle the complexity of continuum meshes.

In the Nested Analysis and Design (NAND) approach, the nodal displacement (state) variables are eliminated from the optimization problem through a process where the structural equilibrium equation is solved every iteration instead of being used as a constraint of the optimization. This results in an independent nested phase where the state equation of structural equilibrium is solved separately from the optimization algorithm. This creates a dense coupling between displacement and material density variables, necessitating a computationally expensive sensitivity analysis within the nested algorithm, typically employing the adjoint method (more information about the adjoint method on the following resources [12, 13]). Nevertheless, if the problem is reformulated as a compliance minimization with volume constraints, the problem is self-adjoint and the adjoint algorithm is no longer necessary to evaluate the gradient sensitivities [14].

However, our emphasis on operating within the aerospace sector aligns more favorably with the volume minimization problem. The choice to prioritize volume minimization in the aerospace sector is underpinned by a range of economic, environmental, and performance-related factors. It is a strategic approach that aligns with industry goals of sustainability, efficiency, and technological advancement. Additionally, as we will see later in this thesis, the volume minimization formulation will permit adding local buckling and maximum displacement constraints more easily. We have opted, thus, to employ the volume minimization optimization formulation for our study, and we will now review how this formulation is implemented on continuum and truss-like meshes.

1.1.1 CONTINUOUS DISCRETIZATION NESTED ANALYSIS AND DESIGN (NAND) MINIMUM VOLUME FORMULATION

This section introduces the NAND volume minimization formulation of topology optimization for continuum meshes. We will start however presenting the more common minimum compliance formulation to explain the important notations and concepts that will be essential in developing the volume minimization formulation.

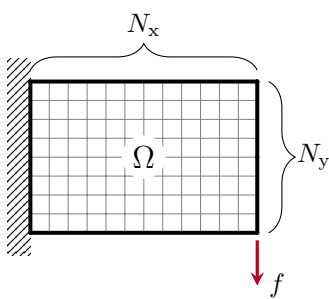


Figure 1.1: The domain Ω is discretized using $N_e = N_x N_y$ continuous 4-nodes elements.

MINIMUM COMPLIANCE FORMULATION Let $\Omega \in \mathbb{R}^2$ be a rectangular domain in of dimensions X and Y , containing respectively N_x and N_y linear 4-nodes elements, for a total of $N_e = N_x N_y$ elements and M nodes (see Fig. 1.1). The objective of the optimization is the minimization of the compliance C of the structure, equivalent to finding the structure with the least possible nodal displacement with

respect to a defined set of boundary conditions. The Problem \mathbb{T}_0 is stated in terms of the design variables ρ as follows:

$$\begin{aligned} \min_{\rho} \quad & C = \sum_i \mathbf{u}_{e,i}^T \mathbf{K}_{e,i} \mathbf{u}_{e,i} = \mathbf{f}^T \mathbf{u} \quad \forall i \in [0, \dots, N_e] \\ \text{s.t.} \quad & \frac{\sum_i (\bar{\rho}_i v_i) / V_0}{V_p} - 1 \leq 0 \quad \forall i \in [0, \dots, N_e] \quad (\mathbb{T}_0) \\ & \mathbf{K}\mathbf{u} = \mathbf{f} \\ & 0 \leq \rho_i \leq 1. \quad \forall i \in [0, \dots, N_e] \end{aligned}$$

The design variables ρ are defined for every element of the structure as $\rho = [\rho_1, \rho_2, \dots, \rho_{N_e}]^T$, with $\rho_i \in [0, 1]$, $\forall i \in [0, \dots, N_e]$. The physical densities $\bar{\rho}$ are related to design variables through density filtering and threshold projection [15], as explained later in the document. V_p is the prescribed volume fraction that acts as the constraint of the minimization problem, while v_i represents the area of the i -th element and V_0 is the total area of the domain Ω . $\mathbf{K}\mathbf{u} = \mathbf{f}$ is the state equation of the problem and defines the elastic response of the structure to an external nodal load $\mathbf{f} = [f_1, f_2, \dots, f_{2M}]^T$. The global stiffness matrix \mathbf{K} is assembled from the element stiffness matrix $\mathbf{K} = \sum_{i \in \Omega} \mathbf{K}_{e,i}$ and $\mathbf{K}_{e,i} = E_i \mathbf{K}_{e,0}$ where $\mathbf{K}_{e,0}$ represents the element stiffness matrix relative to the chosen type of element (linear or quadratic) and $E_i(\bar{\rho}_i)$ the Young's modulus of the i -th element.

The material scheme used to interpolate between void and full material is the well-known Solid Isotropic Material with Penalization Method (SIMP) [7, 16] approach. It is governed by the equation:

$$E_i(\bar{\rho}_i) = E_{\min} + \bar{\rho}_i^p (E_0 - E_{\min}), \quad (1.1)$$

where the parameter p penalizes the intermediate densities and pushes the result to a black-and-white result. E_0 is the Young's modulus of the dense material and E_{\min} is a small value used to avoid the global stiffness matrix \mathbf{K} from being singular when $\bar{\rho}_i = 0$.

In this study we set these parameters to $E_0 = 1$, and $E_{\min} = 10^{-9}$. The value of the penalization parameter p is selected as $p = 3$ because in that way the intermediate densities respect the Hashin-Shtrikman (HS) bounds [16, 17]. These relationships describe the boundaries of attainable isotropic material characteristics when dealing with composites (materials with microscopic structures) using two specified, linearly elastic, isotropic materials (in our case the solid and the empty phases).

SPATIAL FILTERING AND PROJECTION Multiple approaches have been developed to solve the problems linked to mesh discretization, such as mesh dependence or the checkerboard problem [18]. Filtering

15. Wang et al. (2011), 'On projection methods, convergence and robust formulations in topology optimization'

7. Bendsøe (1989), 'Optimal shape design as a material distribution problem'

16. Bendsøe et al. (1999), 'Material interpolation schemes in topology optimization'

17. Hashin et al. (1963), 'A variational approach to the theory of the elastic behaviour of multiphase materials'

18. Díaz et al. (1995), 'Checkerboard patterns in layout optimization'

19. Sigmund (1994), 'Design of Material Structures using Topology Optimization'
 20. Sigmund (1997), 'On the Design of Compliant Mechanisms Using Topology Optimization'
 21. Sigmund (2007), 'Morphology-based black and white filters for topology optimization'

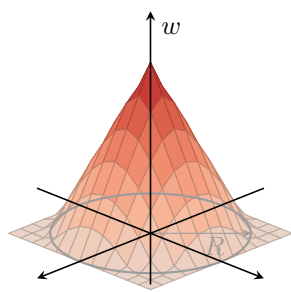


Figure 1.2: Kernel of the 2D convolution operator.

15. Wang et al. (2011), 'On projection methods, convergence and robust formulations in topology optimization'
 22. Ferrari et al. (2020), 'A new generation 99 line Matlab code for compliance topology optimization and its extension to 3D'

the sensitivity information of the optimization problem proved to be an effective approach to guarantee independence from mesh resolution [19, 20]. In the present research, we decided instead to directly filter the density field ρ using the 2D convolution operator [21]. The weight function w (or kernel) of the convolution is defined as:

$$w(d_j) = R - d_j, \quad j \in \mathbb{N}_{i,R} \quad (1.2)$$

where $\mathbb{N}_{i,R}$ represent the set of elements lying within a circle of radius R centered on the i -th element and d_j is the distance of the j -th element to the center of the filter (see Fig. 1.2).

The filtered values of the design variable are calculated as:

$$\tilde{\rho}_i = \frac{\sum_{j \in \mathbb{N}_{i,R}} w(d_j) v_j \rho_j}{\sum_{j \in \mathbb{N}_{i,R}} w(d_j) v_j}. \quad (1.3)$$

As the filtering phase produces a large number of gray elements, a smooth projection technique based on the \tanh function is implemented [15]:

$$\bar{\rho}_j = \frac{\tanh(\beta\eta) + \tanh(\beta(\tilde{\rho}_j - \eta))}{\tanh(\beta\eta) + \tanh(\beta(1 - \eta))}, \quad (1.4)$$

where β is a parameter that defines the slope of this approximation function: the larger the value of β , the less intermediate elements are present in the structure topology. η is the threshold value of the projection. Using Equation 1.4 is not volume conservative for all values of η , and to stay conservative we use a volume-increasing filter [22]. The value of $\eta = 0.4$ is then chosen.

The derivative of the filtered density $\tilde{\rho}$ with respect to the design variable ρ is written deriving Equation 1.3:

$$\frac{\partial \tilde{\rho}_i}{\partial \rho_j} = \frac{w(d_j) v_j}{\sum_{j \in \mathbb{N}_{i,R}} w(d_j) v_j}. \quad (1.5)$$

The sensitivity of the physical densities $\bar{\rho}$ with respect to the filtered $\tilde{\rho}$ can be written as:

$$\frac{\partial \bar{\rho}_j}{\partial \tilde{\rho}_j} = \beta \frac{1 - \tanh^2(\beta(\tilde{\rho}_j - \eta))}{\tanh(\beta\eta) + \tanh(\beta(1 - \eta))}. \quad (1.6)$$

Using the chain rule it is possible to write:

$$\frac{\partial h}{\partial \rho_i} = \sum_{j \in \mathbb{N}_{i,R}} \frac{\partial f}{\partial \bar{\rho}_j} \frac{\partial \bar{\rho}_j}{\partial \tilde{\rho}_j} \frac{\partial \tilde{\rho}_j}{\partial \rho_i}, \quad (1.7)$$

where h represents a generic function.

OBJECTIVE AND CONSTRAINT FUNCTIONS Up until this point, we have been focused on the compliance minimization formulation \mathbb{T}_0 . Moving forward, we introduce the necessary modifications to transition into the volume minimization formulation with stress constraints. This formulation will be used to compare the continuous mesh with truss-like structure optimization.

The objective of the optimization is to minimize the volume of a structure subject to a specified load case. The volume of the structure V is expressed as a fraction of the total volume V_0 of the domain Ω :

$$V = \frac{1}{V_0} \sum_{i \in \Omega} \bar{\bar{\rho}}_i v_i. \quad (1.8)$$

In this thesis, we assume that the elementary volume occupied by the i -th element v_i is equal for all the elements, and thus Equation 1.8 is simplified as follows:

$$V = \frac{1}{N_e} \sum_{i \in \Omega} \bar{\bar{\rho}}_i. \quad (1.9)$$

The normalized local stress constraint g_{st} are formulated as:

$$\frac{\sigma_{VM,i}}{\sigma_L} - 1 \leq 0, \quad \forall i \in \Omega_{mat}(\rho) \quad (g_{st})$$

where $\Omega_{mat}(\rho) \subseteq \Omega$ represents the design-dependent set of elements with a non-zero density, $\sigma_{VM,i}$ is the equivalent Von Mises stress for the i -th element, and σ_L is the maximum allowable of the material.

The first difficulty that arises is that the stress constraints are defined only for the elements where $\bar{\bar{\rho}}_i > 0$, while $\bar{\bar{\rho}}_i \in [0, 1]$. Thus, the set of constraints changes during the optimization. This class of problems is called Mathematical Programs with Vanishing Constraints (MPVCs) [23] and is known for being difficult to solve with a gradient descent optimization algorithm. The original set of constraints g_{st} is then reformulated into an equivalent design-independent set of constraints \bar{g}_{st} as follows [24]:

$$\bar{\bar{\rho}}_i \left(\frac{\sigma_{VM,i}}{\sigma_L} - 1 \right) \leq 0, \quad \forall i \in \Omega. \quad (\bar{g}_{st})$$

23. Achtziger et al. (2008), 'Mathematical programs with vanishing constraints'

24. Cheng et al. (1992), 'Study on Topology Optimization with Stress Constraints'

VON MISES STRESS EVALUATION The evaluation of the equivalent stress of an element follows the formulation proposed by Von Mises. Let us take a four-node quadrilateral linear element with a single integration (or Gauss) point in the center and four $2a$ equal-length sides (see Fig. 1.3). If bilinear shape functions are used to interpolate the displacement field, we can evaluate the deformations at the

integration point as:

$$\begin{pmatrix} \varepsilon_x \\ \varepsilon_y \\ \gamma_{xy} \end{pmatrix} = \mathbf{B}_s \mathbf{q}_s, \text{ with } \mathbf{B}_s = \frac{1}{4a} \begin{pmatrix} -1 & 1 & 1 & -1 & 0 & 0 & 0 & 0 \\ 0 & 0 & 0 & 0 & -1 & -1 & 1 & 1 \\ -1 & -1 & 1 & 1 & -1 & 1 & 1 & -1 \end{pmatrix}, \quad (1.10)$$

where $\mathbf{q}_s = (u_1, u_2, u_3, u_4, v_1, v_2, v_3, v_4)^T$ represents the vector of the displacement degrees of freedom of the element.

The stress tensor is evaluated using the elasticity Hooke's law in 2D as follows:

$$\begin{pmatrix} \sigma_x \\ \sigma_y \\ \tau_{xy} \end{pmatrix} = \mathbf{C}_e \begin{pmatrix} \varepsilon_x \\ \varepsilon_y \\ \gamma_{xy} \end{pmatrix} \quad \text{with} \quad \mathbf{C}_e = \frac{E}{1-\nu^2} \begin{pmatrix} 1 & \nu & 0 \\ \nu & 1 & 0 \\ 0 & 0 & G \end{pmatrix}. \quad (1.11)$$

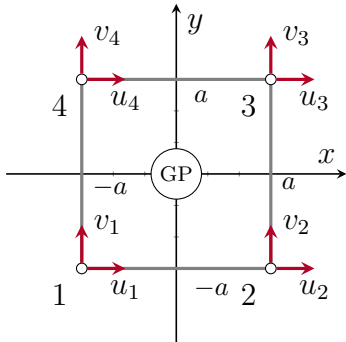


Figure 1.3: A four-node quadrilateral element. GP is the Gaussian integration point for which the equivalent stress is evaluated.

The equivalent Von Mises stress of the element can then be written as:

$$\langle \sigma_{VM} \rangle = \sqrt{\sigma_x^2 + \sigma_y^2 - \sigma_x \sigma_y + 3\tau_{xy}} \quad (1.12)$$

$$= \sqrt{(\sigma_x \ \sigma_y \ \tau_{xy}) \begin{pmatrix} 1 & -1/2 & 0 \\ -1/2 & 1 & 0 \\ 0 & 0 & 3 \end{pmatrix} \begin{pmatrix} \sigma_x \\ \sigma_y \\ \tau_{xy} \end{pmatrix}} \quad (1.13)$$

$$= \sqrt{\mathbf{q}_s^T \mathbf{B}_s^T \mathbf{C}_e^T \mathbf{D}_{VM} \mathbf{C}_e \mathbf{B}_s \mathbf{q}_s}, \text{ with } \mathbf{D}_{VM} = \begin{pmatrix} 1 & -1/2 & 0 \\ -1/2 & 1 & 0 \\ 0 & 0 & 3 \end{pmatrix} \quad (1.14)$$

$$\langle \sigma_{VM} \rangle = \sqrt{\mathbf{q}_s^T \mathbf{S} \mathbf{q}_s}, \quad \text{with } \mathbf{S} = \mathbf{B}_s^T \mathbf{C}_e^T \mathbf{D}_{VM} \mathbf{C}_e \mathbf{B}_s. \quad (1.15)$$

MICROSCOPIC AND MACROSCOPIC STRESS In stress-constrained topology optimization, the element stress is usually evaluated using the microscopic stress formulation, assuming that there is no direct correlation between stress and density [25]. Indeed, the use of the macroscopic stress in volume minimization optimization problems creates an all-void design [26]. The properties that the microscopic stress should present are:

- (i) The stress criterion should be mathematically as simple as possible, as the relationship between Young's modulus and density. This permits a simple numerical implementation.
- (ii) To mimic the real physical behavior, the microscopic stress should be inversely proportional to density.
- (iii) The microscopic stress should converge to a non-zero value at zero density. This requisite is deduced from investigations into the asymptotic stress behavior in thin layers [27].

25. Duysinx et al. (1998), 'Topology optimization of continuum structures with local stress constraints'
26. Le et al. (2010), 'Stress-based topology optimization for continua'

27. Verbart et al. (2017), 'A unified aggregation and relaxation approach for stress-constrained topology optimization'

The relation between stress and displacement is written as:

$$\langle \sigma_{VM} \rangle = C_e(\langle E \rangle) \langle \varepsilon \rangle, \quad (1.16)$$

where the variables between angular brackets $\langle \dots \rangle$ represent macroscopic variables.

Combining (i) and (ii) with Equations 1.1, and 1.16, the microscopic stress can be written as:

$$\sigma_{VM} = \frac{\langle \sigma_{VM} \rangle}{\rho_e^q} = \rho_e^{p-q} C_e(E_0) \langle \varepsilon \rangle, \quad (1.17)$$

where the exponent q is a number greater than 1.

One possible choice that satisfy all the requirements is $q = p$ [26–29]. Thus, the microscopic stress is defined as:

$$\sigma_{VM} = C_e(E_0) \langle \varepsilon \rangle. \quad (1.18)$$

From a physical perspective, the significance of microscopic stress becomes evident when considering an element with intermediate density and a porous microstructure. The microscopic stress presented in Equation 1.18 measures the stress of the microstructure. It is grounded in the assumption that the macroscopic deformations of the homogenized element generate within the microstructure of the element a stress state that remains unaffected by the density of the element itself.

CONSTRAINTS AGGREGATION AND RELAXATION When optimizing a structure with stress constraints using a NAND formulation, two primary challenges commonly arise:

- (i) Is it known in the literature [30, 31] that stress-based topology optimization suffers from the *singular minima* (or *singularity*) problem: firstly observed on truss structure optimization [32], these *minima* are almost inaccessible to a standard gradient-based optimizer, and they represent the *minima* of the optimization. This is because achieving the optimal solution to a problem using continuous design variables may necessitate passing through a state where the optimization constraints are violated, i.e. the *minimum* is on a lower dimension compared to the design space. This problem is often solved using a technique called *constraints relaxation* [33].
- (ii) The stress is a local measure, and thus a large set of constraints is generated when a reasonably fine mesh is used (one element, one constraint). This problem is often solved using a technique called *constraints aggregation* or *global constraints* [34].

Following the work developed by Verbart *et al.* [27], the lower bound

26. Le et al. (2010), ‘Stress-based topology optimization for continua’

27. Verbart et al. (2017), ‘A unified aggregation and relaxation approach for stress-constrained topology optimization’

28. Holmberg et al. (2013), ‘Stress constrained topology optimization’

29. Silva et al. (2019), ‘Stress-constrained topology optimization considering uniform manufacturing uncertainties’

33. Cheng et al. (1997), ‘ ε -relaxed approach in structural topology optimization’

34. Silva et al. (2021), ‘Local versus global stress constraint strategies in topology optimization’

27. Verbart et al. (2017), ‘A unified aggregation and relaxation approach for stress-constrained topology optimization’

[35.](#) Kreisselmeier et al. (1979), 'Systematic Control Design by Optimizing a Vector Performance Index'

Kreisselmeier-Steinrauer (KS) function [35] is used to approximate the local relaxed stress constraint maximum. The authors discovered that employing lower-bound KS aggregation functions to approximate the maximum operator in stress-constrained topology optimization eliminates the need for stress constraint relaxation methods to address the singularity issue. This is because the lower-bound functions inherently offer a combined effect of constraint aggregation and relaxation. The KS aggregated stress constraint function is defined as follows:

$$G_{\text{KS}}^{\text{L}} = \frac{1}{P} \ln \left(\frac{1}{N_e} \sum_{i \in \Omega} e^{P \bar{g}_i} \right). \quad (1.19)$$

Its main advantage over other different formulations is that it uses a single hyperparameter P to control the aggregation and the relaxation of the constraints simultaneously.

MINIMUM VOLUME FORMULATION The NAND minimum volume formulation for continuous discretization is written combining Equations 1.9, and 1.19 as:

$$\begin{aligned} \min_{\rho} \quad & V = \frac{1}{N_e} \sum_{i \in \Omega} \bar{\rho}_i, \\ \text{s.t.} \quad & G_{\text{KS}}^{\text{L}} = \frac{1}{P} \ln \left(\frac{1}{N_e} \sum_{i \in \Omega} e^{P \bar{g}_i} \right) \leq 0 \\ & \mathbf{Ku} = \mathbf{F} \\ & 0 \leq \rho_i \leq 1, \end{aligned} \quad (\mathbb{T}_1)$$

The optimization is carried out using a gradient descent optimization algorithm for which the sensitivities are given in analytical form. Using analytic gradients is in general more efficient than finite differences as it avoids the need for multiple function evaluations, making the optimization process faster and more precise.

SENSITIVITY ANALYSIS OF THE OBJECTIVE FUNCTION The objective of this section is to quickly present the calculation of the analytical sensitivity of the volume with respect to the design variable ρ . Deriving Equation 1.9 we obtain:

$$\frac{\partial V}{\partial \bar{\rho}_i} = \frac{1}{N_e}. \quad (1.20)$$

The sensitivity of the objective function can then be evaluated using Equations 1.20, 1.5, 1.6, and 1.7 as follows:

$$\frac{dV}{d\rho_i} = \sum_{j \in \mathbb{N}_{i,R}} \frac{\partial V}{\partial \bar{\rho}_j} \frac{\partial \bar{\rho}_j}{\partial \bar{\rho}_i} \frac{\partial \bar{\rho}_j}{\partial \rho_i}. \quad (1.21)$$

SENSITIVITY ANALYSIS OF THE CONSTRAINT FUNCTION This section focuses on the details of the calculation of how the constraint function G_{KS}^L changes with respect to the design variable ρ . The sensitivity of the aggregated constraint function with respect to the design variable ρ is evaluated using:

$$\frac{dG_{KS}^L}{d\rho_i} = \sum_{j \in \mathbb{N}_{i,R}} \frac{\partial G_{KS}^L}{\partial \bar{\rho}_j} \frac{\partial \bar{\rho}_j}{\partial \bar{\rho}_j} \frac{\partial \bar{\rho}_j}{\partial \rho_i}. \quad (1.22)$$

As the constraint function $G_{KS}^L = G(\bar{\rho}, \mathbf{u}(\bar{\rho}))$ is explicitly and implicitly (via the relationship with \mathbf{u}) depending on $\bar{\rho}$, the first-order derivative is evaluated using the total derivative formula:

$$\frac{\partial G_{KS}^L}{\partial \bar{\rho}_j} = \frac{dG}{d\bar{\rho}_j} = \frac{\partial G}{\partial \bar{\rho}_j} + \frac{\partial G}{\partial \mathbf{u}} \frac{d\mathbf{u}}{d\bar{\rho}_j}. \quad (1.23)$$

As function G_{KS}^L depends on \mathbf{u} via the stresses σ_i , it is possible to write:

$$\frac{\partial G}{\partial \mathbf{u}} = \sum_{i \in \Omega} \left(\frac{\partial G}{\partial \sigma_i} \frac{\partial \sigma_i}{\partial \mathbf{u}} \right). \quad (1.24)$$

Combining Eq. 1.23 with Eq. 1.24, we obtain:

$$\frac{dG}{d\bar{\rho}_j} = \underbrace{\frac{\partial G}{\partial \bar{\rho}_j}}_A + \sum_{i \in \Omega} \underbrace{\left(\underbrace{\frac{\partial G}{\partial \sigma_i}}_B \underbrace{\frac{\partial \sigma_i}{\partial \mathbf{u}}}_C \right)}_D \frac{d\mathbf{u}}{d\bar{\rho}_j}. \quad (1.25)$$

We compute the four factors separately:

A – The first term represents the explicit relationship of G to the physical densities and its calculation is straightforward:

$$\frac{\partial G}{\partial \bar{\rho}_j} = \frac{1}{P} \frac{\left(\frac{\sigma_{VM,j}}{\sigma_L} - 1 \right) \frac{1}{N_e} P e^{P \bar{g}_j}}{\frac{1}{N_e} \sum_k e^{P \bar{g}_k}} = \left(\frac{\sigma_{VM,j}}{\sigma_L} - 1 \right) \frac{e^{P \bar{g}_j}}{\sum_k e^{P \bar{g}_k}}. \quad (1.26)$$

B – The second term can be calculated using the chain rule:

$$\frac{\partial G}{\partial \sigma_i} = \frac{\partial G}{\partial \bar{g}_i} \frac{\partial \bar{g}_i}{\partial \sigma_i} = \frac{1}{P} \frac{\frac{1}{N_e} P e^{P \bar{g}_i} \bar{\rho}_i}{\frac{1}{N_e} \sum_k e^{P \bar{g}_k} \sigma_L} = \frac{\bar{\rho}_i}{\sigma_L} \frac{e^{P \bar{g}_i}}{\sum_k e^{P \bar{g}_k}}. \quad (1.27)$$

C – We reformulate Equation 1.15 to be written in global coordinates instead of local:

$$\sigma_i^2 = \mathbf{q}_s^T \mathbf{S} \mathbf{q}_s = \mathbf{u}^T |\mathbf{S}_i|_g \mathbf{u}, \quad (1.28)$$

where $|\mathbf{S}_i|_g$ represents the matrix \mathbf{S} of Equation 1.15 written on

2: The matrix $|S_i|_g$ can be calculated using the very same assembling approach used for the stiffness matrix \mathbf{K} starting from the elemental stiffness matrix \mathbf{K}_e . As the global stiffness matrix \mathbf{K} , $|S_i|_g$ is symmetric and sparse.

global coordinates². We can now differentiate Equation 1.28 with respect of the displacement field in global coordinates \mathbf{u} to obtain:

$$\frac{\partial \sigma_i}{\partial \mathbf{u}} = \frac{|S_i|_g \mathbf{u}}{\sigma_i}. \quad (1.29)$$

Equations 1.27, and 1.29 are now combined to obtain the result of the product of the \mathbf{B} and \mathbf{C} terms. As a result, the derivatives of G with respect to \mathbf{u} , are written as:

$$\frac{\partial G}{\partial \mathbf{u}} = \frac{\bar{\rho}_j}{\sum_i e^{P\bar{g}_i}} |S_j|_g \mathbf{u}. \quad (1.30)$$

D – To calculate the last term, we take the static equilibrium equation $\mathbf{K}\mathbf{u} = \mathbf{f}$ and differentiate it with respect to the physical densities $\bar{\rho}_j$, obtaining:

$$\frac{\partial \mathbf{K}}{\partial \bar{\rho}_j} \mathbf{u} + \mathbf{K} \frac{\partial \mathbf{u}}{\partial \bar{\rho}_j} = 0 \iff \frac{\partial \mathbf{u}}{\partial \bar{\rho}_j} = -\mathbf{K}^{-1} \frac{\partial \mathbf{K}}{\partial \bar{\rho}_j} \mathbf{u}, \quad (1.31)$$

where

$$\frac{\partial \mathbf{K}}{\partial \bar{\rho}_j} = (E_0 - E_{\min}) p \bar{\rho}_j^{p-1} \mathbf{K}_{e,j}. \quad (1.32)$$

Equation 1.32 represent the well-known first-derivative term of the global stiffness matrix \mathbf{K} with respect to the physical densities $\bar{\rho}_j$ when using SIMP material scheme [14]. We finally obtain the last term:

$$\frac{d\mathbf{u}}{d\bar{\rho}_j} = -\mathbf{K}^{-1} \left((E_0 - E_{\min}) p \bar{\rho}_j^{p-1} \mathbf{K}_e \right) \mathbf{u}. \quad (1.33)$$

Combining Eq. 1.25, Eq. 1.26, Eq. 1.30, and Eq. 1.33, we finally obtain:

$$\frac{\partial G_{KS}^L}{\partial \bar{\rho}_j} = \left(\frac{\sigma_{VM,j}}{\sigma_L} - 1 \right) \frac{e^{P\bar{g}_j}}{\sum_k e^{P\bar{g}_k}} - \mathbf{K}^{-1} \frac{\partial G}{\partial \mathbf{u}} \left(\frac{\partial \mathbf{K}}{\partial \bar{\rho}_j} \right) \mathbf{u}. \quad (1.34)$$

3: More information about the adjoint method used to analytically calculate the first-order derivatives can be found on the Martins *et al.* book [13].

To avoid the explicit calculation of \mathbf{K}^{-1} we use the *adjoint method*³. Here is the linear system that, once solved, permits to calculate ψ :

$$\mathbf{K}\psi = \frac{\partial G}{\partial \mathbf{u}} \iff \psi = \mathbf{K}^{-1} \frac{\partial G}{\partial \mathbf{u}}. \quad (1.35)$$

This formula is called *adjoint equation*. This equation is solved for ψ and the result used to evaluate:

$$\frac{\partial G_{KS}^L}{\partial \bar{\rho}_j} = \left(\frac{\sigma_{VM,j}}{\sigma_L} - 1 \right) \frac{e^{P\bar{g}_j}}{\sum_k e^{P\bar{g}_k}} - \psi \left(\frac{\partial \mathbf{K}}{\partial \bar{\rho}_j} \right) \mathbf{u}. \quad (1.36)$$

where N represents the size of the square matrix describing the linear system. Equation 1.36 represents the first-order derivative equation used to evaluate the sensitivity of the constraint function G_{KS}^L with respect to the physical densities $\bar{\rho}$. The value of ψ is calculated every iteration solving the linear system 1.35.

1.1.2 TRUSS DISCRETIZATION SAND MINIMUM VOLUME FORMULATION

We are now shifting our focus from continuous structures to discrete truss systems, describing the Truss Topology Optimization (TTO) (also known in early literature as layout optimization), a structure optimization method that focuses on discrete structures. In his most used formulation, Truss Topology Optimization (TTO) aims at reducing material usage while meeting stress criteria using a SAND approach. The problem is already well-posed for comparison with continuous discretization, and we intend to explore specific key concepts within its established framework.

CLASSICAL MICHELL STRUCTURES The characteristics of these structures are described by some simple criteria that date to the end of the 19th and the beginning of the 20th century. When a structure is statically determinate — i.e. the structure is not a mechanism, and it is not over-constrained by the supports — the Maxwell theorem [36] states that:

$$\sum_{\forall i | q_i > 0} \ell_i q_i + \sum_{\forall i | q_i < 0} \ell_i q_i = \text{const.} \quad (1.37)$$

where ℓ_i and q_i represent the length and the axial force of the i -th member, respectively. The constant value at the right of Equation 1.37 depends on the nature of the boundary conditions and the material used. The Maxwell theorem dictates that any increment in compression forces must be counterbalanced by an equivalent increase in tension forces when the structure remains topologically unchanged. So for statically determinate structures the structure layout is not influenced by the ratio between σ_c and σ_t , Young's modulus E of the material, nor the force magnitude.

Starting from Maxwell's findings, Michell theorized two further criteria for optimal truss structures [37] valid when the maximum allowable stress is equal in tension and compression ($\sigma_t = \sigma_c$) and when the supports of the structure are statically determinate. The first one states that all the members of an optimal structure should present internal stress equal in magnitude to the maximum allowable value of the material – i.e. the structure is *fully stressed*. The second criterion asserts that the strain of all the members of the structure should be equal and there should be no other point having a strain higher than this value. As formulated, these two criteria are known as the Michell criteria. The second criterion was later generalized by Hemp [4] as:

Solving linear system 1.35 instead of directly calculating the inverse matrix of K is more efficient from a performance perspective. The cost of solving a system using the Cholesky decomposition is $\mathcal{O}(N^3/3)$, while a matrix inversion is $\mathcal{O}(N^3)$.

36. Maxwell (1870), 'I.—On Reciprocal Figures, Frames, and Diagrams of Forces'

37. Michell (1904), 'The limits of economy of material in frame-structures'

4. Hemp (1973), 'Optimum Structures'

$$-\frac{1}{\sigma_c} \leq \varepsilon \leq \frac{1}{\sigma_t}. \quad (1.38)$$

Compared to the second Michell criterion, Equation 1.38 permits to correct identification of the minimum volume structure even when different strength values for compression and tension and different support types are taken. These criteria are known as the Michell-Hemp criteria.

- 2. Dorn et al. (1964), 'Automatic design of optimal structures'
- 3. Chan (1964), 'Optimum structural design and linear programming'
- 4. Hemp (1973), 'Optimum Structures'

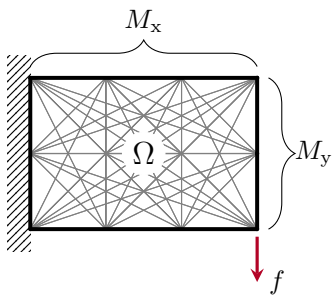


Figure 1.4: The domain Ω is discretized using a set of straight members connecting a set of nodes. This framework is known as the ground structure.

- 38. Gilbert et al. (2003), 'Layout optimization of large-scale pin-jointed frames'
- 39. Pedersen (1973), 'Optimal Joint Positions for Space Trusses'
- 40. Achtziger (2007), 'On simultaneous optimization of truss geometry and topology'
- 41. Descamps et al. (2013), 'A lower-bound formulation for the geometry and topology optimization of truss structures under multiple loading'
- 42. He et al. (2015), 'Rationalization of trusses generated via layout optimization'
- 43. Lu et al. (2023), 'Reducing the number of different members in truss layout optimization'

PLASTIC MATERIAL FORMULATION The rigid-plastic formulation characterizes the material as entirely rigid up to the point of reaching the yield stress, denoted as σ_y , and subsequently assumes a constant stress level of σ_y once that threshold is exceeded. This formulation is a clear consequence of the application of the Michell-Hemp criteria and has thus been used in the very first work of layout optimization (also known as TTO) [2–4].

THE GROUND STRUCTURE APPROACH The ground structure is a framework composed of various structural members that connect specified points or nodes in two- or three-dimensional space (see Fig. 1.4). These members can take the form of beams, columns, wires, or bars elements, depending on the specific structural requirements. In this thesis, we will deal with trusses, and so the chosen element is the bar. Since the nodes within the ground structure are considered pin-joints, all straight members exclusively face either tension or compression loads.

Depending on how the connectivity of the grid of nodes is, we can experience very different ground structures. In a fully connected ground structure, every node within the system is linked to every other node, resulting in a dense and redundant structural configuration. The number of bars N_{el} of a fully connected ground structure can be determined using the following formula:

$$N_{el} = \frac{M \cdot (M - 1)}{2}, \quad (1.39)$$

where M represents the number of nodes of the structure.

In classic works, the ground structure is used as the start of the optimization, where the optimized structure is obtained as a subset of the initial ground structure, but multiple alternative approaches have been proposed since then, e.g. starting from a very coarse ground structure that is enriched during the analysis [38], or giving the nodes of a coarse ground structure the possibility to move, during [39–41], or after the optimization, simultaneously reducing the number of active members of the solution [42, 43].

OPTIMIZATION FORMULATION The volume minimization formulation with maximum stress constraints is stated in terms of members' cross-sectional areas \mathbf{a} and member forces \mathbf{q} as follows:

$$\begin{aligned} \min_{\mathbf{a}, \mathbf{q}} \quad & V = \ell^T \mathbf{a} \quad (\text{Volume minimization}) \\ \text{s.t.} \quad & \mathbf{B}_s \mathbf{q} = \mathbf{f} \quad (g_{\text{eq}}) \\ & -\sigma_c \mathbf{a} \leq \mathbf{q} \leq \sigma_t \mathbf{a} \quad (g_{\text{st,c}}, g_{\text{st,t}}) \\ & \mathbf{a} \geq 0, \end{aligned} \quad (\mathbb{P}_0)$$

where \mathbf{B}_s is a $N_{\text{dof}} \times N_{\text{el}}$ matrix containing the direction cosines of the i -th member with respect to the i -th degree of freedom to calculate the nodal force equilibrium constraints \mathbf{g}_{eq} , and where N_{dof} is the number of Degrees Of Freedom (DOFs), equal to $2M$ or $3M$ for a two- or a three-dimensional load case, respectively. $\mathbf{q} = [q_1, q_2, \dots, q_{N_{\text{el}}}]^T$ is the vector containing the internal member forces, with a positive sign when in tension, caused by the external load $\mathbf{f} = [f_1, f_2, \dots, f_{N_{\text{dof}}}]^T$. The state variable $\mathbf{a} = [a_1, a_2, \dots, a_{N_{\text{el}}}]^T$ represents the cross-sectional area of the N_{el} members of the structure. σ_c and σ_t are the compressive and tensile maximum allowable stresses of the material, respectively, used in the stress constraints $\mathbf{g}_{\text{st,c}}$ and $\mathbf{g}_{\text{st,t}}$. This formulation takes into account only the linear behavior of the structure and is equivalent to the original and well-studied member force formulation [2, 14].

The resolution of Problem \mathbb{P}_0 frequently produces complex structures made up of a multitude of small members that tend to the shapes of Michell structures (see Fig 1.5) [37, 38]. While it is known that these structures are nearly optimal, one would want to limit the complexity of the resulting structure. Substituting ℓ with $\tilde{\ell} = [\ell_1 + s, \ell_2 + s, \dots, \ell_{N_{\text{el}}} + s]^T$ in the objective function of \mathbb{P}_0 , one would penalize the appearance of small members [44]. $\tilde{\ell}$ is called augmented member length and s the joint cost. This approach mimics the mesh-independency regularization filter of topology optimization, avoiding the inevitable apparition of structures with tiny features when a fine mesh is adopted.

1.2 COMPARISON BETWEEN CONTINUOUS AND TRUSS DISCRETIZATION

In the upcoming discussion, we will be comparing the optimized structures using discrete and continuous meshes. Our primary objective in this comparison is to gain a comprehensive understanding of the application limits inherent in these two structural discretization methods. If, indeed, we identify such limitations, the aim is to discern and define them. Such discussions have already been pointed out in the literature [7, 45], but they are usually only empirical considerations and not numerical analysis.

- 2. Dorn et al. (1964), 'Automatic design of optimal structures'
- 14. Bendsøe et al. (2004), 'Topology Optimization'
- 37. Michell (1904), 'The limits of economy of material in frame-structures'
- 38. Gilbert et al. (2003), 'Layout optimization of large-scale pin-jointed frames'
- 44. Parkes (1975), 'Joints in optimum frameworks'

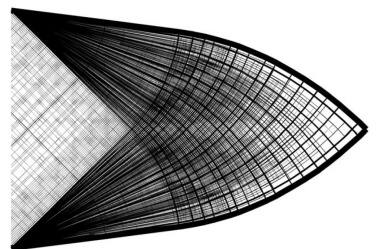


Figure 1.5: The optimal structures found by layout optimization tend at Michell-like structures, made up of a very large number of infinitesimal struts [38].

- 7. Bendsøe (1989), 'Optimal shape design as a material distribution problem'
- 45. Watts et al. (2019), 'Simple, accurate surrogate models of the elastic response of three-dimensional open truss micro-architectures with applications to multiscale topology design'

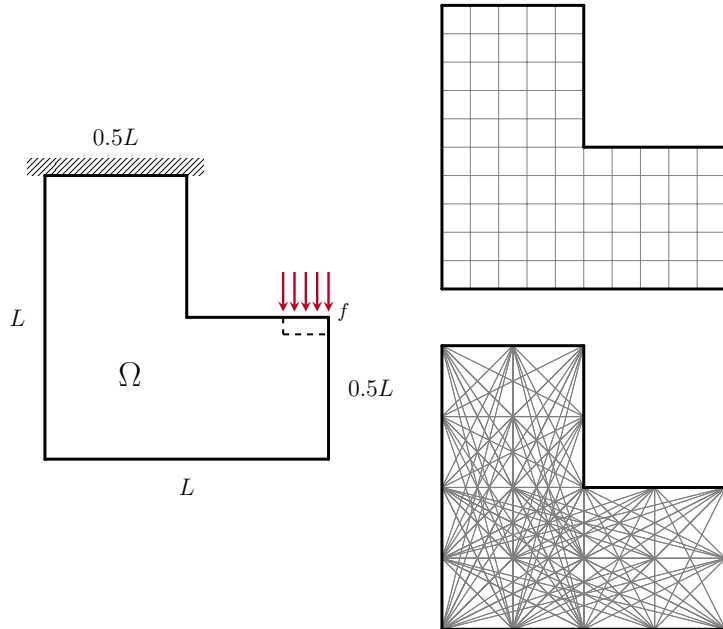


Figure 1.6: On the left, plot of the L-shape beam test case, on the right the graphical representations of the two discretizations used, the continuous (above) and the truss-like (below).

Since our interest is in ultralight structures, we are especially interested in comparing the results of both optimization methods when dealing with different volume fractions on a common load case. Since we can't directly control volume in our formulation, we will adjust the material properties to influence the volume fraction of the optimized structure. For this comparative analysis, we have selected three key performance metrics: the volume fraction $V_f = V/\Omega$, the structural compliance C , and the maximum material allowable σ_L . Among these, we classify stress limit as the active metric used to influence the optimization, while volume and compliance are the objective of the optimization and a passive metric, respectively. In addition to the aforementioned performance metrics, we will also track the execution time of the algorithms.

1.2.1 DEFINITION OF A COMMON TEST CASE

25. Duysinx et al. (1998), 'Topology optimization of continuum structures with local stress constraints'

26. Le et al. (2010), 'Stress-based topology optimization for continua'

The L-shape beam is one of the most used load case benchmarks for stress-based topology optimization [25, 26]. This choice is driven by the distinctive geometry of the problem, which generates a stress concentration, particularly at the sharp corner—a phenomenon approaching infinity. Consequently, optimized solutions often feature a large fillet, mitigating the intensity of the stress singularity. The geometric description of the test case is given in Fig. 1.6. The beam with dimensions $L \times L$ presents an encastre on the top part and a load on the right extremity. For the continuous mesh case the load is distributed over multiple elements (5% of L) to avoid stress concentrations and the stress constraints are not evaluated there. This zone is considered outside of the design domain Ω .

To permit the discretization comparison, the structure is divided into

two distinct meshes: in the continuous case, we employ a mesh consisting of 600×600 quadrilateral elements, totaling 270 000 elements, while for the truss configuration, we employ a mesh with 33×33 nodes and a fully connected ground structure, comprising a total of 305 728 candidates.

We employ the same isotropic material and structure dimensions for the two optimizations, and the complete data is resumed in Table 1.1. The value of the maximum material admissible σ_L is used as the parameter that influences the volume fraction of the solutions. For simplicity, all numeric values are assumed normalized and dimensionless.

1.2.2 NUMERICAL APPLICATION

The focus of this section is to provide the numerical framework used to carry out the comparative analysis of the optimization results obtained from continuous and truss discretizations. The optimization formulations previously described have been implemented using Python.

The optimizing algorithm chosen for the continuous mesh is the Method of Moving Asymptotes (MMA) [46]. The parameter called *movelimit*⁴ is set to 0.1 while the other algorithm's parameters are set to their default value. A continuation scheme for the aggressiveness of the projection parameter β is set to increase by one every 200 iterations, the number of max iteration is set to 7500, the stopping criteria is calculated as $\|r_k\|_2/\sqrt{N_e}$ on the physical densities $\bar{\rho}$ [22], and it is set to 10^{-4} . The aggregation parameter P of the aggregation function G_{KS}^L is set to 32. The numerical implementation is carried out using the NLOpt Python optimization framework [47], analytically evaluating the sensitivity using Equations 1.20, and 1.25.

Formulation \mathbb{P}_0 represents a LP problem that can be efficiently solved by modern algorithms. In this work, we used the Python package CVXPY 1.2.2 [48] with the ECOS 2.0.7 [49] solver. The joint cost s is set to 0.001 and the stopping criteria is chosen as $\|\Delta x\|_\infty \leq 10^{-8}$. As Formulation is linear, no sensitivity calculation is carried out.

The optimizations presented in this section are performed on a server equipped with an Intel® Xeon® CPU E5-2650 @ 2.20 GHz and using 8 GB of RAM.

CONTINUOUS MESH OPTIMIZATION RESULTS In this section, we generate multiple optimized structures with different volume fractions V_f by launching the optimization code for continuous mesh with different values of the material admissible σ_L spanning from 0.2 to 20.

On top of volume fraction, compliance, and stress, we evaluate an additional metric specific to continuous meshes called the *measure*

Parameter	Value
E	1
ν	0.3
L	100
σ_L	var.

Table 1.1: Material data used for the optimizations. The value of the maximum material admissible σ_L is used as the parameter to generate multiple optimized topologies.

46. Svanberg (1987), 'The method of moving asymptotes—a new method for structural optimization'

47. More information on the implementation of the *movelimit* parameter can be found on the paper by Verbart [27]

48. Johnson (2007), 'The NLOpt nonlinear-optimization package'

49. Diamond et al. (2016), 'CVXPY: A Python-Embedded Modeling Language for Convex Optimization'

49. Domahidi et al. (2013), 'ECOS: An SOCP solver for embedded systems'

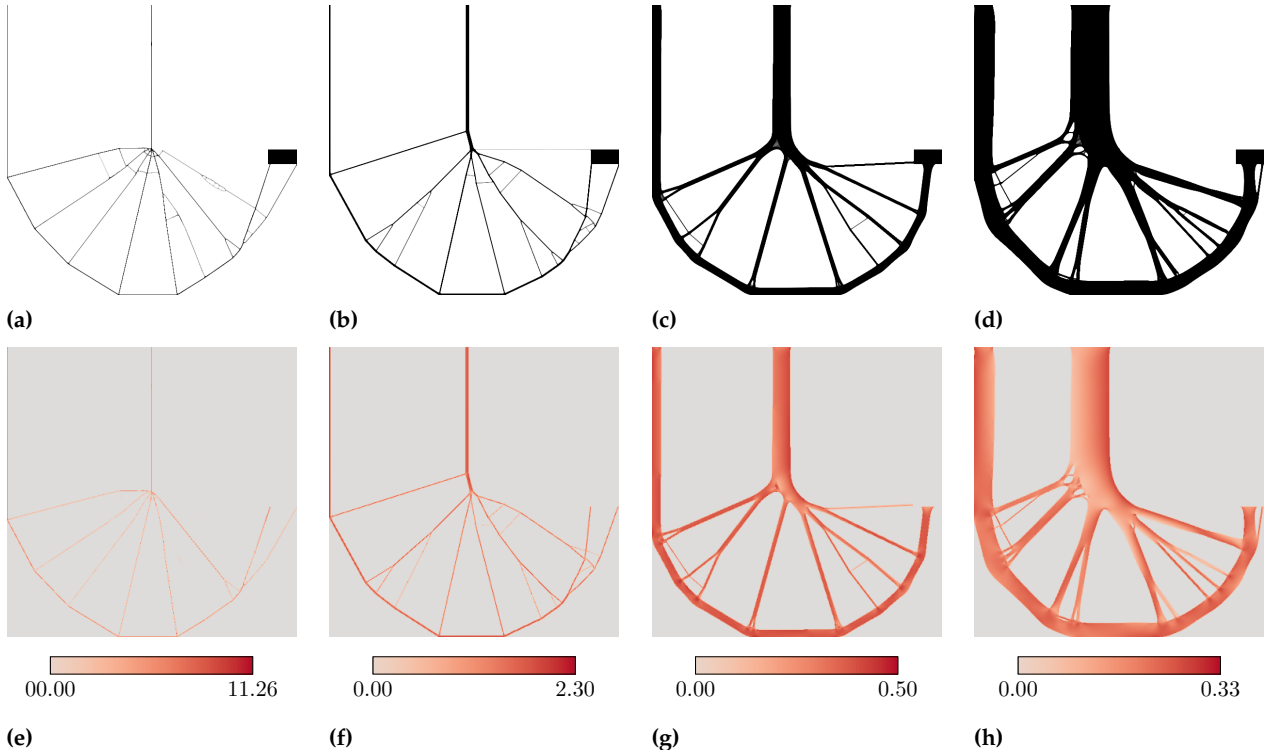


Figure 1.7: (a-d) topology optimized structures for different material admissibles $\sigma_L = 10.00, 2.00, 0.40$ and 0.25 , showing a volume fraction of $V_f = 1.60\%, 4.04\%, 18.03\%$ and 34.71% , respectively. (e-h) Von Mises stress distribution of the optimized structures.

21. Sigmund (2007), 'Morphology-based black and white filters for topology optimization'

of non-discreteness [21] to evaluate the quality of the solutions. It is defined as:

$$M_{nd} = \frac{\sum_e 4\bar{\rho}_e(1 - \bar{\rho}_e)}{n} \times 100\%, \quad (1.40)$$

where results near zero mean a completely black-and-white design.

The results obtained for $\sigma_L = 10.00, 2.00, 0.40$ and 0.25 are shown in Fig. 1.7. In the upper part of the figure (a-d), we see the topology of the optimized structures with an ascending volume fraction V_f . Interestingly, the topology of the solution remains almost unchanged, varying principally in the thickness of its members. We notice the classic large fillet around the corner that alleviates the stress concentration problem. As the volume decreases, the optimized structure tends to a solution that resembles Michell structures, with a reducing fillet radius. In those cases, we know that the topology optimization algorithm acts as a method for the layout of truss-like structures [6]. This effect is caused by the combination of different factors, such as the regularization filter, the mesh size, and the low volume fraction [50]. A summary of the numerical results is presented in Table ??.

6. Bendsøe et al. (1988), 'Generating optimal topologies in structural design using a homogenization method'

50. Sigmund et al. (2016), 'On the (non-)optimality of Michell structures'

In the lower part of Fig. 1.7 (e-f), we plot the equivalent Von Mises stress for every element of the solution with physical density $\bar{\rho} > 0.5$. Multiple interesting observations can be made. First, we notice that the

σ_L	max σ_L	V_f	C	M_{nd}	It.	Time
20.00	23.51	1.18 %	6992	1.91 %	1142	8 h 11 m
10.00	11.26	1.60 %	3837	2.19 %	1147	7 h 55 m
8.00	8.78	1.74 %	2766	1.95 %	792	5 h 39 m
6.00	7.15	1.89 %	2243	1.81 %	806	5 h 35 m
5.00	5.81	2.17 %	1823	1.81 %	849	5 h 53 m
4.00	4.69	2.67 %	1424	2.02 %	894	6 h 12 m
3.00	3.47	3.00 %	1133	1.64 %	993	6 h 45 m
2.00	2.30	4.04 %	781	1.45 %	1189	8 h 20 m
1.00	1.18	7.28 %	404	1.35 %	1621	11 h 41 m
0.90	1.06	8.09 %	365	1.31 %	1656	11 h 36 m
0.80	0.96	8.82 %	332	1.21 %	1937	15 h 21 m
0.70	0.84	10.05 %	292	1.09 %	1827	13 h 21 m
0.60	0.73	11.80 %	250	1.19 %	1955	14 h 21 m
0.50	0.61	14.18 %	213	1.06 %	2032	15 h 39 m
0.40	0.50	18.03 %	170	1.08 %	2259	17 h 6 m
0.35	0.44	21.12 %	148	1.15 %	2421	19 h 29 m
0.30	0.38	26.21 %	126	1.50 %	3100	24 h 46 m
0.25	0.33	34.71 %	104	1.04 %	3484	27 h 39 m
0.20	0.27	48.08 %	77	1.26 %	7500	91 h 46 m

stress distribution is almost uniform in the structure, and it tends to the value of the material admissible σ_L – i.e. we approach a *fully stressed* structure. Even if the geometric support of the theory is different, it looks like the topology-optimized structures follow the Michell criteria presented in Section 1.1.2 for optimal truss structures. Furthermore, it is observed that the maximum stress exceeds the material admissible σ_L . Aggregation methods aim to estimate the maximum value of the stress constraint across a group of elements. However, these aggregation methods do not perfectly align with the exact maximum value, which is a recognized limitation. To address this challenge, multiple approaches have been proposed within the aggregation framework to accurately account for the true constraint value, like using a set of active stress constraints [51], several aggregation clusters [52] or rectifier functions [53].

Looking again at Table 1.2, we notice that the optimization processes exhibit long execution times, especially when dealing with extreme cases like high-volume fractions. This effect is likely caused by the very fine mesh used to discretize the design domain Ω , by the sensitivity calculation by means of the adjoint method, and by the increasing difficulty of satisfying the stress constraints.

As previously mentioned, our focus lies in exploring the method’s limits, particularly at the volume fraction boundaries. When dealing with excessively weak materials – i.e. materials that show a low σ_L , we encounter a scenario where no solution can be attained since no distribution can fulfill the imposed constraints. Throughout our research with this specific test case and mesh size, we did not produce any solutions with a volume fraction exceeding 50%. Although we

Table 1.2: Numerical results of the topology optimization method of the L-shape beam load case with varying material admissible σ_L on a 600×600 elements mesh.

51. Bruggi et al. (2012), ‘Topology optimization for minimum weight with compliance and stress constraints’

52. París et al. (2010), ‘Block aggregation of stress constraints in topology optimization of structures’

53. Norato et al. (2022), ‘A maximum-rectifier-function approach to stress-constrained topology optimization’

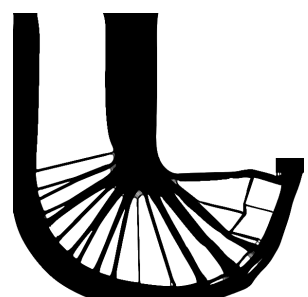


Figure 1.8: The optimized structure for $\sigma_L = 0.2$ with $V_f = 48.08 \%$, but does not converge after 7500 iterations.

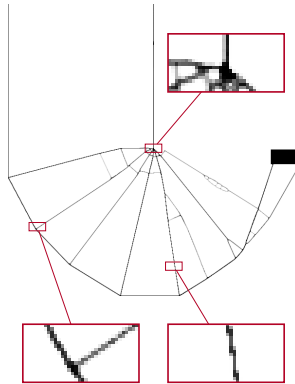


Figure 1.9: The optimized structure for $\sigma_L = 10.0$ with $V_f = 1.60\%$. Some of the structure's features present not even a fully-dense element in their thickness.

haven't reached that scenario with σ_L set to 0.2, the calculation time and the number of iterations increase significantly, showing that we have encountered the method's limits. The calculation time has significantly increased because the algorithm faces greater difficulty in satisfying the stress constraints. Fig. 1.8 shows the topology of the solution with $\sigma_L = 0.2$, $V_f = 48.08\%$ and over five days of optimization.

Conversely, when dealing with exceedingly strong material – i.e. materials that show a high σ_L , the optimal scenario would demand such minimal material usage that certain sections of the structure become thinner than the width of a single element. In this case, the mesh used for discretization is too coarse to accurately represent the solution, and finer meshing becomes essential to capture the intricate details of the optimized design. Fig. 1.9 shows the limit case when $\sigma_L = 10.0$ and $V_f = 1.60\%$.

Finally, in Fig. 1.10 are the plots summarizing our findings, with the limits highlighted. To effectively show the different orders of magnitude present in the plot, we have used both linear and logarithmic scales simultaneously. It's interesting to note that the volume fraction V_f follows a hyperbolic relationship, while compliance C exhibits a linear correlation with respect to the material admissible σ_L .

TRUSS MESH OPTIMIZATION RESULTS In this section, we present the optimized structures of the truss discretization. Fig. 1.11 provides a visual representation of the topology and the corresponding stress distribution. Due to the inherent linearity properties of Formulation \mathbb{P}_0 , several intriguing characteristics emerge. Notably, in the case of the tested L-shaped case, we encounter a scenario where the boundary conditions are neither overconstrained nor subject to asymmetric stress constraints. Consequently, this test case aligns with the Michell criteria. As a result, the topology does not vary regardless of the imposed stress limit, and the structure is fully stressed. Additionally,

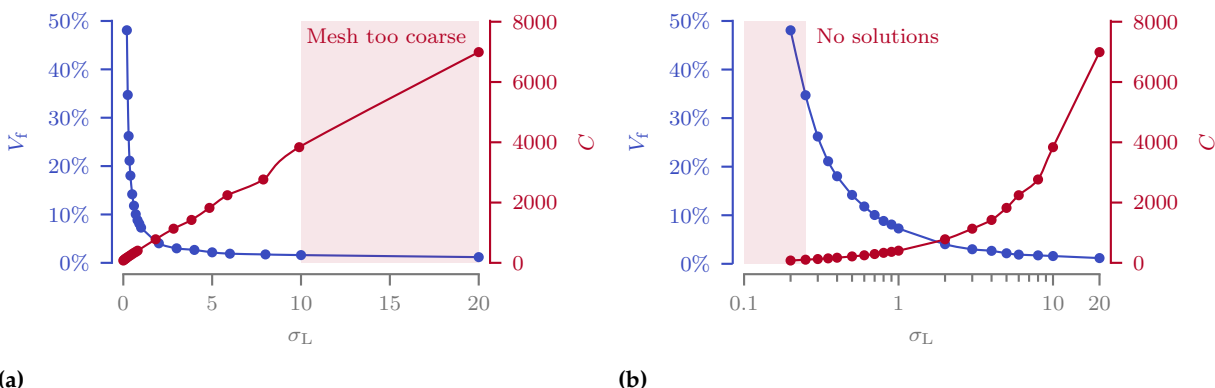


Figure 1.10: Linear (a) and logarithmic (b) plot of the volume fraction V_f and the compliance C with respect to the maximum material admissible σ_L for the continuous mesh structures. Areas in red represent the boundaries of the applied method.

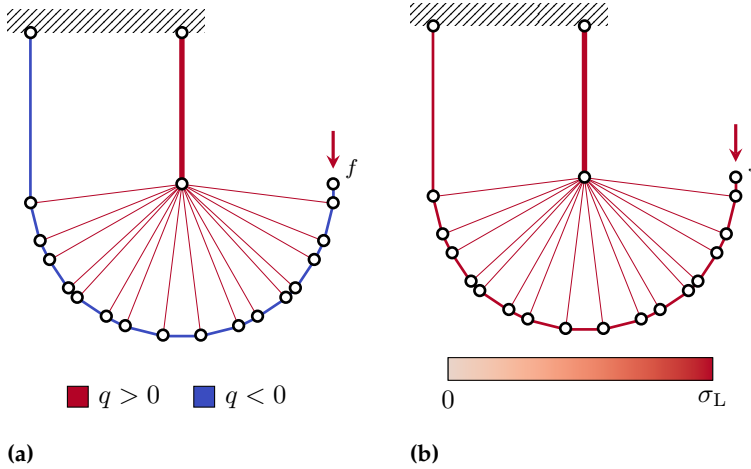


Figure 1.11: Topology (a) and stress (b) plot for the truss-like discretization.

Table 1.3: Numerical results of the TTO method of the L-shape beam load case with varying material admissible σ_L on a 33×33 ground structure.

σ_L	V_f	C	Min λ	Time
50.0	0.12 %	23 282	111.7	1 m 6 s
20.0	0.31 %	9313	70.6	1 m 9 s
10.0	0.62 %	4656	49.9	1 m 18 s
8.0	0.78 %	3725	44.7	1 m 15 s
6.0	1.03 %	2794	38.7	1 m 10 s
5.0	1.24 %	2328	35.3	1 m 24 s
4.0	1.55 %	1863	31.6	1 m 18 s
3.0	2.07 %	1397	27.4	1 m 15 s
2.0	3.10 %	931	22.3	1 m 15 s
1.0	6.21 %	466	15.8	1 m 17 s
0.9	6.90 %	419	15.0	1 m 20 s
0.8	7.76 %	373	14.1	1 m 21 s
0.7	8.87 %	326	13.2	1 m 16 s
0.6	10.35	279 %	12.2	1 m 20 s
0.5	12.42	233 %	11.2	1 m 22 s

the following equation consistently holds:

$$V^* = \frac{fL}{\sigma_L} \cdot \text{const.}, \quad (1.41)$$

where the multiplicative constant depends on the load case and the ground structure used to discretize the design space Ω [54]. The execution time of the optimization is approximately 90 s and does not change with respect to the maximum stress σ_L . The results of the multiple optimizations can be found in Table 1.3.

It's worth noting that we have intentionally opted for a fine mesh here to achieve a design variable count roughly equivalent to that of the continuous mesh case. We have utilized a fully connected ground structure with 33×33 nodes, but in reality, we obtain satisfactory results even with just 13×13 nodes (see Fig. 1.12). In this case we obtain a normalized volume $V^* = 4.705 fL/\sigma_L$, signifying a 1.05 % increase compared to the 33×33 case with $V^* = 4.656 fL/\sigma_L$ with a variable count reduction of 97.4 % (305 728 vs 7705 candidates). The computational time remains below one second.

54. Lewiński et al. (1994), 'Extended exact solutions for least-weight truss layouts—Part I'

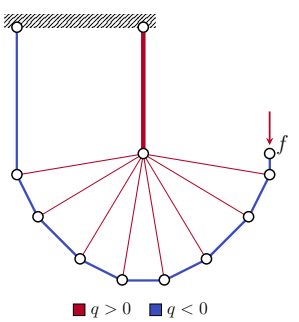


Figure 1.12: Optimized structure obtained on a fully connected ground structure with 13×13 nodes.

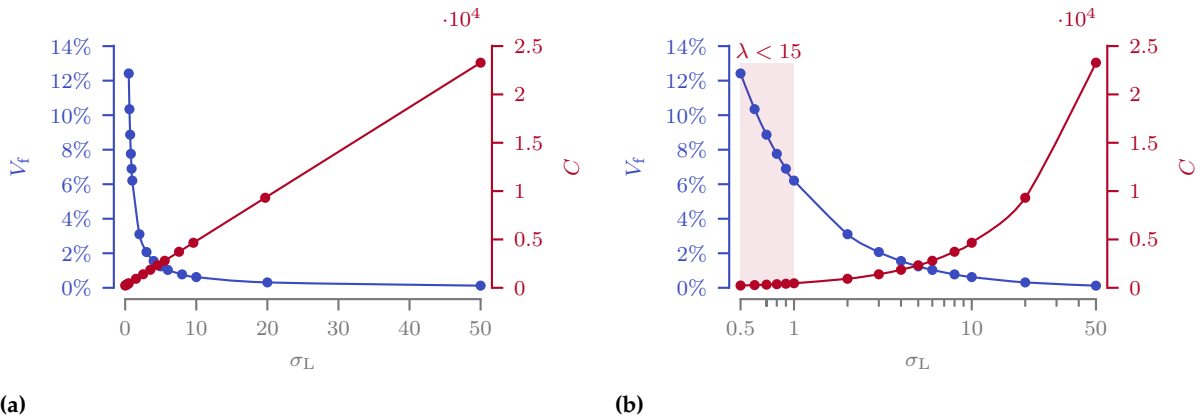


Figure 1.13: Linear (a) and logarithmic (b) plot of the volume fraction V_f and the compliance C with respect to the maximum material admissible σ_L for the truss-like structures. Areas in red represent the boundaries of the applied method.

In assessing solution quality, we employ a distinct metric known as the slenderness ratio, denoted as λ , which represents the ratio between the length and the radius of gyration of the bar. In our specific case, we have established a minimum slenderness ratio of 15. For a bar with a circular cross-sectional area, this corresponds to a radius of R_λ for a bar length of $7.5 R_\lambda$. We highlighted in red the optimized structures that does not repeat the minimum slenderness ratio in Table 1.3. It is important to note that this metric is very sensible to the ground structure used: for example in the 13×13 nodes test case, λ becomes critical ($\lambda = 14.8$) only when $\sigma_L = 0.25$ and $V_f = 25.09$, suggesting that a control of this parameter during the optimization should be beneficial.

Lastly, Fig. 1.13 provides a visual summary of our findings, emphasizing in red the observed limits. To effectively show the different orders of magnitude present in the plot and how already done for the continuous mesh case, we have used both linear and logarithmic scales simultaneously. In this case, the compliance exhibits a perfectly linear relationship, while the volume follows a hyperbolic law in accordance with Equation 1.41.

1.2.3 DISCUSSION

In this section, we present a series of graphs for the two formulations comparing the three figures of merit that have been considered thus far: the maximum material admissible σ_L , the compliance C , and the volume fraction V_f . It's important to note that the data presented in these graphs excludes the values that fall outside the limits highlighted for the two different discretizations in the previous subsections.

Fig. 1.14 depicts the stress compliance graph for the L-shaped beam load case under consideration. It is evident that the truss configuration consistently exhibits lower compliance values for every considered material admissible and maintains a perfectly linear relationship, in contrast to the continuous discretization approach. We speculate that

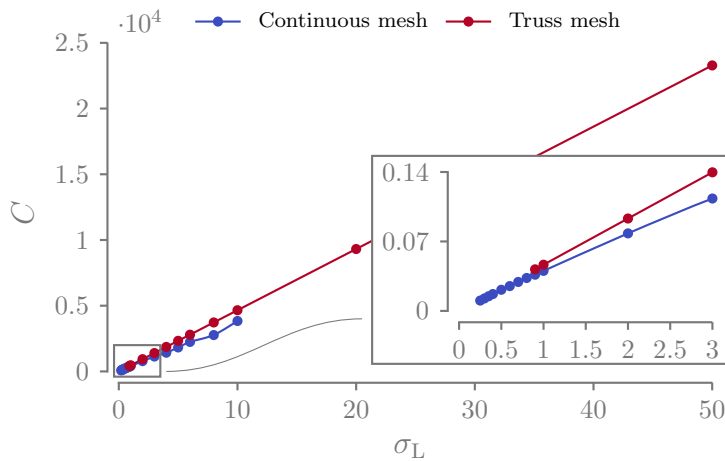


Figure 1.14: Compliance – Maximum material admissible plot for the continuous and truss discretizations.

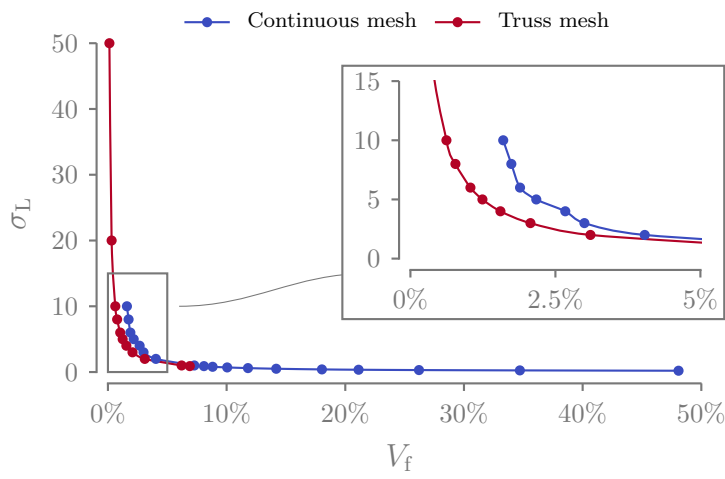


Figure 1.15: Maximum material admissible – Volume fraction plot for the continuous and truss discretizations.

the difference may be attributed to the non-linearity of the formulation, potentially causing the continuous approach to converge to a local minimum.

In Fig. 1.15 we plot the different volume fractions obtained for a given material admissible (the axis in the graph are swapped as for us the most important figure of merit is the volume fraction). The continuous mesh yields structures that are more massive for a given material limit. This outcome can be attributed not only to the aforementioned non-linearity in the formulation but also to another intriguing phenomenon. When dealing with volumes exceeding 1% (see Fig. 1.7b), we observe that the material in the topology-optimized structure is distributed across multiple elements, appearing somewhat “smeared”. In contrast, the truss representation concentrates all the structural mass along an imaginary line extending from one node to another, being more efficient.

We can also distinctly observe that the truss representation serves as the lower limit of the topology optimization for low volume fractions. Interestingly, both discretizations follow a similar trend for high-volume fractions, despite the significant disparity in their physical

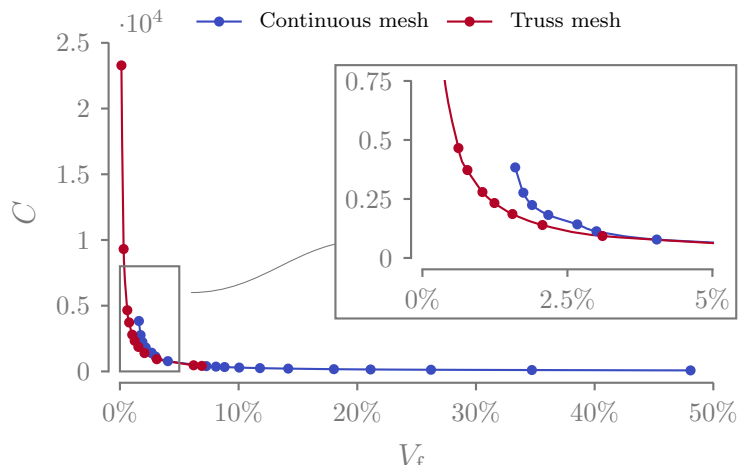


Figure 1.16: Compliance – Volume fraction plot for the continuous and truss discretizations.

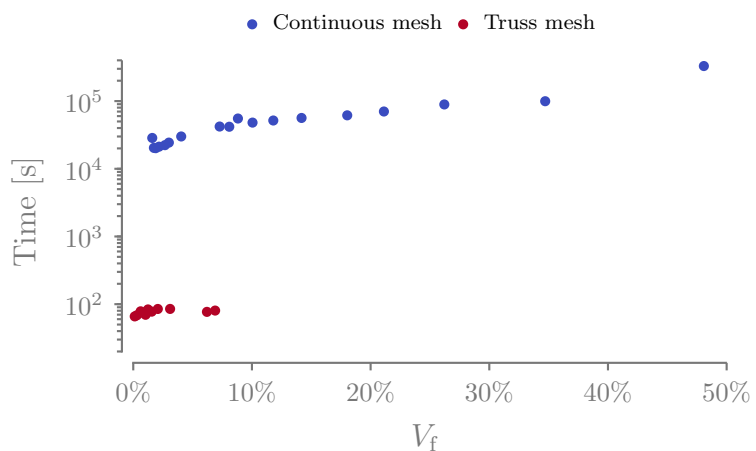


Figure 1.17: Time – Volume fraction plot for the continuous and truss discretizations.

description models. The very same trends can be observed watching the volume-compliance graph of Fig. 1.16.

Finally, in Fig. 1.17 we turn our attention to the time comparison between the two optimization methods. It is noteworthy that a consistent three-order of magnitude difference is observed between the two methods (days vs. minutes). Additionally, it's worth recalling that in the truss case, employing an extremely fine ground structure is not a necessity, which implies that the time difference could potentially be even bigger.

The notable difference in computation time for stress-based topology optimization (which is not self-adjoint in contrast to compliance minimization) points to the potential for exploring SAND topology optimization. While preliminary studies in this direction have been conducted [55], they lie beyond the scope of this thesis and will not be further investigated. It's worth mentioning that SAND approaches typically lead to a substantial increase in the number of design variables. However, in truss topology problems, this is less of a concern due to the ground structure approach, which results in numerous cross-sectional area design variables and fewer displacement-related ones. This, however, does not hold when dealing with a continuous

55. Munro et al. (2017), 'Local stress-constrained and slope-constrained SAND topology optimisation'

mesh.

To sum up, in comparing truss and continuous discretization methods, the advantages of truss structures become evident when considering the limitations of continuous discretization for the optimization of ultralight structures. One key drawback of continuous discretization is its increasing need for more elements as the desired level of refinement becomes finer at low volume fractions. Additionally, continuous discretization faces challenges with stress limits in optimized structures, which often exceed the specified admissible limits. Strategies exist to address this issue, but they come at the cost of increased computation time. Furthermore, stress constraints in continuous discretization are often defined for equivalent Von Mises stress, making it more challenging to distinguish between asymmetric bounds for tension and compression. Finally, truss structures are naturally subject to local buckling as a mode of failure [50], a phenomenon that can be more easily and directly modeled in a truss discretization.

While truss discretization offers advantages in terms of computational efficiency, it does come with certain limitations. In the minimum volume formulation, the problem is linear and cost-effective to solve. However, the linearity is lost when additional constraints, such as local buckling, are introduced. Moreover, the formulation does not inherently account for the kinematic compatibility of the problem. This limitation restricts its applicability to relatively simple problems and can pose issues when dealing with complex scenarios involving multiple loads or constraints that may lead to structures that are statically indeterminate.

Despite these challenges, we decided to favor truss discretization for our research. In the upcoming chapter, we will address and explore potential solutions to address its main limitations to further enhance its applicability and effectiveness.

1.3 CONCLUSION

Since the first developments of the topology optimization method, it has been recognized that "For moderately low volume fractions the lay-out of truss-like structures is predicted, but for very low volume fractions it is recommended that the traditional lay-out theory be employed..." [7]. However, the performance gap has never been quantified, nor has the domain of applicability been assessed. This is the primary motivation behind this chapter. Additionally, it's important to note that these assumptions were primarily based on compliance formulations and not on volume minimization formulations, which are more pertinent to the aeronautical context.

^{50.} Sigmund et al. (2016), 'On the (non-)optimality of Michell structures'

^{7.} Bendsøe (1989), 'Optimal shape design as a material distribution problem'

In this chapter, we introduced a volume minimization formulation applicable to both continuous and truss-like discretizations, aiming at a meaningful comparison. We established a standardized two-dimensional test case, the L-shaped beam, commonly used in stress-based optimization. We conducted multiple optimization runs for both discretization methods using various materials and subsequently compared the results, focusing primarily on volume fraction, compliance, and stress in the optimized structures.

Considering the limitations encountered with the continuous approach, particularly at very low volume fractions, we opted for the truss discretization method for our specific research problem. We also identified certain limitations inherent to truss discretizations, which will be addressed in the following chapter.

ENRICHING THE CLASSIC TTO FORMULATION WITH ADVANCED MECHANICAL CONSTRAINTS

2

Chapter 3 highlighted some inherent limitations of the truss modeling and the conventional optimization formulation of Truss Topology Optimization (TTO). These limitations include the minimum slenderness problem and the absence of local buckling and kinematic compatibility constraints. The primary objective of this chapter is to propose a comprehensive formulation capable of addressing these shortcomings. As we will observe, the resulting formulation, if solved in its original form, tends to yield solutions characterized by numerous active and intersecting bars. To mitigate this, we propose a two-step optimization algorithm that offers a means to reduce the solution complexity. Additionally, we introduce a heuristic designed to reduce the influence of the starting point within this two-step optimization algorithm.

In Section 2.1, we detail and model the various mechanical constraints applied in the context of TTO. Subsequently, in Section 2.2, a comprehensive formulation is presented along with an accompanying optimization algorithm. Through the utilization of this optimization algorithm, we are able to maintain control over the complexity of the design. Finally, in Section 2.3, we put the proposed formulation to the test, applying it to various 2D and 3D test cases sourced from the literature, as well as novel cases. The objective is to assess its capabilities and numerical performance.

2.1 ADVANCED MECHANICAL CONSTRAINTS

This section aims to introduce additional mechanical constraints that will be utilized in this study, to reduce the need for post-processing at the end of the optimization process, just before the manufacturing phase begins. We begin by addressing the issue of minimum slenderness, a side constraint that is imposed on the cross-sectional area of the active members to guarantee that the solution adheres to the truss modeling. Subsequently, we address the local buckling constraints, a critical failure mode observed in ultra-light truss structures. Particular attention is devoted to examining the stability of nodes within what are known as compressive chains. The combination of local buckling and nodal stability, a phenomenon known in the literature as topological buckling, is discussed. Furthermore, as we want our formulation to be as versatile as possible, we explore the extension of these constraints to accommodate multi-load cases. A challenge arises from the fact that the resulting structures are frequently statically indeterminate. To address this, we introduce an additional mechanical constraint

2.1 ADVANCED MECHANICAL CONSTRAINTS	25
2.2 OPTIMIZATION FORMULATION AND SOLVING STRATEGY	30
2.3 NUMERICAL APPLICATION	36
2.4 CONCLUSION	50

Part of the content presented in this chapter has been published [finish](#).

Table 2.1: Non-exhaustive list of the existing research in Truss Topology Optimization (TTO) with their corresponding scientific contributions.

Authors	Stress	Local Buckling	Topological buckling	Kinematic compatibility	Multi-load cases	Minimum slenderness
Dorn et al. (1964) [2]	x	-	-	-	-	-
Hemp (1973) [4]	x	-	-	-	x	-
Reinschmidt et al. (1974) [56]	x	x	-	~	-	-
Kirsch (1980) [57]	x	-	-	x	-	-
Oberndorfer et al. (1996) [58]	x	x	-	-	-	-
Silva Smith (1997) [59]	x	x	~	-	x	-
Achtziger (1999a, 1999b) [60, 61]	x	x	x	-	x	-
Stolpe (2004) [62]	x	x	-	x	x	-
Pritchard et al. (2005) [63]	x	-	-	-	x	-
Tyas et al. (2006) [64]	x	x	x	-	x	-
Descamps et al. (2014) [65]	x	x	x	-	x	-
Schwarz et al. (2018) [66]	x	x	-	-	-	-
Cai et al. (2022) [67]	x	x	x	-	-	-
Present work	x	x	x	x	x	x

known as "kinematic compatibility" to ensure that the predicted force field aligns with the displacements of the structure.

In Table 2.1, we provide an overview of historical and contemporary research in the field of TTO, along with their respective scientific contributions. This serves to highlight the necessity for a more comprehensive formulation that incorporates these mechanical constraints, reducing the gap between the optimized design and the actual manufactured structure.

2.1.1 MINIMUM SLENDERNESS CONSTRAINTS

As previously discussed in Section 1.2.2, the TTO method shows numerous limitations due to its reliance on the truss model. Therefore, the resulting structures may not be acceptable if the model falls outside the bounds of this idealization. To better study this limit, as outlined in Section 1.2.2, we introduced a metric called bar slenderness, which is defined as follows:

$$\lambda = \frac{\ell}{R_g}, \quad (2.1)$$

where R_g represents the gyration radius of the cross-sectional area, defined as $R_g = \sqrt{I/a_i}$. The primary objective of this section is to introduce an upper limit constraint on the cross-sectional area design variable. This constraint prevents a bar from exceeding the bounds of its idealized model, thereby enhancing the optimization process's robustness.

Remembering that for a circular cross-section $I = \pi r_i^4/4$, we can write

$$R_{g,i} = \frac{r_i}{2}. \quad (2.2)$$

The minimum slenderness limit constraints are then stated as:

$$a_i \leq \frac{4\pi\ell_i^2}{\lambda_{\max}}, \quad \forall i \in [1, \dots, N_{\text{el}}] \quad (\mathbf{g}_{\text{slend}})$$

for a fixed λ_{\max} . In this thesis we set $\lambda_{\max} = 15$.

2.1.2 LOCAL AND TOPOLOGICAL BUCKLING CONSTRAINTS

Adding local buckling constraints to the optimization formulation is fundamental, as ultralight truss structures are often dominated by this mode of failure [50]. By imposing local buckling constraints over a TTO problem (where the lower bound for the members' cross-sectional areas is 0), the optimization domain becomes disjointed [68]. The solution is to be searched inside a degenerate space of the design space of the optimization, known in the literature as singular optimum [69]. Stolpe [70] showed how using the Simultaneous Analysis and Design (SAND) formulation with local buckling and kinematic compatibility constraints, it is possible to find well-optimized structures without the use of relaxation techniques. The authors, however, point out how the solution is still very sensitive to the initialization point of the Non-Linear Programming (NLP) formulation. The local buckling constraints \mathbf{g}_{buck} are stated using Euler's critical load formula as:

$$q_i + \frac{s_i a_i^2}{\ell_i^2} \geq 0 \quad \forall i \in [1, \dots, N_{\text{el}}], \quad (\mathbf{g}_{\text{buck}})$$

where s_i is a parameter dependent on the member material and section topology as follows:

$$s_i = \pi^2 E \beta_i. \quad (2.3)$$

$\beta_i = I_i/a_i^2$ is a positive constant dependent on the moment of inertia and the section of the i -th bar, and E is Young's modulus of the material. Assuming that the shape of the cross-section is identical over the whole structure and is independent of a , it follows that $\beta_i = \beta$ and $s_i = s$, $\forall i \in [1, \dots, N_{\text{el}}]$.

Direct application of the local buckling constraint \mathbf{g}_{buck} in the optimization formulation tends to create "chains" of unstable compressive members [71–73]. This problem is known in the literature as topological buckling [60], as the definition of the compressive chains is a function of the topology of the structure, and is one of the elements of the nodal stability of the structure. Additional forms of structure instability, such as global buckling [74–77] or the use of lateral perturbing forces to obtain nodal stability [64, 78] have been studied in the literature. However, since they are beyond the scope of this work, they will not be discussed further.

To illustrate the topological buckling phenomenon, we consider the

- 50. Sigmund et al. (2016), 'On the (non-)optimality of Michell structures'
- 68. Cheng (1995), 'Some aspects of truss topology optimization'
- 69. Guo et al. (2001), 'A new approach for the solution of singular optima in truss topology optimization with stress and local buckling constraints'
- 70. Stolpe et al. (2003), 'A note on stress-constrained truss topology optimization'
- 71. Bendsøe (1995), 'Optimization of Structural Topology, Shape, and Material'
- 72. Zhou (1996), 'Difficulties in truss topology optimization with stress and local buckling constraints'
- 73. Rozvany (1996), 'Difficulties in truss topology optimization with stress, local buckling and system stability constraints'
- 60. Achtziger (1999), 'Local stability of trusses in the context of topology optimization Part I'
- 74. Ben-Tal et al. (2000), 'Optimal Design of Trusses Under a Nonconvex Global Buckling Constraint'
- 75. Kočvara (2002), 'On the modelling and solving of the truss design problem with global stability constraints'
- 76. Neves et al. (1995), 'Generalized topology design of structures with a buckling load criterion'
- 77. Ferrari et al. (2021), 'Topology optimization with linearized buckling criteria in 250 lines of Matlab'
- 64. Tyas et al. (2006), 'Practical plastic layout optimization of trusses incorporating stability considerations'
- 78. Mela (2014), 'Resolving issues with member buckling in truss topology optimization using a mixed variable approach'

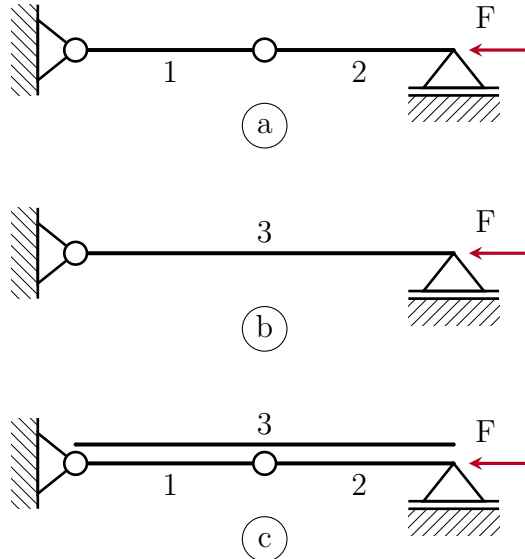


Figure 2.1: The three ground structures loaded in compression are used to highlight the topological buckling problem in TTO. (a) Two-bar ground structure loaded in compression; (b) single bar ground structure; (c) overlap of the *a* and *b* ground structures.

case shown in Fig. 2.1a. It consists of a ground structure with $M = 3$ nodes and $N_{\text{el}} = 2$ bars with length $\ell_1 = \ell_2 = \ell$, and a compressive load of magnitude F applied at the right-hand side node. For this trivial structure, we can state that $q_1 = q_2 = F$ and thus $a_1 = a_2 = a$. We suppose here that the allowables of the material are such that the local buckling (and not the stress) is the most limiting failure criterion for the bars. Assuming that the shape of the section is equal, the local buckling constraints are written as:

$$q_i \geq -\frac{sa^2}{\ell^2}, \quad i \in [1, 2]. \quad (2.4)$$

However, the structure is unstable because the vertical force equilibrium equation evaluated on the central hinge is satisfied only in an ideal case where no structural imperfections are taken into account.

If the hinge between bars 1 and 2 is deleted, we obtain the structure pictured in Fig. 2.1b with $\ell_3 = 2\ell$. The local buckling constraints for bar 3 are thus:

$$q_3 \geq -\frac{sa_3^2}{(2\ell)^2}. \quad (2.5)$$

Combining Equations 2.4, 2.5 and observing that $q_1 = q_2 = q_3 = F$, it is now trivial to demonstrate that $a_3 = 2a$. Constraint 2.5 leads, then, to more voluminous structures compared to constraint 2.4. For that reason, even if we consider the ground structure given in Fig. 2.1c composed by the superposition of the ground structures in Fig. 2.1a and Fig. 2.1b, the optimization with a uniform initialization tends to converge to the solution $a^* = [a, a, 0]$, unstable but lighter than the physical solution $a_p^* = [0, 0, 2a]$.

The easiest way to get rid of the instability of the compressive chains is to post-process the optimized structure and remove the unstable

hinges between the compressive bars. Doing that, the local buckling constraints are not satisfied anymore as the effective buckling length has increased. It is, then, necessary to calculate the section of the new compressive bars to comply with the newly introduced buckling constraints. As extensively shown by Achtziger [61], this post-processing phase leads to structures that are less optimal compared to the ones we could obtain if we take into account the topological buckling in the optimization in the first place.

For that reason, Achtziger proposes an update strategy to modify the length used to evaluate the critical buckling force of g_{buck} as follows:

$$\ell_i^*(\boldsymbol{a}) := \begin{cases} \ell_i & \text{if } i \notin \mathcal{C}_{l,r}(\boldsymbol{a}) \\ \sum \ell_r \mid r \in \mathcal{C}_{l,r}(\boldsymbol{a}) & \text{otherwise,} \end{cases} \quad (2.6)$$

where r represents the r -th bar of the l -th compression chain of the structure. The topology-dependent set $\mathcal{C}_{l,r}(\boldsymbol{a})$ is defined as the set of r member indexes of the l -th buckling chain. As internal forces on buckling chains are constant, only the buckling length of the first member of the chain ($\ell_i^*(\boldsymbol{a})$ with $i \in \mathcal{C}_{l,1}(\boldsymbol{a})$) is modified. Additionally, we add the following side constraints on the other members of the l -th chain to ensure feasibility:

$$a_r \geq a_{r=1} \quad r \in \mathcal{C}_{l,r}(\boldsymbol{a}), \quad \forall r \neq 1. \quad (2.7)$$

2.1.3 KINEMATIC COMPATIBILITY CONSTRAINTS

To optimize test cases that result in statically indeterminate structures, such as structures loaded with multiple load cases or imposed symmetries, we add an additional mechanical constraint called kinematic compatibility [79, 80]. Compatibility can be imposed as a nonlinear constraint in the optimization formulation [57], or can be taken into account by prestressing the initial structure [81].

The kinematic compatibility constraints restrict the displacement field $\boldsymbol{U} = [U_1, \dots, U_{N_{\text{dof}}}]^T$ in such a way that strains ε_i and internal stresses σ_i comply with Hooke's law $\sigma_i = E_i \varepsilon_i$ with $i \in [1, \dots, N_{\text{el}}]$. Recalling that in a truss the relationship between nodal displacements and member deformations is $\boldsymbol{b}_i^T \boldsymbol{U} = \ell_i \varepsilon_i$ with \boldsymbol{b} as the i -th column of the \boldsymbol{B} matrix, we can formulate the kinematic compatibility constraints g_{comp} as:

$$q_i - \frac{a_i E_i}{\ell_i} \boldsymbol{b}_i^T \boldsymbol{U} = 0 \quad \forall i \in [1, \dots, N_{\text{el}}]. \quad (g_{\text{comp}})$$

Kinematic compatibility constraints are non-linear as the design variable \boldsymbol{q} is dependent on \boldsymbol{a} and \boldsymbol{U} .

61. Achtziger (1999), 'Local stability of trusses in the context of topology optimization Part II'

79. Kirsch (1989), 'Optimal topologies of truss structures'

80. Rozvany et al. (1995), 'Layout Optimization of Structures'

57. Kirsch (1980), 'Optimal design of trusses by approximate compatibility'

81. Kirsch (1989), 'Effect of Compatibility and Prestressing on Optimized Trusses'

2.2 OPTIMIZATION FORMULATION AND SOLVING STRATEGY

In this section, we propose an innovative TTO formulation developed specifically to minimize the mass of 3D ultralight truss structures, taking into account maximum stress, topological buckling, kinematic compatibility, and minimum slenderness constraints. Combining Formulation \mathbb{P}_0 with Equations g_{buck} , g_{slend} , 2.6, 2.7, and g_{comp} , Formulation \mathbb{P}_1 is stated in terms of members' cross-sectional area \mathbf{a} , member forces \mathbf{q} and nodal displacements \mathbf{U} as follows:

$$\begin{aligned}
 & \min_{\mathbf{a}, \mathbf{q}^0, \dots, \mathbf{q}^{N_p}, \mathbf{U}^0, \dots, \mathbf{U}^{N_p}} \quad V = \boldsymbol{\ell}^T \mathbf{a} \\
 & \text{s.t.} \quad \mathbf{B}\mathbf{q}^p = \mathbf{f}^p \quad \forall p \in [0, \dots, N_p] \\
 & \quad \mathbf{q}^p = \frac{\mathbf{a}\mathbf{E}}{\boldsymbol{\ell}} \mathbf{b}^T \mathbf{U}^p \quad \forall p \in [0, \dots, N_p] \\
 & \quad \mathbf{q}^p \geq -\frac{s\mathbf{a}^2}{\ell^{*2}} \quad \forall p \in [0, \dots, N_p] \tag{\mathbb{P}_1} \\
 & \quad -\sigma_c \mathbf{a} \leq \mathbf{q}^p \leq \sigma_t \mathbf{a} \quad \forall p \in [0, \dots, N_p] \\
 & \quad a_r \geq a_{r=1} \quad r \in \mathcal{C}_{l,r}(\mathbf{a}) \\
 & \quad 0 \leq \mathbf{a} \leq \frac{4\pi\boldsymbol{\ell}^2}{\lambda_{\max}}
 \end{aligned}$$

60. Achtziger (1999), 'Local stability of trusses in the context of topology optimization Part I'

5. Sankaranarayanan et al. (1994), 'Truss topology optimization with simultaneous analysis and design'

The formulation has been extended to multiple load cases given by N_p external loads vector $\mathbf{f}^0, \dots, \mathbf{f}^{N_p}$ and the resulting internal forces $\mathbf{q} = [\mathbf{q}^0, \dots, \mathbf{q}^{N_p}]$ and displacements $\mathbf{U} = [\mathbf{U}^0, \dots, \mathbf{U}^{N_p}]$. This proposed formulation expands the multiple load cases formulation of Achtziger [60] with kinematic compatibility constraints, permitting the correct evaluation of the mechanical state of statically indeterminate structures.

The formulation follows the SAND approach [5], where, in addition to the members' cross-sectional area \mathbf{a} , the member forces \mathbf{q} and the structure displacements \mathbf{U} are used as state variables. One of the advantages of SAND approach is that the state variables are independent of each other and, thus, the sensitivity calculation of the constraints functions is usually simpler and leads to sparse partial derivatives. Additionally, compared to Nested Analysis and Design (NAND) formulations, the problem stays well-posed even if the cross-sectional area goes to 0. As the linear system $\mathbf{K}\mathbf{U} = \mathbf{f}$ is never explicitly solved during the optimization, it is not necessary to impose a lower bound on the members' cross-sectional area \mathbf{a} to avoid a singular stiffness matrix. The last important advantage is that thanks to \mathbf{U} being design variables, it is trivial to add bound constraints on the nodal displacements of the structure if needed.

2.2.1 OPTIMIZATION STRATEGY

Formulation \mathbb{P}_1 presents multiple constraints and design variables for every physical bar of the ground structure. The quantity of constraints creates a highly non-linear design space and it proved to be hard for the optimizer to bring to zero the value of the cross-sectional areas. If a NLP optimizer is directly used on Formulation \mathbb{P}_1 , the resulting structure will be composed of a multitude of intersecting bars. The optimizer is, thus, working like it is performing sizing optimization instead of topology optimization.

Inspired by the early works by Reinschmidt [56], we propose a novel two-step optimization strategy in which a first optimization solving a relaxed formulation is used to find a good starting point for the second optimization, solving the full Formulation \mathbb{P}_1 . Doing that way, the first optimization explores extensively the relaxed and more regular design space and finds simpler structures, while the second optimization refines the solution imposing additional mechanical constraints. The complete solving strategy is graphically presented in Fig. 2.2.

56. Reinschmidt et al. (1974), 'Applications of linear programming in structural layout and optimization'

In the first step, Problem \mathbb{P}_1 is relaxed: kinematic compatibility constraints are omitted. We call this relaxed Problem \mathbb{P}_2 . Problem \mathbb{P}_2 is solved using a Sequential Linear Programming (SLP) method by iteratively linearizing the local buckling constraints. A heuristic strategy called Reinitialization is iteratively used to reduce the influence of the starting point a_0 . The resulting structure described by the design variables vector \tilde{x}^* is then post-processed, removing the members whose optimized area is below a fixed cross-sectional area threshold value. The structures generated by solving the relaxed Problem \mathbb{P}_2 proved to be simpler i.e. fewer active members compared to directly solving \mathbb{P}_1 with a NLP optimizer. If the solution is not statically indeterminate the optimization is completed as the kinematic compatibility constraints g_{comp} are automatically satisfied and, thus, used to evaluate the optimal displacements.

Otherwise, a second step is needed. Firstly, the ground structure of the problem is simplified, removing all the members that do not appear in the solution of the relaxed Problem \mathbb{P}_2 i.e. avoiding the reintroduction of members discarded by the SLP step. Then, the kinematic compatibility and the exact local buckling constraints are restored, and Problem \mathbb{P}_1 is solved in its original form on the simplified ground structure using a NLP optimizer. The initial values for the cross-sectional areas are the solution \tilde{x}^* of Problem \mathbb{P}_2 .

2.2.2 FIRST STEP: SLP OPTIMIZATION

The first step of the proposed optimization strategy is here described in detail. The relaxed Problem \mathbb{P}_2 obtained by omitting g_{comp} and the

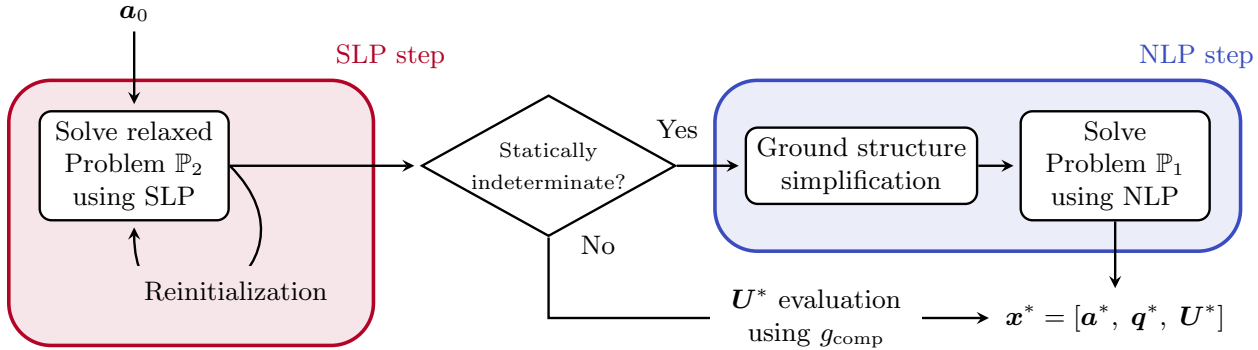


Figure 2.2: Flowchart of the two-step optimization strategy used to solve Problem \mathbb{P}_1 .

displacements \mathbf{U} in Formulation \mathbb{P}_1 is stated as:

$$\begin{aligned}
 \min_{\mathbf{a}, q^0, \dots, q^p} \quad & V = \ell^T \mathbf{a} \\
 \text{s.t.} \quad & \mathbf{B} \mathbf{q}^p = \mathbf{f}^p \quad \forall p \in [0, \dots, N_p] \\
 & \mathbf{q}^p \geq -\frac{s \mathbf{a}^2}{\ell^{*2}} \quad \forall p \in [0, \dots, N_p] \\
 & -\sigma_c \mathbf{a} \leq \mathbf{q}^p \leq \sigma_t \mathbf{a} \quad \forall p \in [0, \dots, N_p] \\
 & a_r \geq a_{r=1} \quad r \in \mathcal{C}_{l,r}(\mathbf{a}) \\
 & 0 \leq \mathbf{a} \leq \frac{4\pi\ell^2}{\lambda_{\max}}
 \end{aligned} \tag{\mathbb{P}_2}$$

66. Schwarz et al. (2018), 'Efficient size and shape optimization of truss structures subject to stress and local buckling constraints using sequential linear programming'

Since the objective function and all of its constraints are linear, except for the buckling constraint, this problem is solved by iteratively linearizing the non-linear buckling constraints and using a SLP algorithm. Following the work of [66], the Euler's critical load is iteratively updated using a first-order Taylor expansion for every i member with cross-sectional area a_i^k at the iteration k in the neighborhood of the point P_k (see Fig. 2.3):

$$\tilde{q}_{i,k}^{\text{cr}} = q_{i,k}^{\text{cr}}(a_i^k) + (a_i^{k+1} - a_i^k) \left. \frac{\partial q_{i,k}^{\text{cr}}(a_i^k)}{\partial a} \right|_{a=a_i^k} \tag{2.8}$$

where a_i^{k+1} represent the design variable of the SLP at the current iteration and $q_{i,k}^{\text{cr}}(a_i^k) = -s(a_i^k)^2/\ell_i^{*2}$ represents the Euler's critical load with cross-sectional area a_i^k and modified buckling length ℓ_i^* .

The linearized local buckling constraints \tilde{g}_{buck} are then stated as:

$$q_i \geq \tilde{q}_{i,k}^{\text{cr}}, \text{ with } \tilde{q}_{i,k}^{\text{cr}} = -\frac{s a_i^k (2a_i^{k+1} - a_i^k)}{\ell_i^{*2}} \quad \forall i \in [1, \dots, N_{\text{el}}], \quad (\tilde{g}_{\text{buck}})$$

where superscript \sim indicates linearized functions and corresponding variables.

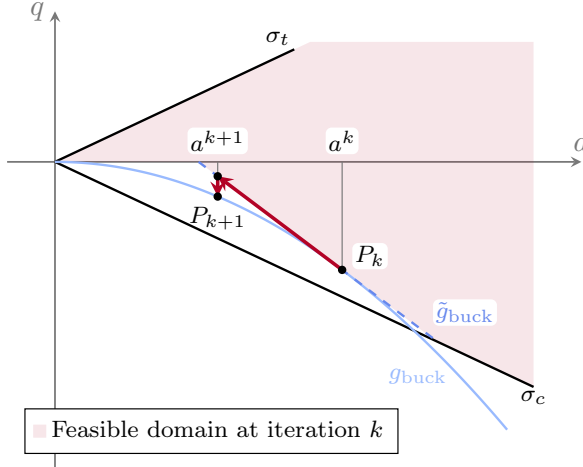


Figure 2.3: Linearization of the local buckling constraints for a single bar.

We can now state the relaxed linearized sub-problem $\tilde{\mathbb{P}}_2$ obtained substituting g_{buck} with \tilde{g}_{buck} in Formulation \mathbb{P}_2 :

$$\begin{aligned}
 & \min_{a, q^0, \dots, q^p} \quad V = \ell^T a \\
 \text{s.t.} \quad & Bq^p = f^p \quad \forall p \in [0, \dots, N_p] \\
 & q^p \geq -\frac{s a^k (2a^{k+1} - a^k)}{\ell^*{}^2} \quad \forall p \in [0, \dots, N_p] \quad (\tilde{\mathbb{P}}_2) \\
 & -\sigma_c a \leq q^p \leq \sigma_t a \quad \forall p \in [0, \dots, N_p] \\
 & a_r \geq a_{r=1} \quad r \in \mathcal{C}_{l,r}(a) \\
 & 0 \leq a \leq \frac{4\pi\ell^2}{\lambda_{\max}}
 \end{aligned}$$

Since the objective function and all of its constraints are linear, we can approximate the solution of \mathbb{P}_2 by iteratively solving the sub-problem $\tilde{\mathbb{P}}_2$. At every iteration k , the vector of cross-sectional areas a^k is used to evaluate the linearization point P_k and calculate the set of linearized buckling constraints \tilde{g}_{buck} (see Fig. 2.3). The sub-problem $\tilde{\mathbb{P}}_2$ is, then, solved using a Linear Programming (LP) solver, and the updated vector of cross-sectional areas a^{k+1} is used to evaluate the set of linearized buckling constraints of the $k + 1$ iteration. These steps are repeated until convergence i.e. when $\|\Delta x\|_\infty \leq \text{tol}_{slp}$, where Δx represents the difference of the design variable vector x between two successive iterations. The vector x is scaled so that the difference Δx gives coherent results for the different physical quantities (cross-sectional areas and forces).

2.2.3 HANDLING LOCAL MINIMA: REINITIALIZATION STRATEGY

If at the end of iteration $k - 1$ the cross-sectional area of bar i , a_i^k , becomes very small, the gradient of the corresponding local buckling constraint at iteration k will tend towards 0 and the feasible domain will be extremely reduced (see Fig. 2.4). Any bar with near-zero sections will remain as such in future iterations since there is no

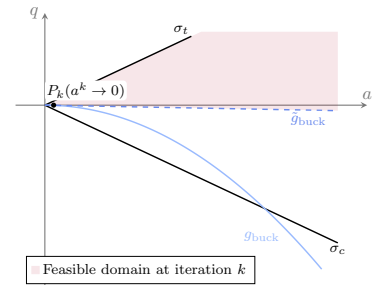


Figure 2.4: The linearized buckling constraints (blue dashed line) limit the design space of successive iterations when evaluated on compressive bars with very small areas. Additionally, the gradient of the linearized buckling constraint tends to 0.

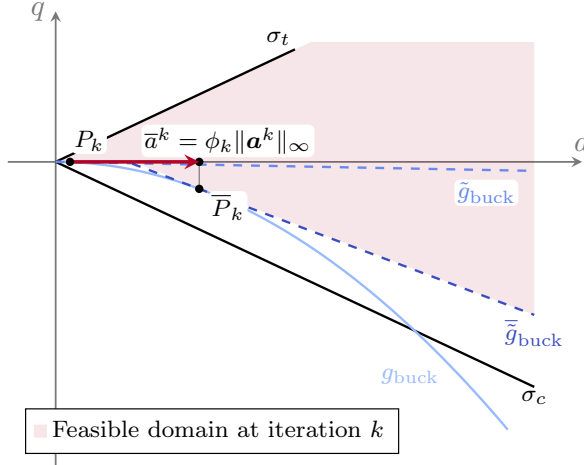


Figure 2.5: The reinitialization strategy modifies the linearization point of the members with a small area to promote their reintroduction in the optimization problem.

incentive for the SLP optimizer to increase its value. This is one of the possible reasons why the SLP optimizer gets stuck in local minima.

Subsequently, we propose a heuristic strategy to reinitialize the small cross-sectional area values a^k used to evaluate the linearized local buckling constraints \tilde{g}_{buck} at iteration k . The strategy is called multiple times during the optimization when the solver converges to a minimum, i.e. when $\|\Delta x\|_\infty \leq \text{tol}_{slp}$. It affects only the cross-sectional areas that are smaller than a fraction value τ of the maximum value at iteration k , $\|a^k\|_\infty$. The updated cross-sectional area \bar{a}^k used to evaluate the linearization point \bar{P}_k is updated as follows:

$$\bar{a}_i^k := \begin{cases} \phi_n \|a^k\|_\infty & \text{if } a_i^k \leq \tau \|a^k\|_\infty \\ a_i^k & \text{otherwise.} \end{cases} \quad (2.9)$$

The effects of this approach are shown in Fig. 2.5, where it is clear that updating the constraint \tilde{g}_{buck} with \bar{g}_{buck} reduces the gap between the original and the linearized design space and permits the exploration of new solutions. Additionally, the gradient of the constraint is restored to a non-zero value.

The ϕ_n parameter is used in Equation 2.9 to influence how much the reinitialization heuristic modifies the original formulation. Subsequently, to reach convergence, we propose a continuation scheme on ϕ_n to reduce its impact on the optimization following an exponential decay law:

$$\phi_n = \phi_{n-1}^\beta \quad \forall n \in [1, \dots, n_{\max}], \quad (2.10)$$

where n_{\max} represent the maximum number of reinitialization calls and the β parameter control the steepness of the exponential progression. In that way, as the number of calls to the reinitialization strategy increases, its influence on the original formulation decreases.

The complete SLP strategy with reinitialization used to solve Problem \mathbb{P}_2 is presented in Fig. 2.6, where the SLP optimized design variable vector is noted as $\tilde{x}^* = [\tilde{a}^*, \tilde{q}^*]$.

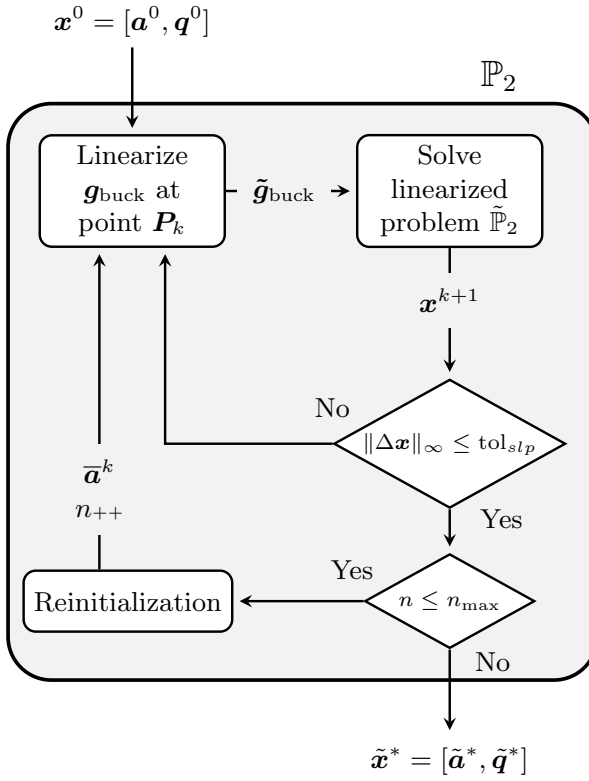


Figure 2.6: Flowchart of the SLP strategy with reinitialization used to solve Problem \mathbb{P}_2 .

2.2.4 SECOND STEP: NLP OPTIMIZATION

If only one load case and no particular symmetries are imposed on the initial ground structure, the SLP solution $\tilde{\mathbf{x}}^*$ is not statically indeterminate [79, 80]. In that case, it is trivial to evaluate the displacements using g_{comp} and the optimization is complete. However, if this is not the case, the stability of the structure is to be tested.

- 79. Kirsch (1989), 'Optimal topologies of truss structures'
- 80. Rozvany et al. (1995), 'Layout Optimization of Structures'

The stability of the SLP-optimized structure is assessed by evaluating the Degree of Static Indeterminacy (DSI) of the truss using Maxwell's criterion:

$$DSI = N_{\text{el}} - N_{\text{DOF}} - r \quad (2.11)$$

with r the number of fixed Degrees Of Freedom (DOFs) of the test case. If $DSI \leq 0$, the number of equilibrium equations is less than or equal to the number of the internal forces and Equation g_{comp} suffices to evaluate the correct displacements of the truss. If, however, $DSI > 0$, the truss is potentially statically indeterminate and additional nonlinear constraints must be added to ensure the structure's kinematic compatibility. The optimization is then performed again. We call this second step the NLP step (see Fig. 2.2).

To mitigate the risk of becoming trapped in local minima, the NLP optimizer is employed on a reduced design space. The solution $\tilde{\mathbf{x}}^*$ of the SLP serves the purpose of simplifying the initial ground structure, thereby eliminating elements from the NLP optimization that fall

below the specified threshold value a_{thr} :

$$a_i < a_{\text{thr}} \quad \forall i, \text{ with } a_{\text{thr}} = \chi \max(\tilde{\mathbf{a}}^*), \quad (2.12)$$

with the parameter χ called the cross-sectional area threshold value.

An elastic Finite Element Analysis (FEA) based on the direct stiffness method is performed to provide a correct estimate of forces and displacements caused by the external forces on the solution of Problem \mathbb{P}_2 for the initial point of the optimization. The initial displacement vector \mathbf{U}^0 is calculated as the unique solution to:

$$\mathbf{f} = \mathbf{B}^T \mathbf{q} = \mathbf{B}^T \mathbf{D} \boldsymbol{\epsilon} = \mathbf{B}^T \mathbf{D} \mathbf{B} \mathbf{U}^0 = \mathbf{K} \mathbf{U}^0. \quad (2.13)$$

where \mathbf{K} is the stiffness matrix of the truss, defined as $\mathbf{K} = \mathbf{B}^T \mathbf{D} \mathbf{B}$, with $\mathbf{D} = \text{diag}(E(\tilde{\mathbf{a}}^* + \delta \mathbf{e})/\ell)$, $\mathbf{e} = [1, \dots, 1]^T$, and $\delta = 10^{-12}$. This last term is added as the structures coming from the SLP step could result in a mechanism with respect to load cases different from the one used for the optimization [2]. Then the initial member forces vector \mathbf{q}^0 is evaluated using g_{comp} . $\tilde{\mathbf{a}}^*$, \mathbf{q}^0 and \mathbf{U}^0 are used as the starting point of the full NLP formulation where the kinematic compatibility and the exact local buckling formulation are restored. The NLP solver finally outputs the optimized structure variables $\mathbf{x}^* = [\mathbf{a}^*, \mathbf{q}^*, \mathbf{U}^*]$.

2. Dorn et al. (1964), 'Automatic design of optimal structures'

2.3 NUMERICAL APPLICATION

In this section, the proposed method is benchmarked against four classical and innovative test cases. Firstly, we show how the proposed two-step solution strategy with reinitialization reduces the influence of the starting point on the optimization result compared to the direct NLP optimization of Problem \mathbb{P}_1 . Additionally, as the response surface of the SLP of the proposed method is more regular than the original NLP, the two-step solution strategy generates simple structures i.e. with a low number of active bars, as it is efficient at driving the cross-sectional areas to zero. To show that, we implement and optimize the ten-bar truss and the 2D cantilever beam, two of the most common benchmarks in TTO with buckling constraints. Secondly, to show the ability of the proposed method to work on structures with multiple load cases we implemented a modified ten-bar truss test case where several load cases are applied to the same ground structure. Finally, to assess the computational efficiency and to validate the proposed strategy on a large-scale structure, we optimize a three-dimensional wingbox test case based on the NASA Common Research Model (CRM) with multiple discretization refinement.

The test cases are optimized using different resolution strategies. The proposed method is compared against the direct NLP optimization of Problem \mathbb{P}_1 , denoted in our analysis as NLP. The proposed two-step

resolution strategy is implemented with three different maximum numbers of reinitialization calls n_{\max} : no reinitialization (2S-0R) with $n_{\max} = 0$, one call of reinitialization (2S-1R) with $n_{\max} = 1$, and finally five calls of reinitialization (2S-5R) with $n_{\max} = 5$. The reinitialization magnitude parameter ϕ is set up using Equation 2.10 and the parameters listed in Table 2.2, leading to $\phi = 0.8000$ for the 2S-1R algorithm and to $\phi = [0.8000, 0.6400, 0.4096, 0.1677, 0.0281]$ for the five reinitialization calls of 2S-5R.

The optimizations are performed using the Python package CVXPY 1.2.2 [48] with the ECOS 2.0.7 [49] solver to solve the relaxed LP Problem $\tilde{\mathbb{P}}_2$. The NLP Problem \mathbb{P}_1 is solved using cyipopt [82], a Python wrapper for IPOPT 3.14.11 [83], a large-scale nonlinear optimization package using PARDISO 6.0 [84] as linear solver. The Jacobian and the Hessian of the Lagrangian of the NLP step are calculated at every optimization iteration to allow faster convergence. As every state variable of the optimization is independent of the others, these responses are derived analytically and will not be detailed there. The stopping criterion used for the SLP and NLP optimizations are $\|\Delta \mathbf{x}\|_\infty \leq \text{tol}_{slp}$, and $\|\Delta_{NLP}\|_\infty \leq \text{tol}_{nlp}$, with $\text{tol}_{slp} = 10^{-6}$ and $\text{tol}_{nlp} = 10^{-4}$ respectively. Δ_{NLP} represents the scaled NLP error, a more comprehensive value used by IPOPT to take into account the optimality of the solution and the constraints violation. The objective function is scaled so that the initial volume is 1000, the areas are in the interval $[0, 1000]$, the initial forces in $[0, 1000]$, and the displacement in $[0, 1000]$ for the SLP and the NLP. The full list of parameters used to set up the variable scaling, the SLP optimization, the reinitialization, and the NLP optimization is listed in Table 2.2. Several additional parameters are used in the NLP step for cyipopt and IPOPT:

- ▶ `mu_strategy` is set to `adaptive`
- ▶ `grad_f_constant` is set to `yes`
- ▶ `hessian_constant` is set to `yes`
- ▶ `alpha_for_y` is set to `min-dual-infeas`
- ▶ `linear_solver` is set to `pardiso`
- ▶ `expect_infeasible_problem` is set to `yes`
- ▶ `bound_push` is set to `1e-12`
- ▶ `constr_viol_tol` is set to `1e-6`
- ▶ `nlp_scaling_method` is set to `user-scaling`.

The optimizations presented in this section are performed on a notebook equipped with an Intel Core™ i5-9400H Processor @ 2.50 GHz (4 cores) and 16 GB of RAM. Additionally, the load cases, the starting point, and the result data of all the presented test cases are available in the reference data set [85].

2.3.1 L-SHAPED BEAM

To assess the effectiveness of the proposed minimum slenderness limit, we conducted a new round of optimization on the L-shaped beam

⁴⁸. Diamond et al. (2016), 'CVXPY: A Python-Embedded Modeling Language for Convex Optimization'

⁴⁹. Domahidi et al. (2013), 'ECOS: An SOCP solver for embedded systems'

⁸². Moore et al. (2018), 'cyipopt: Cython interface for the interior point optimizer IPOPT'

⁸³. Wächter et al. (2006), 'On the implementation of an interior-point filter line-search algorithm for large-scale nonlinear programming'

⁸⁴. Alappat et al. (2020), 'A Recursive Algebraic Coloring Technique for Hardware-efficient Symmetric Sparse Matrix-vector Multiplication'

⁸⁵. Stragiotti (2023), 'Truss Topology Optimization with Topological Buckling Constraints Data Set'

Table 2.2: Values and description of the parameters used for the SLP and NLP optimizations.

Parameter	Value	Description
tol_{slp}	10^{-6}	Stopping criterion SLP
tol_{nlp}	10^{-4}	Stopping criterion NLP
$\text{max}_{\text{it,SLP}}$	400	Maximum iterations of the SLP algorithm
$\text{max}_{\text{it,NLP}}$	5000	Maximum iterations of the NLP algorithm
χ	10^{-6}	Threshold for the ground structure reduction
τ	0.05	Threshold for the reinitialization
ϕ_0	0.8	Initial reinitialization magnitude parameter
β	2	Index of the exponential decay law

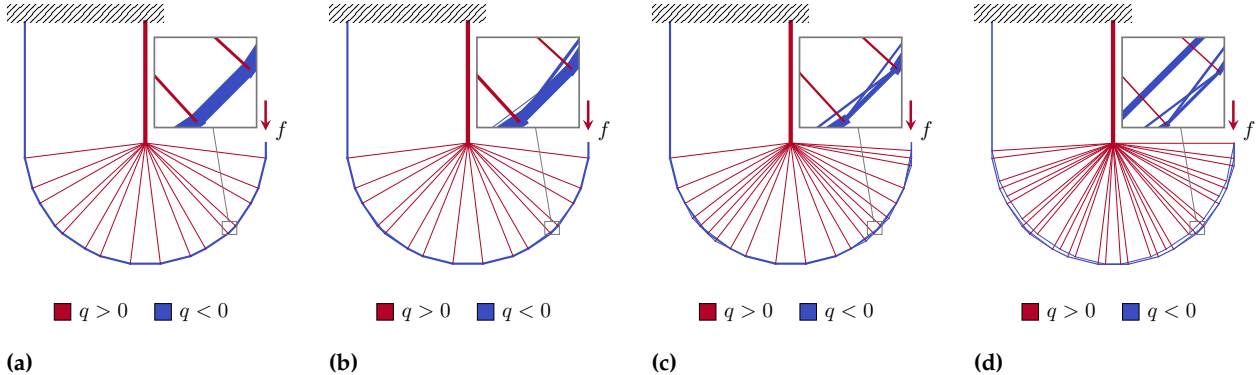


Figure 2.7: Topology of the optimized truss structures for different material admissibles $\sigma_L = 1.0, 0.8, 0.3$ and 0.2 with a minimum slenderness limit $\lambda < 15$.

described in Section 1.2.2. In the Fig. 2.7, we present the optimized structures obtained using this modified formulation and the stress limits σ_L values of 1, 0.8, 0.3, and 0.2. The first two values have already been used and the results have been presented in Table 1.3. They highlighted the limits of Formulation \mathbb{P}_0 when imposing a specified slenderness limit ($\lambda < 15$). The last two values are introduced here to test how the g_{slend} constraints affect the truss topology for extreme cases.

A major focus is put on the shorter bar of the optimized structures to observe how the solution evolved. We observe a redistribution of the same load across multiple smaller bars. More bars became active because there is an upper limit on the cross-sectional area (and thus the force) they can withstand. The four structures present $N_{\text{el,sl}} = 34, 38, 56$ and 79 active bars, respectively.

In Table 2.3 we compared the new designs limited in minimum slenderness (noted in the table with the 'sl' subscript) to the ones presented in Section 1.2.2 and found that the new designs meet the bar model's slenderness requirements correctly. The number of active bars increases along with the calculation time, but the volume remains nearly the same, indicating there are many solutions with similar volumes. Adding this upper bound constraint, we have extended the domain of application of the TTO. However, we must be careful because very high volumes of fraction solutions can lead to too many bar intersections, resulting in structures with no physical meaning.

Table 2.3: Numerical comparison of the effect of the minimum slenderness constraint on the optimization of the 2D L-shaped beam.

σ_L	V_f	Min λ	$V_{f,sl}$	Min λ_{sl}	$V_{f,sl}/V_f$	$N_{el,sl}/N_{el}$	t_{sl}/t
1.0	6.21 %	15.8	6.21 %	15.8	1.0000	1.00	1.02
0.9	6.90 %	15.0	6.90 %	15.0	1.0000	1.00	1.03
0.8	7.76 %	14.1	7.76 %	15.0	1.0001	1.12	2.27
0.7	8.87 %	13.2	8.87 %	15.0	1.0001	1.12	2.21
0.6	10.35 %	12.2	10.35 %	15.0	1.0002	1.12	1.12
0.5	12.42 %	11.2	12.42 %	15.0	1.0003	1.12	1.07
0.4	–	–	15.53 %	15.0	–	–	–
0.3	–	–	20.71 %	15.0	–	–	–
0.2	–	–	31.06 %	15.0	–	–	–

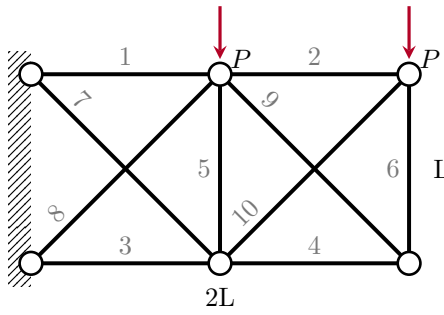


Figure 2.8: The ten-bar truss ground structure and load case.

2.3.2 TEN-BAR TRUSS

The ten-bar truss is a test case subjected to maximum stress and local buckling constraints proposed by [69] and is shown in Fig. 2.8. It is a small test case with 32 design variables (10 cross-sectional area, 10 internal force, and 12 displacement variables) and 42 constraints (12 force equilibrium, 20 maximum stress, 10 local buckling, and 10 kinematic compatibility constraints) when solved using Formulation \mathbb{P}_1 . The geometry and material data are given in Table 2.4. For simplicity, all numeric values are assumed normalized and dimensionless. We compare the results obtained by our method with those obtained by direct NLP resolution and with the results published by [69] and [70].

The robustness of the optimization algorithms to local minima is evaluated by running 50 optimizations from different initialization points a^0 randomly chosen in the interval $[0, 100]$. The first initialization point, denoted a_s^0 , is specifically chosen to match the one used by [70] ($a_{s,2}^0 = a_{s,8}^0 = a_{s,10}^0 = 0$ and $a_{s,i}^0 = 50$ elsewhere). This is the starting point from which the authors conclude that the problem is initialization-dependent.

In Fig. 2.9 we show the scatter plot of the optimization of the ten-bar truss for the four considered resolution algorithms, where for every initialization point (X-axis) we show the final volume of the structure. The NLP algorithm converges to different solutions with varying volume values, confirming an abundance of local minima

Parameter	Value
L	360
E	1.0×10^4
s	$\pi E/4$
σ_c, σ_t	± 20
P	100

Table 2.4: Material data used for the ten-bar truss optimization.

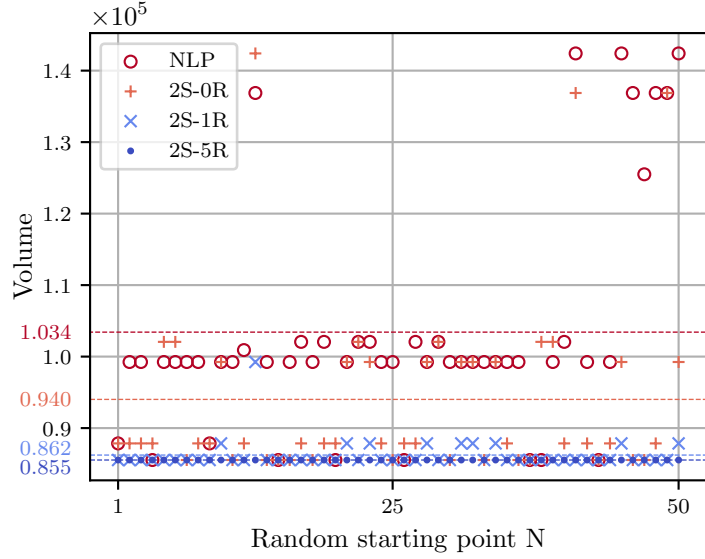


Figure 2.9: Scatter plot of the four benchmarked optimization algorithms on the ten-bar truss. The 2S-5R shows a 100 % convergence rate to the lightest structure found. The dashed lines represent the mean of the distributions.

Table 2.5: Numerical comparison of the four optimization algorithms on the ten-bar truss for 50 different initial points. The 2S-5R algorithm shows a 100 % convergence rate to the lightest structure found. The iteration count and time are from the first initialization point a_s^0 .

Algorithm	$\bar{V} \pm SD$	Conv.	It.	t [s]
NLP	$(1.03 \pm 0.15) \times 10^5$	14 %	22	0.25
2S-0R	$(9.40 \pm 1.22) \times 10^4$	20 %	4	0.06
2S-1R	$(8.62 \pm 0.21) \times 10^4$	80 %	17	0.24
2S-5R	$(8.55 \pm 0.00) \times 10^4$	100 %	73	1.18
[69]	8.78×10^4	-	-	-
[70]	8.55×10^4	-	-	-

even for such a small test case with 10 bars. The optimized results are dispersed, and the best design found ($V = 85534$) is only attained 7 times over the 50 optimization runs (14 %). To properly compare the different algorithms, we use two different figures of merit: the mean \bar{V} and the standard deviation SD of the distribution of the volume of the optimized designs and the ratio of solutions converged to the best result to the total number of initialization points. The numerical results are listed in Table 2.5. The proposed two-step optimization strategy (2S-0R) already reduces \bar{V} by approximately 9 % compared to NLP, but it is only when we introduce the reinitialization strategy that major improvements are observed, especially when multiple calls of the heuristic are done. The five-calls reinitialization optimization strategy (2S-5R) is not influenced by the initialization point ($SD = 0$), with all solutions successfully converging to the lightest structure.

Let us consider only the first initialization point a_s^0 . In Fig. 2.10 we show the convergence history and the design of the structure throughout the iterations for that specific case. We notice how the initialization point a_s^0 (represented in Fig. 2.10a) corresponds to the topology of the local minimum found by [69]. As extensively shown in Section 2.2.3, if the cross-sectional area of one member is almost or exactly zero the gradient of the local buckling constraint tends to zero and the bar is not considered in the optimization anymore. For

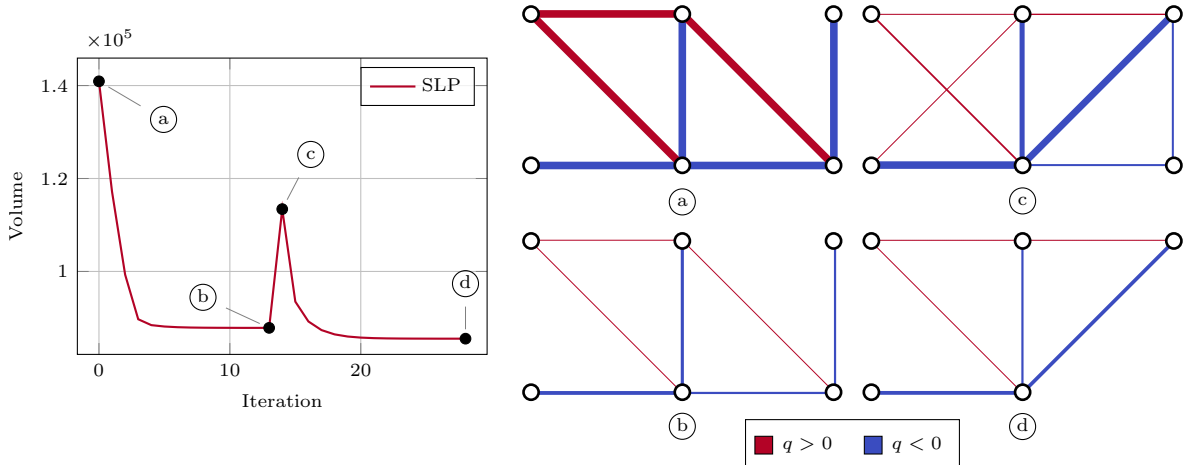


Figure 2.10: Volume convergence history for the proposed two-step resolution strategy with one step of reinitialization (2S-1R) for the initialization point a_s^0 . The reinitialization strategy permits to jump from the local minimum (b), with $V = 87857$, to the lighter structure (d), with $V = 85534$. Only the SLP step is plotted because the solution is statically determinate and kinematic compatibility constraints are already satisfied. In red the members loaded in tension, in blue the members loaded in compression.

that reason, the optimizer is not able to restore the bars initialized at 0 and promptly converges to a solution that presents the very same topology (see Fig. 2.10b, $V = 87857$). This structure would be the optimization result if no additional steps are done. With a single call of the reinitialization heuristic, the topology is modified as shown in Fig. 2.10c, in which bars 2 and 10 are reintroduced in the set of active members. From this iteration, the optimizer finally converges to the lighter structure shown in Fig. 2.10d with $V = 85534$, showing the interest of the reinitialization strategy. We notice how only the SLP step of the proposed two-step strategy is shown here as the optimized structure is statically determinate ($DSI=0$ and stiffness matrix \mathbf{K} non-singular) and the kinematic compatibility is already satisfied by the optimized design.

It should be mentioned that the proposed heuristic comes with an increase in computational cost. While for the first initialization point, the 2S-0R algorithm converges in only 4 iterations, the single-step 2S-1R and the five-step 2S-5R algorithms converge after 17 and 73 iterations, respectively. The optimization time is slightly more than one second (see the last column of Table 2.5). However, this increase in calculation time is justified by the fact that a single initialization point should suffice to reach an acceptable solution, instead of using a multistart approach.

It is advisable to select the highest number of reinitialization calls (parameter n_{\max} of Equation 2.10) that is compatible with the user's computational budget. Our research findings suggest that once the parameter ϕ_k (which determines the strength of the heuristic perturbation) drops below 0.01, the reinitialization has no more influence on the result of the linearized problem. Therefore, with the proposed

parameterization of the continuation scheme, pursuing more than five reinitialization calls does not yield additional benefits in the studied test cases.

2.3.3 2D CANTILEVER BEAM

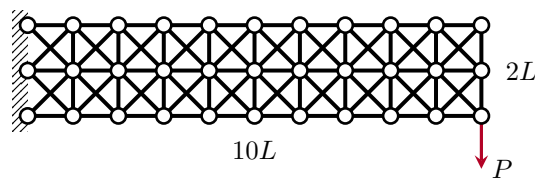
The second example we consider is a 2D cantilever beam charged on one extremity as shown in Fig. 2.11. This test case was proposed by Achtziger [61] with the geometry and dimensionless material data given in Table 2.6. The number of the candidate bars of the initial ground structure is $N_{\text{el}} = 90$. The complexity of this problem resides in the fact that the geometry and material data are chosen in such a way that the solution with or without local buckling constraints coincides if topological buckling is not considered. The optimized structure shows in this case a volume of $V = 70.00$. However, as this structure presents multiple bars in compressive chains, we need to merge them into single bars, recalculate their length, and evaluate their sections to comply with local buckling constraints. By doing so, we would obtain $V = 99.99$, an increase of more than 40 % with respect to the optimized structure just found. This load case is built to show the importance of topological buckling and suggests that a lighter solution is to be found between these two bounds.

The 2D cantilever is optimized starting from 100 random points $\mathbf{a}^0 \in [0, 100]$ and the same four algorithms presented in the previous section. At the end of the optimization, the resulting structures are checked for compressive chains and, if present, they are merged into single bars. The final volume does not change as the effective buckling length ℓ^* is iteratively updated using Equation 2.6 during the optimization. The numerical results are presented in Table 2.7.

Table 2.6: Material data used for the 2D cantilever beam optimization.

[61] Achtziger (1999), ‘Local stability of trusses in the context of topology optimization Part II’

Figure 2.11: The 2D cantilever beam load case with a first-order connectivity ground structure. The total number of candidate members is $N_{\text{el}} = 90$.



Algorithm	V_{\min}	$\bar{V} \pm SD$	N_{\min}	$\bar{N}_{\text{el}} \pm SD$
NLP	80.67	81.34 ± 2.98	58	66.57 ± 1.13
2S-0R	79.88	92.80 ± 7.45	10	25.61 ± 7.94
2S-1R	77.78	88.42 ± 6.29	10	27.86 ± 6.56
2S-5R	77.78	86.72 ± 6.05	10	28.60 ± 6.44
[61]	85.58	-	18	-

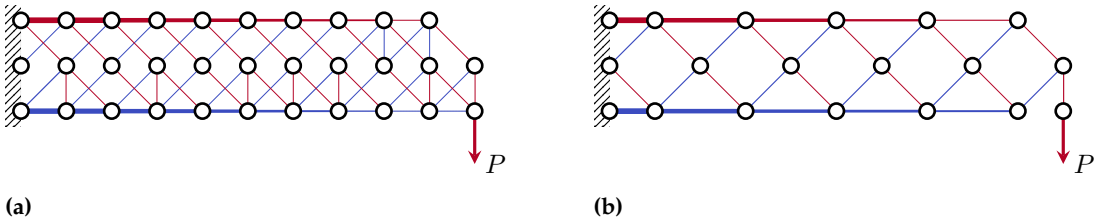


Figure 2.12: (a) NLP optimized design of the 2D cantilever beam with a volume of $V = 80.67$ and high number of active and crossing bars $N_{\text{el}} = 66$; (b) 2S-5R solution $V = 77.78$ with $N_{\text{el}} = 31$. In red the members loaded in tension, in blue the members loaded in compression.

The NLP algorithm shows a good consistency with a mean volume $\bar{V} = 81.34$ and a low dispersion of the results ($SD = 2.98$), repeatedly converging to a specific solution with $V = 80.85$. However, despite the apparent good numerical performance, the solutions always present a high number of active bars, with an average \bar{N}_{el} of over 66 bars. As discussed in Section 2.2, the NLP algorithm encounters difficulties in driving the cross-sectional areas to 0. Fig. 2.12a shows the lightest design found using NLP, with $V = 80.67$ and $N_{\text{el}} = 66$.

The proposed two-step formulation without reinitialization 2S-0R drastically reduces the complexity of the structure, with an average number of active bars \bar{N}_{el} of around 27, and an absolute minimum of $N_{\min} = 10$. However, this simplification of the design comes at the expense of an increased average volume and dispersion ($\bar{V} = 92.80$ and $SD = 7.45$). This detrimental effect is efficiently counterbalanced with the proposed reinitialization strategy, which reduces the average volume to $\bar{V} = 86.72$ and $SD = 6.05$ for 2S-5R. To sum up, the NLP remains stuck in a low-volume local optimum whose volume varies little and that shows a very high number of active bars. With the two-stage strategy, the number of bars of the optimized structures is 58 % lower, resulting in a lighter design in 30 % of cases, and with the best design found that is 3.5 % lighter.

Fig. 2.13 shows how the results of the proposed algorithm are more scattered and do not converge to a single minimum as precedently seen on the ten-bar truss example of Section 2.3.2. A possible explanation for this difference in performance might be the discrete nature of the optimization when topological buckling constraints are taken into account. In some rare cases, we observed that calling the reinitialization makes the optimization converge to a more voluminous design compared to the one we had just before. In these cases, the

Table 2.7: Numerical comparison of the 2D cantilever beam of the four algorithms for 100 random initial points. The 2S-5R algorithm shows a good balance between the volume, complexity, and dispersion of the solutions.

$(x_a \ y_a)$	$(x_b \ y_b)$	ℓ	q	a	V
(0 0)	(1 0)	1.00–5.00	5.00	5.00	
(1 0)	(0 1)	1.41	0.71	0.71	1.00
(1 0)	(2 1)	1.41–0.71	1.02	1.45	
(3 0)	(2 1)	1.41	0.71	0.71	1.00
(3 0)	(4 1)	1.41–0.71	1.02	1.45	
(5 0)	(4 1)	1.41	0.71	0.71	1.00
(5 0)	(6 1)	1.41–0.71	1.02	1.45	
(7 0)	(6 1)	1.41	0.71	0.71	1.00
(7 0)	(8 1)	1.41–0.71	1.02	1.45	
(9 0)	(8 1)	1.41	0.71	0.71	1.00
(9 0)	(10 1)	1.41–0.71	1.02	1.45	
(10 0)	(10 1)	1.00	1.00	1.00	1.00
(0 1)	(1 2)	1.41–0.71	1.02	1.45	
(2 1)	(1 2)	1.41	0.71	0.71	1.00
(2 1)	(3 2)	1.41–0.71	1.02	1.45	
(4 1)	(3 2)	1.41	0.71	0.71	1.00
(4 1)	(5 2)	1.41–0.71	1.02	1.45	
(6 1)	(5 2)	1.41	0.71	0.71	1.00
(6 1)	(7 2)	1.41–0.71	1.02	1.45	
(8 1)	(7 2)	1.41	0.71	0.71	1.00
(8 1)	(9 2)	1.41–0.71	1.02	1.45	
(10 1)	(9 2)	1.41	0.71	0.71	1.00
(0 2)	(1 2)	1.00	5.00	5.00	5.00
(1 0)	(3 0)	2.00–4.00	4.00	8.00	
(3 0)	(5 0)	2.00–3.00	3.00	6.00	
(5 0)	(7 0)	2.00–2.00	2.43	4.87	
(7 0)	(9 0)	2.00–1.00	1.72	3.44	
(1 2)	(3 2)	2.00	4.00	4.00	8.00
(3 2)	(5 2)	2.00	3.00	3.00	6.00
(5 2)	(7 2)	2.00	2.00	2.00	4.00
(7 2)	(9 2)	2.00	1.00	1.00	2.00
					$V_{\text{tot}} \ 77.78^a$

^aThe total volume value is lower than the sum of the member volumes due to the 2 decimal places round-off.

Table 2.8: Optimal values of the member forces, areas, and volumes of the 2D cantilever beam.

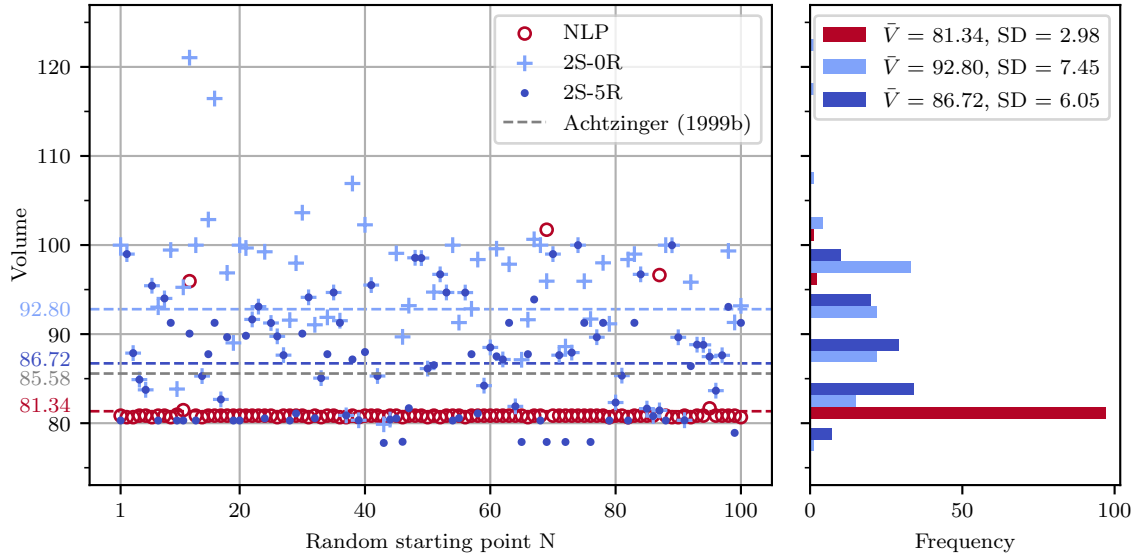


Figure 2.13: Left: scatter plot of three of the four benchmarked optimization algorithms on the 2D cantilever beam compared to the solution by Achtziger [61]. The dashed lines represent the mean of distributions. Right: histogram of the distribution of the results of the optimization algorithms.

results presented are the best ones encountered over the optimization steps and not the final ones.

The lightest solution found by 2S-5R with a volume of $V = 77.78$ and with $N_{el} = 31$ is presented in Fig. 2.12b. Some of the active members of the optimized design are not present in the original ground structure but are the result of the bar merging process. The optimized design shows a 9 % lower volume with respect to the solution found by Achtziger [61] with $V = 85.57^1$. The detailed value of the design variables of the solution can be found in Table 2.8 and in the referenced data set [85]. Approximately 45 % of the solutions of the 2S-5R algorithm are less voluminous than the one found by Achtziger.

61. Achtziger (1999), 'Local stability of trusses in the context of topology optimization Part II'

1: Even if Achtziger [61] reports an optimized volume of $V = 79.57$, we use here the value corrected by Tyas [64] of $V = 85.57$.

85. Stragiotti (2023), 'Truss Topology Optimization with Topological Buckling Constraints Data Set'

The authors are aware of the less voluminous solution ($V = 73.44$) found by [64]. The main reason for the difference is that Tyas's method allows the inclusion of bracing-only members that are not required for primary load-carrying purposes to reduce the effective buckling lengths ℓ of internal members. The incorporation of these members is regulated by introducing perturbative forces applied to the structure as additional load cases at unstable nodes. In the specific example of Tyas' structure, the resulting structure is statically admissible, and this ensures that kinematic compatibility is satisfied. However, as demonstrated later in this Chapter, this may not always be the case. Tyas' formulation, in this context, serves only as a lower-bound formulation for minimizing the structure's volume.

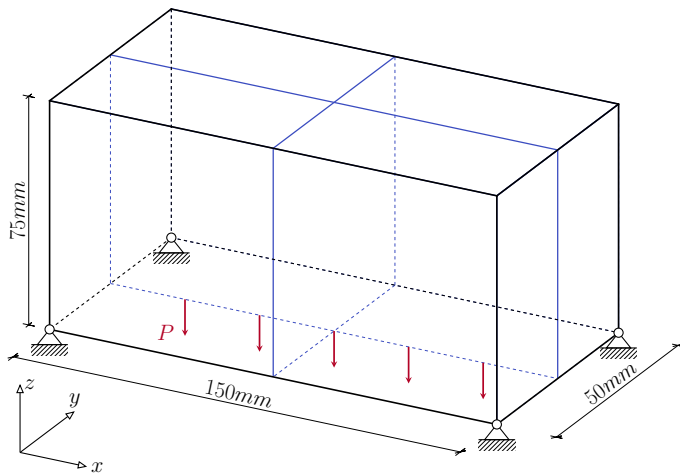


Figure 2.14: The simply supported 3D beam example with the load case and boundary conditions. In blue we plot the symmetry planes.

2.3.4 SIMPLY SUPPORTED 3D BEAM

In this subsection, we focus on optimizing a simply supported three-dimensional beam. The supports are positioned at all four lower extremities of the design volume, the structure is subjected to five equispaced nodal loads, with each load magnitude set to $P = 100 \text{ N}$, applied on the XZ symmetry plane of the structure, as depicted in Fig. 2.14. The volume of the design space is $150 \text{ mm} \times 50 \text{ mm} \times 75 \text{ mm}$. These specific dimensions have been selected to accommodate the printing volume of the Creality Halot One, which is an Stereolithography (SLA) 3D printer with maximal printing dimensions of $127 \text{ mm} \times 80 \text{ mm} \times 160 \text{ mm}$. The material properties used for the optimization are given in Table 2.9 and mimic a tough SLA resin². The test case exhibits symmetry concerning the XZ and YZ planes (see blue lines of Fig. 2.14), enabling us to mesh and optimize just one-quarter of the structure. This specific portion is meshed using a fully connected ground structure with dimensions of $4 \times 2 \times 4$ nodes, resulting in a total of 496 elements (or 1984 for the entire structure). For this case, we employ the 2S-5R solving algorithm.

2: The material data has been sourced from 3ds.com/make/solutions/blog/sla-3d-printing-materials-compared and hubs.com/knowledge-base/sla-3d-printing-materials-compared.

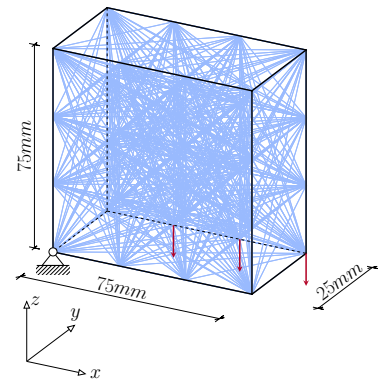


Figure 2.15: Ground structure composed of $N_{\text{el}} = 496$ elements of the symmetric portion used to optimize the simply supported 3D beam.

Table 2.10 and Fig. 2.16 show the numerical results and topology of the optimized structure, respectively. The entire structure features 20 active bars, approximately 1 percent of the original ground structure. In Fig. 2.17, we visualize the stress and buckling constraints applied to the optimized structure. Every compression-loaded bar of the optimized structure activates the buckling constraint, underscoring the critical importance of accounting for this mode of structural failure in a truss. The final structure has a weight of 11.294 g and achieves a volume fraction of 1.761% . The optimization process is completed within 4 seconds, with only the SLP solved, as the resultant structure is statically determinate and kinematic constraints are inherently satisfied.

Parameter	Value
E	2.7 GPa
ν	0.3
σ_c, σ_t	$\pm 55 \text{ MPa}$
ρ	1.14 g cm^{-3}
P	100 N

Table 2.9: Material data used for the simply supported 3D beam optimization.

Table 2.10: Numerical results of the optimization of the simply supported 3D beam.

Quantity	Value
N_{el}	1984
N_{opt}	20
V	9.907 cm^3
$V\%$	1.761 %
Mass	11.294 g
a_{max}	37.61 mm^2
C	3.71 J
t	4 s

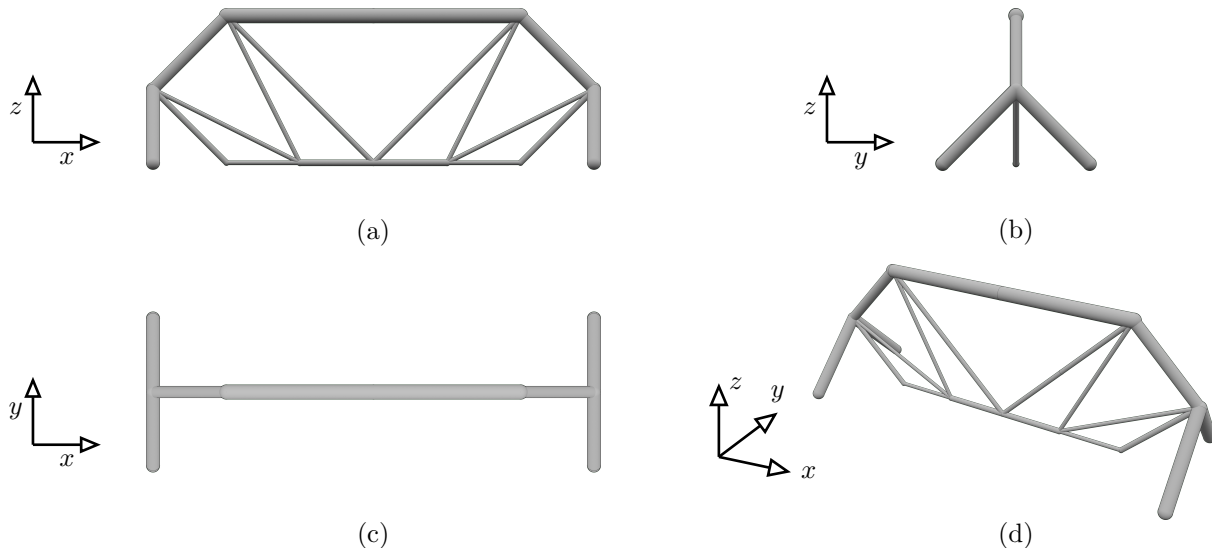


Figure 2.16: Orthographic views of the topology of the optimized simply supported 3D beam. (a) XZ plane (b) YZ plane (c) XY plane (d) auxiliary perspective view.

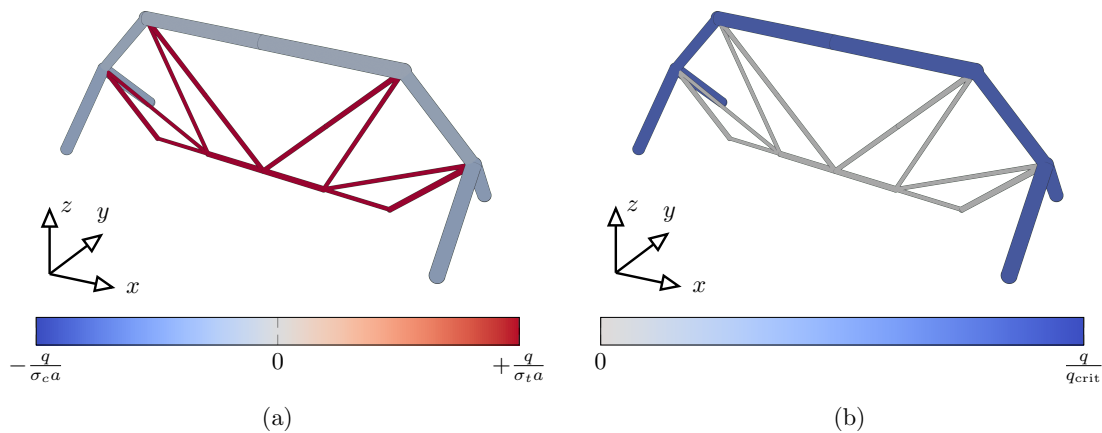


Figure 2.17: Maximum stress constraint value (a) and buckling constraint value (b) plotted on the optimized topology of the simply supported 3D beam.

Algorithm	$\bar{V} \pm \text{SD}$
NLP	$1.45 \times 10^5 \pm 1.44 \times 10^4$
2S-0R	$1.33 \times 10^5 \pm 9.56 \times 10^3$
2S-1R	$1.35 \times 10^5 \pm 2.73 \times 10^3$
2S-5R	$1.35 \times 10^5 \pm 2.73 \times 10^3$

Table 2.11: Numerical comparison of the four optimization algorithms on the ten-bar truss for 50 different initial points.

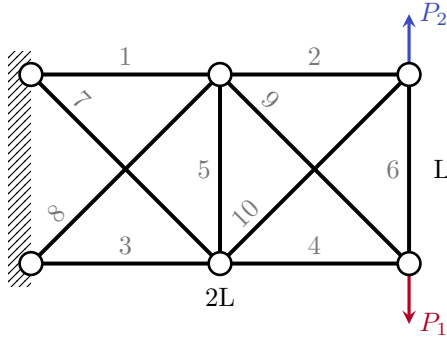


Figure 2.18: Ground structure of the ten-bar truss with two applied load cases P_1 and P_2 .

2.3.5 TEN-BAR TRUSS WITH MULTIPLE LOAD CASES

We introduce here a more complex example to validate the proposed algorithm on a multiple load cases structure with maximum stress and topological buckling constraints. The test case is obtained by slightly modifying the ten-bar truss presented in Section 2.3.2. The ground structure and the material data are the same, and two load cases P_1 and P_2 are applied at the structure's free extremity in a symmetric way with respect to the horizontal axis. A graphical presentation of the load case is shown in Fig. 2.18. The loads' magnitude is set to $P_1 = P_2 = 1$.

First, we optimize the structure using the same four algorithms and the starting point presented in Section 2.3.2. Differently from the structures optimized earlier in Sections 2.3.2 and 2.3.3, the solutions of the SLP step are statically indeterminate, as they show a $\text{DSI} > 0$ and a non-singular \mathbf{K} stiffness matrix. For that reason, the structures undergo a second optimization in which the kinematic compatibility and the exact buckling constraints are restored (NLP step, see Formulation \mathbb{P}_1). The numerical findings of the four algorithms are presented in Table 2.11.

In agreement with previous results, the proposed 2S-5R strategy reduces simultaneously the volume and the dispersion of the solutions. Interestingly, the mean value \bar{V} of the 2S-0R algorithm is 1.3 % lower with respect to 2S-5R, a fact never observed before. This is due to the 2S-0R algorithm occasionally converging to a heavier solution in the SLP phase that results in a lighter solution once optimized by the NLP, suggesting that the lightest SLP configuration does not always correspond to the lightest NLP design. However, as the difference between the two solutions is low (3.9 %), the 2S-5R algorithm is still preferred thanks to its higher solution consistency (the dispersion σ

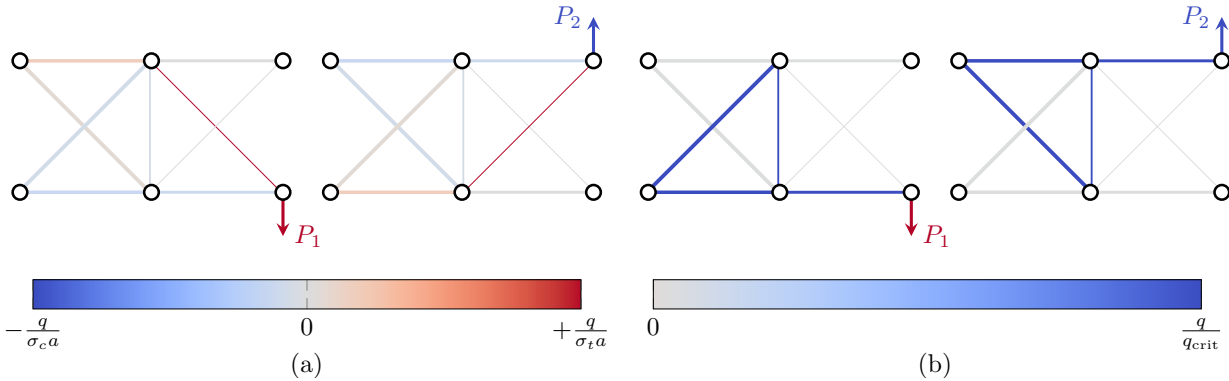


Figure 2.19: Maximum stress constraint value (left) and buckling constraint value (right) plotted on the optimized design of the multiple load cases ten-bar truss.

86. Rozvany (2011), 'On symmetry and non-uniqueness in exact topology optimization'

87. Guo et al. (2014), 'A confirmation of a conjecture on the existence of symmetric optimal solution under multiple loads'

of 2S-5R is 71 % lower than the dispersion σ of 2S-0R).

We now analyze the lightest solution with a final volume of $V = 134279.32$. The optimized design obtained is symmetric. This is consistent with Conjecture 4 made by Rozvany [86], according to which if the boundary conditions and the ground structure are symmetric, and two alternate load conditions are mirror images of each other with respect to the symmetry axis, then at least one globally optimal topology is symmetric. This conjecture has been confirmed in [87] in the case of symmetric convex optimization problems. It is interesting to note that the Conjecture still holds for this specific example even if problem \mathbb{P}_1 is non-linear and non-convex. In Table 2.12 we list the cross-sectional area of the members for the two steps of the proposed solving optimization strategy. The NLP optimized structure presents a volume $V = 134279.32$, a 35.15 % increase compared to the predicted volume of the SLP step of $V = 99084.93$. Incorporating kinematic constraints to achieve a solution that adheres to elasticity requirements significantly impacts the volume of the optimized solution. The design for the two different load cases P_1 and P_2 is shown in Fig. 2.19, where a side-by-side plot of the maximum stress and buckling constraints is presented. In this example, the bars are constrained by either the buckling or the stress of one of the two load cases. The detailed value of the design variables of the solution is given in Table 2.13, while the iteration history curves of the optimization can be found in Fig. 2.20.

In Fig. 2.20 we provide the iteration history of the objective function and the constraint violation for the SLP and the NLP steps. The graphs on the left depict the evolution of volume during optimization in both the SLP and NLP steps. Looking at the SLP step (red plot), we can see that the SLP reduces the volume and exhibits occasional "spikes," which correspond to the reinitialization heuristic calls. The gradual diminishment of these spikes throughout the optimization is due to the incorporation of the continuation scheme on the parameter ϕ_k of Equation 2.10. Turning our attention to the NLP step, we observe that initially the volume is increased and then it descends again, stabilizing

Bar	SLP step \mathbb{P}_2	NLP step \mathbb{P}_1	Difference
a_1	57.296	47.987	-16.24 %
a_2	40.408	40.621	+0.05 %
a_3	57.296	47.987	-16.24 %
a_4	40.408	40.621	+0.05 %
a_5	40.193	25.547	-36.43 %
a_6	0.052	0.000	—
a_7	6.997	53.115	+659.11 %
a_8	6.997	53.115	+659.11 %
a_9	6.997	7.071	+0.01 %
a_{10}	6.997	7.071	+0.01 %
V	99084.93	134279.32	+35.51 %

$(x_a \ y_a)$	$(x_b \ y_b)$	ℓ	q_1	q_2	\mathbf{a}	\mathbf{V}
(0 360)	(360 360)	360.0	160.5	-139.6	48.0	17 275.4
(360 360)	(720 360)	360.0	0.0	-100.0	40.6	14 623.8
(0 0)	(360 0)	360.0	-139.6	160.5	48.0	17 275.4
(360 0)	(720 0)	360.0	-100.0	0.0	40.6	14 623.8
(360 0)	(360 360)	360.0	-39.6	-39.6	25.6	9197.0
(360 0)	(0 360)	509.1	55.9	-85.5	53.1	27 042.0
(0 0)	(360 360)	509.1	-85.5	55.9	53.1	27 042.0
(720 0)	(360 360)	509.1	141.4	0.0	7.1	3600.0
(360 0)	(720 360)	509.1	0.0	141.4	7.1	3600.0
V_{tot}						134279.32 ^a

^aThe total volume value is lower than the sum of the member volumes due to the one decimal places round-off.

at a value that is higher than the one of the NLP starting point. To elucidate this behavior, we refer to the graphs on the right, which present the history of constraint violations in the NLP step. Notably, the starting point of the NLP step always respects equilibrium g_{eq} and kinematic compatibility g_{comp} , as displacements and forces are evaluated using Equation 2.13. However, stress $g_{\text{st,c}}$ and $g_{\text{st,t}}$ and buckling constraints g_{buck} are not initially respected, because the force field provided by the SLP does not account for the kinematic compatibility constraint. The NLP optimizer then tries to reduce violations of buckling and stress while temporarily increasing its volume (a phase referred to as the "restoration phase" in the IPOPT algorithm). Ultimately, the optimizer converges to a volume that is slightly higher than what was predicted by the SLP. This aligns with the concept that, by disregarding kinematic compatibility in the SLP step, we have a lower-bound formulation for the volume.

Table 2.12: Comparison of the results of the SLP step and NLP step for the multiple load cases ten-bar truss.

Table 2.13: Optimal values of the member forces, areas, and volumes of the members of the ten-bar truss with multiple load cases.

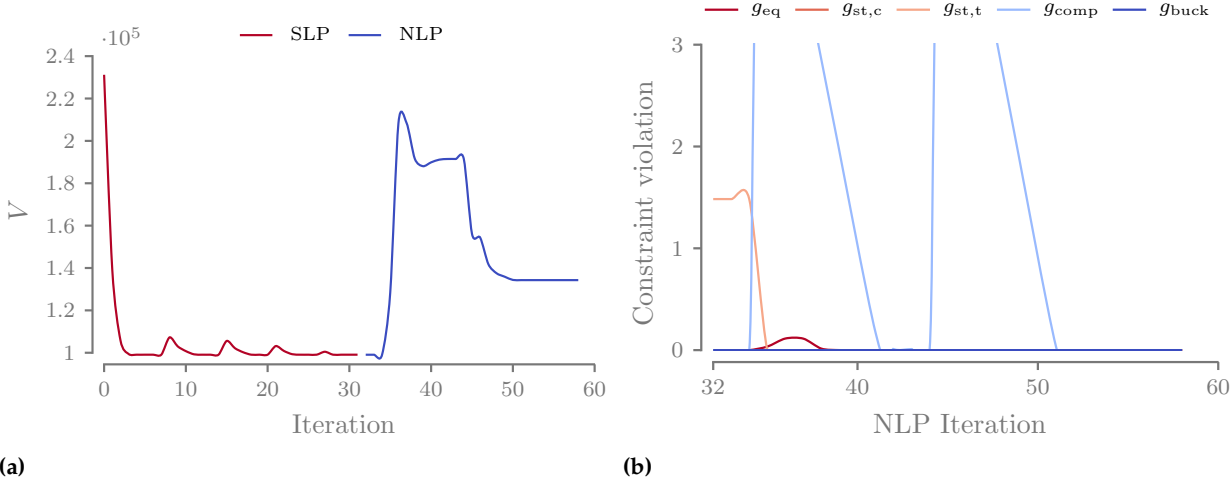


Figure 2.20: Iteration history of the ten-bar truss with multiple load cases example solved with the 2S-5R algorithm; (a) objective function history for the SLP and NLP step (b) constraint violation for the NLP step.

2.4 CONCLUSION

In this chapter, we presented a structural optimization formulation that minimizes the mass of two- and three-dimensional truss structures subject to multiple load cases, maximum stress, topological buckling, and minimum slenderness constraints. The optimization is solved using an efficient two-step method and shows a reduced influence on the starting point thanks to the proposed reinitialization heuristic. Several numeric examples are presented using the proposed optimization algorithm. Optimized structures display designs with fewer active members compared to traditional optimization methods, leading to lower overall manufacturing complexity. Additionally, thanks to the computational efficiency of the proposed optimization strategy, we show how advanced mechanical constraints such as maximum stress, topological buckling, and kinematic compatibility constraints can be applied and solved on structures with thousands of candidates on a notebook computer.

However, some research questions still remain open. The manufacturing complexity is discussed here only as an outcome of the optimization strategy, but a direct way to impose manufacturing constraints (maximum numbers of bars converging to a single node, minimum section, imposed periodicity of the structure) during the optimization would be beneficial. For that reason, in the next chapters, we study the mechanical behavior of modular structures, exploring the trade-off between mechanical performance and manufacturing complexity.

OPTIMIZING MODULAR STRUCTURES

Introduction TODO

In Section 3.1, we provide a detailed explanation of the modifications needed to apply modular constraints to the Truss Topology Optimization (TTO). Specifically, we focus on how to model the problem when multiple modules are used and how topological buckling constraints are implemented in modular structures. Finally, in Section 3.2, we evaluate the proposed formulation through various 2D and 3D test cases, aiming to gain a better understanding of modular structures.

3.1 FORMULATION OF A MODULAR STRUCTURE OPTIMIZATION ALGORITHM

Assembled modular ultralight structures present an opportunity to greatly improve the performance and cost efficiency of modern aerostructures [89]. The repetitive nature brings various interesting features among which reduced tooling, fast assembly, and short repair time. Additionally, as the mechanical performance of the structure is greatly influenced by the topology and the materials of the repetitive pattern, modular structures are naturally prone to optimization.

In the field of structure optimization, periodic materials are often modeled through asymptotic homogenization [90]. The heterogeneous module topology (also called Representative Volume Element (RVE)) is treated as homogeneous material with associated mechanical properties i.e. equivalent elastic tensor, shear modulus, etc. The homogenization approach is valid only if the RVE contains enough information about the heterogeneous material and if the structure presents significant periodicity [91, 92].

Nevertheless, our work pertains to structures that frequently exhibit one or more dimensions significantly smaller than the remaining dimensions, such as the thickness of a wingbox or a sandwich panel. In the context of designing modular structures (and not materials), no scale separation is assumed between the repetitive pattern and the structure itself. Consequently, the assumptions of asymptotic homogenization are not always verified. To address this, full-scale approaches [93] have been developed.

3.1.1 VARIABLE LINKING

The variable linking approach [9] is a full-scale optimization technique that involves first dividing a structure into several subdomains, which are connected in the optimization process – i.e. subdomains that

3.1 FORMULATION OF A MODULAR STRUCTURE OPTIMIZATION ALGORITHM	51
3.2 NUMERICAL APPLICATION	56
3.3 CONCLUSION	74

Part of the content presented in this chapter has been published and showcased during a conference as: Stragiotti, E. et al. (2022) "Enhanced truss topology optimization (TTO) applied to a cellular wing box", in *ASMO-UK 12, an ISSMO Conference on Engineering Design Optimization*. Book of proceedings. Leeds, United Kingdom [88].

89. Cramer et al. (2019), 'Elastic shape morphing of ultralight structures by programmable assembly'

90. Zhou et al. (2008), 'Design of graded two-phase microstructures for tailored elasticity gradients'

91. Kalamkarov et al. (2009), 'Asymptotic Homogenization of Composite Materials and Structures'

92. Li et al. (2020), 'Anisotropic design and optimization of conformal gradient lattice structures'

93. Wu et al. (2021), 'Topology optimization of multi-scale structures'

9. Zhang et al. (2006), 'Scale-related topology optimization of cellular materials and structures'

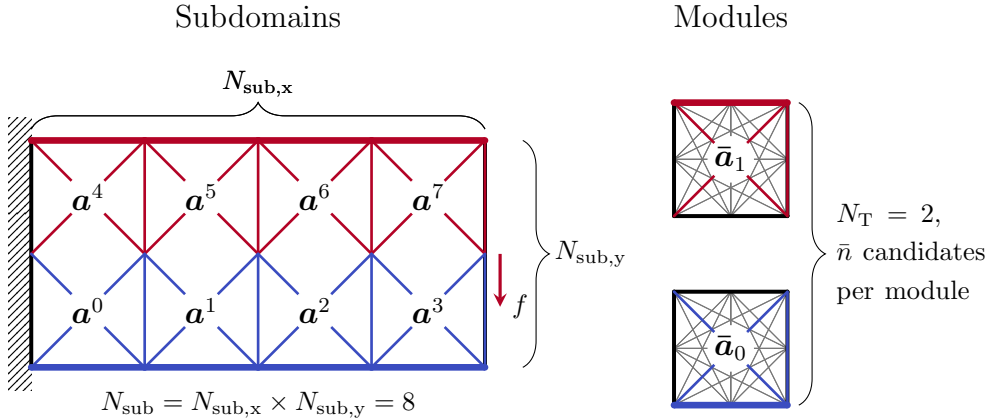


Figure 3.1: Notations used for the definition of the variable linking approach used to apply the modularity constraints.

belong to the same module all share the same cross-sectional areas. The primary goal is to make the manufacturing phase simpler and more efficient, allowing to assemble of big structures starting from smaller repetitive modules. With this approach, the optimization perspective shifts. The optimizer design space using the variable linking approach is restricted to the optimization of the topology of the modules, using the whole structure just to evaluate and impose the necessary mechanical constraints.

We use Fig. 3.1 to illustrate the notation employed in this thesis for modular structures. On the left-hand side of the image, we have the whole test case that we aim to optimize, which is divided into N_{sub} subdomains. Each of these subdomains is bound to exhibit the topology of one of the N_T module topologies presented on the right side of the image. It is assumed for simplicity that each module has the same external shape and an identical ground structure used for discretizing the module volume. Within this framework, \bar{n} represents the number of candidate bars in one module, and if we assume a fully connected mesh, we can define $\bar{n} = \bar{m} \cdot (\bar{m} - 1)/2$, where \bar{m} stands for the number of nodes in the module. Consequently, for the overall structure, we can write the relationship $N_{\text{el}} = N_{\text{sub}}\bar{n}$.

The vector that holds all the cross-sectional areas of the modules is represented by $\bar{\mathbf{a}}$, and it belongs to the set of positive real numbers $\mathbb{R}_+^{N_T \cdot \bar{n}}$. This vector is essentially a grouping of individual cross-sectional areas \bar{a}_t for each of the N_T modules. In mathematical terms, $\bar{\mathbf{a}}$ is defined as follows:

$$\bar{\mathbf{a}} := \{\bar{a}_t \in \mathbb{R}_+^{\bar{n}} \mid \forall t \in [1, \dots, N_T]\} \quad (3.1)$$

The topology of the entire structure \mathbf{a} , which originates from the submodules' topology $\bar{\mathbf{a}}$, is the assembly of the individual cross-sectional areas of every one of the N_{sub} subdomains and is defined as follows:

$$\mathbf{a} := \{\mathbf{a}^j \mid \forall j \in [1, \dots, N_{\text{sub}}]\} \quad (3.2)$$

and is evaluated using:

$$\mathbf{a} = \sum_{t=1}^{N_T} \mathbf{h}_t \otimes \bar{\mathbf{a}}_t = \sum_{t=1}^{N_T} \begin{bmatrix} h_{1,t} & \bar{\mathbf{a}}_t \\ \vdots & \\ h_{N_{\text{sub}},t} & \bar{\mathbf{a}}_t \end{bmatrix} \quad (3.3)$$

where the \otimes operator represents the Kronecker product and \mathbf{h}_t is the t -th column of the module mapping matrix $\mathbf{H} = [\mathbf{h}_0, \dots, \mathbf{h}_{N_T}] \in \mathbb{B}^{N_{\text{sub}}, N_T}$, where $\mathbb{B} = \{0, 1\}$ is the Boolean domain. $h_{j,t}$ is the element at the j -th row and t -th column of the matrix \mathbf{H} . The module mapping matrix \mathbf{H} indexes are defined as follows:

$$h_{j,t} = \begin{cases} 1 & \text{if the } j\text{-th subdomain presents the topology of the } t\text{-th module,} \\ 0 & \text{otherwise.} \end{cases} \quad (3.5)$$

Lastly, we introduce some notation to denote specific bars within the modules and subdomains. We represent the cross-sectional area of the i -th bar of the t -th module as $\bar{\mathbf{a}}_{t,i}$, while the cross-sectional area of the i -th bar of the j -th subdomain as a_i^j .

In the case of the structure shown in Fig. 3.1 we have:

$$\mathbf{H} = \begin{bmatrix} 1 & 0 & & & & & \\ 1 & 0 & & & & & \\ 1 & 0 & & & & & \\ 1 & 0 & & & & & \\ 0 & 1 & & & & & \\ 0 & 1 & & & & & \\ 0 & 1 & & & & & \\ 0 & 1 & & & & & \end{bmatrix} \quad (3.4)$$

as the lower submodules (numbered from 0 to 3) exhibit the topology of module $t = 0$, while the upper submodules (numbered 4 to 7) the topology of module $t = 1$.

3.1.2 TOPOLOGICAL BUCKLING OF MODULAR STRUCTURES

Addressing topological buckling in modular structures is a more complex task compared to monolithic structures. This complexity arises from the fact that we must not only consider bars within a single module's design space but also those connecting different modules. Since the nature of this problem heavily relies on how the modules are arranged within the structure, we have opted for a simplification. We focus only on the assessment of nodal instability within each module, modifying the length ℓ^* used to evaluate the critical buckling force of g_{buck} and Equation 2.6 only of compressive chains of bars that fall inside a module. Additionally, Equation 2.7 is modified as follows:

$$\bar{\mathbf{a}}_{t,r} \geq \bar{\mathbf{a}}_{t,r=1} \quad r \in \mathcal{C}_{l,r}(\bar{\mathbf{a}}_t) \quad \forall t \in [1, \dots, N_T]. \quad (3.6)$$

We have made this choice knowing that the high connectivity of modular structures tends to reduce the occurrence of nodal instability within the structure. Any potential nodal instability in compressive chains at the structure level is addressed in a subsequent post-processing phase.

3.1.3 OPTIMIZATION FORMULATION

The monolithic formulation \mathbb{P}_1 is updated using Equations 3.3, and 3.6 to obtain the modular optimization formulation \mathbb{M}_1 that use the variable linking approach. Formulation \mathbb{M}_1 is stated in terms of modular cross-sectional areas $\bar{\mathbf{a}}$, member forces \mathbf{q} and nodal

Equation 2.6:

$$\ell_i^*(\mathbf{a}) := \begin{cases} \ell_i & \text{if } i \notin \mathcal{C}_{l,r}(\mathbf{a}) \\ \sum \ell_r \mid r \in \mathcal{C}_{l,r}(\mathbf{a}) & \text{otherwise.} \end{cases}$$

Equation 2.7:

$$a_r \geq a_{r=1}, \quad r \in \mathcal{C}_{l,r}(\mathbf{a}), \quad \forall r \neq 1.$$

displacements \mathbf{U} as follows:

$$\begin{aligned}
 \min_{\bar{\mathbf{a}}, \mathbf{q}, \mathbf{U}} \quad & V = \ell^T \mathbf{a} \\
 \text{s.t.} \quad & \mathbf{a} = \sum_{t=1}^{N_T} \mathbf{h}_t \otimes \bar{\mathbf{a}}_t \\
 & \mathbf{B}\mathbf{q} = \mathbf{f} \\
 & \mathbf{q} = \frac{\mathbf{a}^E}{\ell} \mathbf{b}^T \mathbf{U} \\
 & \mathbf{q} \geq -\frac{s\mathbf{a}^2}{\ell^{*2}} \\
 & -\sigma_c \mathbf{a} \leq \mathbf{q} \leq \sigma_t \mathbf{a} \\
 & \bar{\mathbf{a}}_{t,r} \geq \bar{\mathbf{a}}_{t,r=1} \quad r \in \mathcal{C}_{l,r}(\bar{\mathbf{a}}_t), \forall t \\
 & 0 \leq \bar{\mathbf{a}} \leq \frac{4\pi\bar{\ell}^2}{\lambda_{\max}},
 \end{aligned} \tag{M1}$$

where $\bar{\ell}$ represents the vector of the lengths of the bars within the modules.

The total number of design variables in the formulation is expressed as $N_T \bar{n} + N_{\text{sub}} \bar{n} + 2M$ or $N_T \bar{n} + N_{\text{sub}} \bar{n} + 3M$, depending on whether the test case is two or three-dimensional. The number of constraints is, however, equal to the monolithic optimization. This fact arises due to the localized nature of stress, buckling, and compatibility constraints, which are all referenced not only to individual modules but to the entire structure.

The formulation is solved by reusing the proposed two-step optimization algorithm, incorporating the reinitialization heuristic to mitigate dependence on the optimization starting point, as detailed in Section 2.2.1. We state here the formulation \mathbb{M}_2 with relaxed compatibility constraints that are solved as the first step of the optimization.

$$\begin{aligned}
 \min_{\bar{\mathbf{a}}, \mathbf{q}, \mathbf{U}} \quad & V = \ell^T \mathbf{a} \\
 \text{s.t.} \quad & \mathbf{a} = \sum_{t=1}^{N_T} \mathbf{h}_t \otimes \bar{\mathbf{a}}_t \\
 & \mathbf{B}\mathbf{q} = \mathbf{f} \\
 & \mathbf{q} \geq -\frac{s\mathbf{a}^2}{\ell^{*2}} \\
 & -\sigma_c \mathbf{a} \leq \mathbf{q} \leq \sigma_t \mathbf{a} \\
 & \bar{\mathbf{a}}_{t,r} \geq \bar{\mathbf{a}}_{t,r=1} \quad r \in \mathcal{C}_{l,r}(\bar{\mathbf{a}}_t), \forall t \\
 & 0 \leq \bar{\mathbf{a}} \leq \frac{4\pi\bar{\ell}^2}{\lambda_{\max}}.
 \end{aligned} \tag{M2}$$

We can solve Formulation \mathbb{M}_2 by breaking it down into simpler linearized problems using a Sequential Linear Programming (SLP)

algorithm. This is possible because the Kronecker product is a linear operator, and the buckling constraints can be linearized, as previously demonstrated in Section 2.2.1.

3.1.4 SENSITIVITY ANALYSIS

During each iteration of the optimization process, the current state of the structure is determined by the values assigned to the design variables. In structure optimization, the evolution of the structure's design is guided by assessing the sensitivities of both the objective function and constraints with respect to the design variables. In the specific context of modular structure optimization, the module (and not the structure divided into the subdomains) is identified as the design domain, and for that reason necessitating the derivation of corresponding modular sensitivities.

The approach involves initially computing gradients for all candidates for the full monolithic structure, without considering the modularity. Subsequently, the contributions of each i -th bar belonging to a specific module topology t are summed together. Mathematically, this can be expressed as follows:

$$\frac{\partial(\cdot)_i}{\partial \bar{a}_{t,i}} = \sum_{j=0}^{N_{\text{sub}}} h_t^T \frac{\partial(\cdot)_i}{\partial a_i^j} \quad (3.7)$$

where (\cdot) is a generic function for which the sensitivity is calculated. This process is graphically represented in Fig. 3.2.

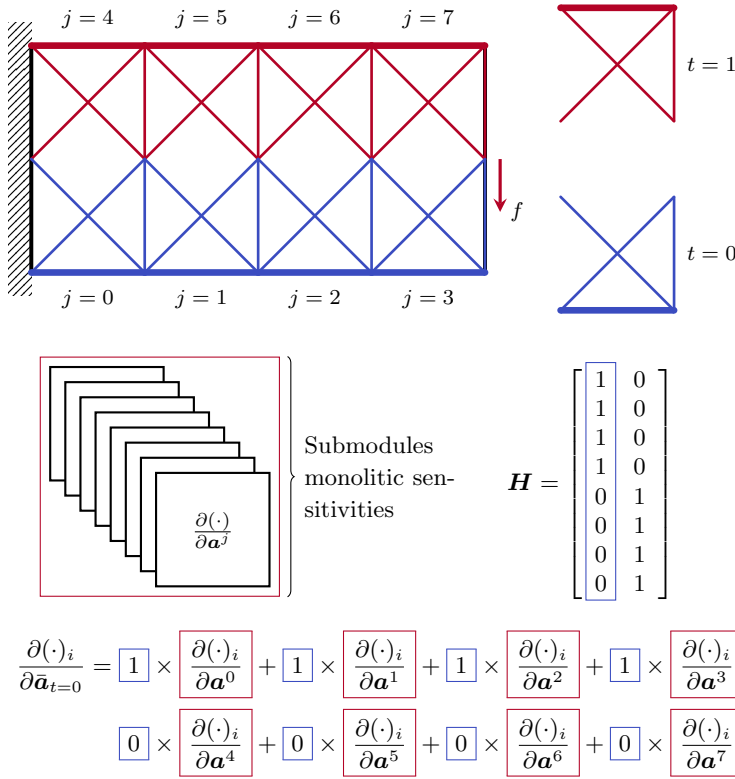


Figure 3.2: Notations used for the evaluation of the sensitivities for the modular structure optimization based on the variable linking scheme.

3.2 NUMERICAL APPLICATION

Parameter	Value
ϕ_0	0.8
β	2

Table 3.1: Reminder of the parameters used to set the reinitialization parameters for the modular optimization. The full list of values and tolerances used for the setup of the optimization algorithm can be found in Table 2.2.

48. Diamond et al. (2016), 'CVXPY: A Python-Embedded Modeling Language for Convex Optimization'

49. Domahidi et al. (2013), 'ECOS: An SOCP solver for embedded systems'

82. Moore et al. (2018), 'cyipopt: Cython interface for the interior point optimizer IPOPT'

83. Wächter et al. (2006), 'On the implementation of an interior-point filter line-search algorithm for large-scale nonlinear programming'

In this section, we formulate multiple test cases used to explore the limits and the characteristics of modular structures and the proposed modular structure optimization formulation \mathbb{M}_1 .

The test cases are optimized using the two-step resolution strategy implemented with five calls of reinitialization (2S-5R) with $n_{\max} = 5$. The reinitialization magnitude parameter ϕ is set up using the same parameters listed in Table 3.1, that leads to $\phi = [0.8000, 0.6400, 0.4096, 0.1677, 0.0281]$.

The optimizations are performed using the Python package CVXPY 1.2.2 [48] with the ECOS 2.0.7 [49] solver to solve the relaxed Linear Programming (LP) Problem \mathbb{M}_2 . The Non-Linear Programming (NLP) Problem \mathbb{M}_1 is solved using cyipopt [82], a Python wrapper for IPOPT 3.14.11 [83], a large-scale nonlinear optimization package using PARDISO 6.0 [84] as linear solver.

3.2.1 ON THE EQUIVALENCE OF MULTI-LOAD CASES AND MODULAR STRUCTURES

The first test case we deal with is a two-dimensional bridge structure segment composed of two subdomains ($n_{\text{sub}} = 2$) with symmetric boundary conditions, as illustrated in Fig. 3.3a. In this test case, two

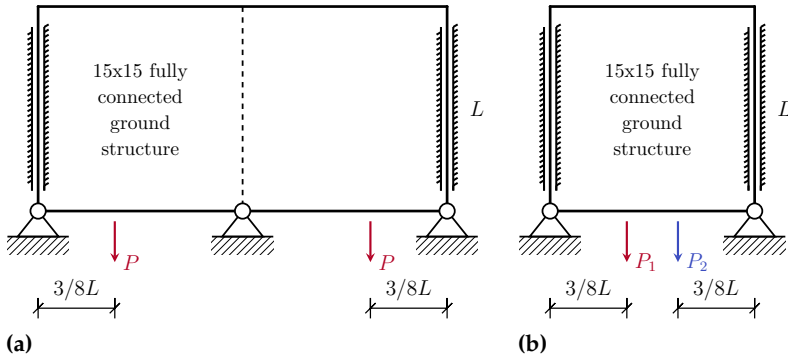


Figure 3.3: Boundary conditions of the multi-subdomains (a) and the multi-load cases (b) test cases.

Table 3.3

Quantity	Multi-subdomain	Multi-loads
N_{sub}	2	1
$N_{\text{opt}} (N_{\text{el}})$	62 (50400)	31 (25200)
V	182.692	91.346

vertical loads of magnitude $P=1$ are applied to the lower side of the design space. The material and geometrical details are given in Table 3.2 and are normalized and adimensional for simplicity. Each subdomain of the structure is discretized using a 15×15 fully connected ground structure, with a number of candidates $\bar{n} = 25200$ per subdomain. It is important to note that, for this example, buckling constraints have been deactivated.

Additionally, a similar structure is optimized, comprising only a single subdomain, subjected to two distinct load cases, denoted as P_1 and P_2 . These loads are positioned at precisely the same distance from the support as the structure with multiple subdomains, as illustrated in Fig. 3.3b. The subdomain is discretized using the same 15×15 fully connected ground structure.

The optimization is carried out for both structures, utilizing the material data specified in Table 3.2. The joint cost is set at $s = 0.05$ for the multi-subdomain structure and $s = 0.1$ for the multi-load case structure. the graphical representation of the optimized structures is given in Fig. 3.4. Remarkably, the resulting subdomain topologies are identical, with the volume of the multi-subdomain structure V_1 being precisely twice the volume of the multi-load cases structure V_2 .

This straightforward example highlights an interesting aspect of modular structure optimization that aligns with common sense. When a loaded structure is divided into multiple subdomains, each subdomain, when isolated and subjected to appropriate boundary conditions defined by the reaction forces of adjacent bars and supports, experiences multiple loading conditions. By imposing modularity constraints on all these subdomains, the optimization process seeks the optimal structure that simultaneously meets the mechanical needs of all these diverse load cases. Hence, there exists an equivalence between optimizing a multi-subdomain structure with modular constraints

84. Alappat et al. (2020), 'A Recursive Algebraic Coloring Technique for Hardware-efficient Symmetric Sparse Matrix-vector Multiplication'

Parameter	Value
L	100
E	1
σ_c, σ_t	± 1
P	1

Table 3.2: Material data used for the modular bridge section 2D structure.

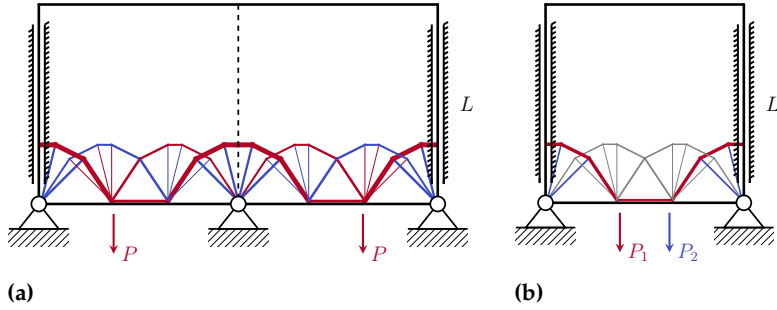


Figure 3.4: Optimized structures of the multi-subdomains (a) and the multi-load cases (b) test cases. The resulting module topology is equal for the two cases. In red the bars are in a tensile state, and in blue the bars are in a compressive state.

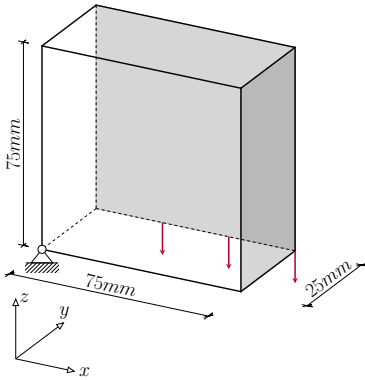


Figure 3.5: Symmetric boundary conditions of the simply supported 3D beam. In gray are the symmetry planes of the test case.

Parameter	Value
E	2.7 GPa
ν	0.3
σ_c, σ_t	± 55 MPa
ρ	1.14 g cm^{-3}
P	100 N

Table 3.4: Material data used for the simply supported 3D beam optimization.

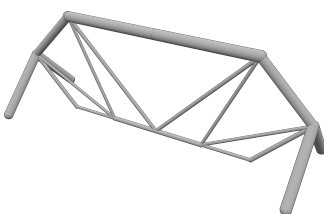


Figure 3.6: Perspective view of the monolithic simply supported 3D beam optimized structure with $V = 9.907 \text{ cm}^3$

³⁷ Michell (1904), 'The limits of economy of material in frame-structures'

and performing a multi-load case optimization solely on the module. Moreover, these examples confirm the necessity of adding kinematic compatibility constraints when addressing modularity constraints.

3.2.2 PARAMETRIC STUDY ON THE NUMBER OF SUBDOMAINS AND THE COMPLEXITY OF THE MODULE

Here, we perform a parametric study on the modular parameters that we use to optimize the simply supported 3D truss, which was previously analyzed as a monolithic structure in Section 2.3.4. In this study, we focus on a single module $N_T = 1$, excluding for the moment an examination of the impact of multiple module topologies on the optimized structure. Additionally, we restrict our investigation to a cubic cell shape. A summary of the loading case, as well as the geometric and material properties of the test case, is presented in Table 3.4 and depicted in Fig. 3.5.

We introduce two new metrics used to enhance our understanding of how modular structures are subjected to loading. The first metric, named the structural efficiency index and denoted as φ , enables a rapid assessment of how close the structure is to the optimal fully stressed state as described by Michell [37]. Since we are accounting for not only tensile and compressive stress but also local buckling, we define a bar as fully stressed when it activates one or more of the three mechanical failure constraints. It is defined by the equation:

$$\varphi = \frac{N_{\text{opt},f} \times 100}{N_{\text{opt}}}. \quad (3.8)$$

Here, $N_{\text{opt},f}$ represents the number of bars that activate either the tensile stress, compressive stress, or buckling constraints and is expressed as:

$$N_{\text{opt},f} = \text{card}(\{i \mid c_{f,i} > 0.95\}), \quad (3.9)$$

where $c_f = \max(-q/\sigma_c a, q/\sigma_t a, q/q_{\text{crit}})$ represent the normalized mechanical failure criterion and $\text{card}(\{\cdot\})$ represent the cardinality of the set $\{\cdot\}$.

The second metric, denoted as ψ , is defined as the mean value of the normalized mechanical failure criterion c_f , weighted by the volumes

of individual bars v :

$$\psi = \frac{1}{V} \left(\sum_{i=0}^{N_{\text{opt}}} v_i c_{f,i} \right) \quad (3.10)$$

This parameter ranges between 0 and 1, with higher values indicating that, on average, bars are closer to the upper limit of one of the mechanical failure constraints. Notably, greater importance is attributed to more voluminous bars.

INFLUENCE OF THE NUMBER OF THE SUBDOMAINS We begin by examining the impact of the number (and consequently, the scale, interchangeably used here) of subdomains N_{sub} in the structure. The structure is partitioned into varying numbers of cubic and equal-sized subdomains while keeping the test case and material constant. Specifically, the entire structure is subdivided into $6 \times 2 \times 3$, $12 \times 4 \times 6$, $18 \times 6 \times 9$, and $30 \times 10 \times 15$ submodules along the X , Y , and Z axes, and each subdomain is discretized by a $2 \times 2 \times 2$ fully connected ground structure with $n_{\text{bar}} = 28$. The same analysis is also conducted on a $3 \times 3 \times 3$ fully connected ground structure with $n_{\text{bar}} = 351$ to ensure that trends remain consistent across varying cell complexities.

The parametric findings on the impact of the number of subdomains in the structure are summarized in Table 3.5. The table presents numerical results alongside graphical representations of the optimized structures' modules for varying sizes of the repeating module. The first key observation is the significant influence of the module scale on the optimized volume. This relationship is evident in Fig. 3.7, where the volume exhibits an almost linear correlation with the number of submodules, a trend that persists even for the higher complexity $3 \times 3 \times 3$ modules. Regarding computational time, a similar relationship is noted. Despite the number of design variables remaining constant, the increase is attributed to the growing number of mechanical constraints. It is important to highlight that in modular optimization, mechanical constraints are evaluated for every member of the structure, not just within the module. Finally, the number of active bars in the optimized module shows little dependence on the module scale.

A graphical representation of the 3D structures is provided in Fig. 3.9, showing isometric views as well as views on the XZ planes for the case with a module featuring a $2 \times 2 \times 2$ ground structure. It is interesting to observe how, with increasing physical dimensions of the module, the optimizer naturally converges toward solutions that prioritize long tensile members and short compressive members to satisfy local buckling constraints. However, as the module size decreases (as seen in the $30 \times 10 \times 15$ results), and consequently, the buckling effective length of the members diminishes the optimized design transitions to a configuration where both tensile and compressive members are

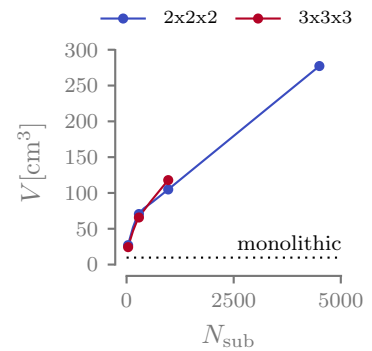


Figure 3.7: Influence of the number of subdomains on the volume of the optimized modular structure.

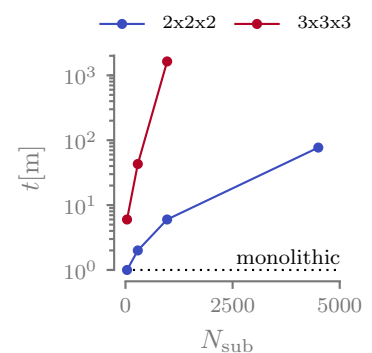


Figure 3.8: Influence of the number of subdomains on the computational time of the optimization.

Table 3.5: Numeric results of the parametric study on the influence of the number of subdomains on the optimized structures.

Quantity	7x3x4	2x2x2				3x3x3		
	1x1x1	6x2x3	12x4x6	18x6x9	30x10x15 ^a	6x2x3	12x4x6	18x6x9
—	—							
$\bar{n}_{\text{opt}} (\bar{n})$	1984	9 (28)	9 (28)	8 (28)	8 (28)	19 (351)	15 (351)	16 (351)
N_{sub}	1	36	288	972	4500	36	288	972
$N_{\text{opt}} (N_{\text{el}})$	20 (1984)	(1008)	(8064)	(27216)	(126000)	(12636)	(101088)	(341172)
$V [\text{cm}^3]$	9.907	27.074	70.559	104.891	277.238	24.323	65.723	117.904
$V [\%]$	1.761	4.812	12.544	18.648	49.288	4.324	11.684	20.960
$C [\text{J}]$	3.71	4.22	3.35	3.19	1.12	3.63	1.84	2.02
$a_{\max} [\text{mm}^2]$	37.61	9.40	5.45	5.45	3.55	5.33	2.60	3.14
φ	100.00 %	14.81 %	1.85 %	0.67 %	0.12 %	20.51 %	1.46 %	0.62 %
ψ	1.000	0.446	0.178	0.105	0.030	0.327	0.127	0.096
t	4 s	6 s	48 s	5 m 6 s	1 h 17 m	5 m 42 s	42 m 50 s	27 h 17 m

^aIn this test case the minimum slenderness limit is relaxed to $\lambda_{\max} = 10$ instead of 15.

50. Sigmund et al. (2016), 'On the (non-)optimality of Michell structures'

present. This observation aligns with the findings of Sigmund on Michell-like structures [50].

In an attempt to understand why the volume is significantly influenced by the number of submodules, we visualize the trends of the parameters φ and ψ in Fig. 3.10. As depicted, every bar in the monolithic structure activates either the buckling or the stress constraint, resulting in $\varphi = 100\%$ and $\psi = 1$. However, this is not true for any of the modular structures, as seen in the case of 12x4x6-3x3x3, where numerous bars remain inactive and are represented in gray.

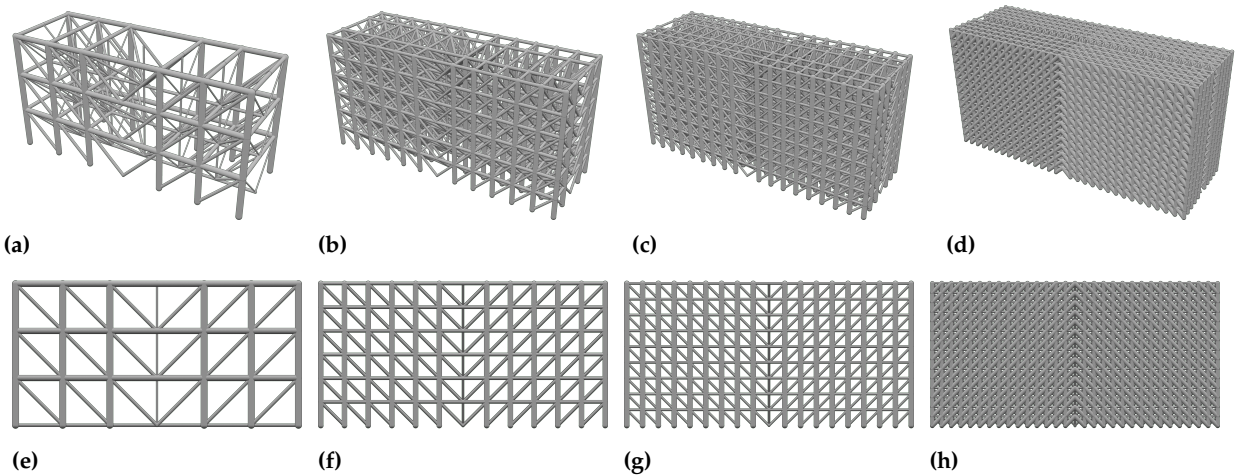


Figure 3.9: Rendering of the optimized structures with $6 \times 2 \times 3$ (a-e), $12 \times 4 \times 6$ (b-f), $18 \times 6 \times 9$ (c-g), and $30 \times 10 \times 15$ (d-h) subdomains. The module presents a $2 \times 2 \times 2$ complexity.

This phenomenon becomes more apparent in Fig. 3.11, where the stress and buckling constraints are plotted to the optimized structures of both the monolithic and the $12 \times 4 \times 6$ - $3 \times 3 \times 3$ cases. In this illustration, it is evident that in the $12 \times 4 \times 6$ - $3 \times 3 \times 3$ case, many bars remain inactive (gray). Examining Fig. 3.11c and d, we notice that the stress and buckling constraints activate only in one submodule but influence the entire structure to display these constraints. As a result, the modular structure is highly redundant and fail-safe, but this comes at the cost of increased total volume.

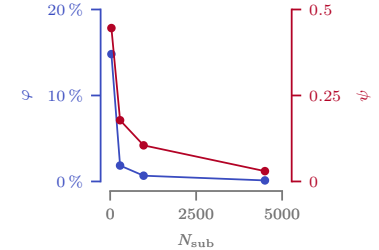


Figure 3.10: Influence of the number of subdomains on the loading metrics φ and ψ of the optimized structures.

INFLUENCE OF THE COMPLEXITY OF THE MODULE We now shift our focus to another parameter of modular structures: the module complexity, defined as the number of candidate members \bar{n} inside a module. To understand how this parameter influences the optimized structures, we set up an analysis similar to the one previously conducted for the module scale. Utilizing the same test case, we divide the structure into $6 \times 2 \times 3$ submodules along the X, Y, and Z axes, respectively. We discretize each module using a $2 \times 2 \times 2$, a $3 \times 3 \times 3$, a $4 \times 4 \times 4$, and a $5 \times 5 \times 5$ fully connected ground structure ($\bar{n} = 28$, $\bar{n} = 351$, $\bar{n} = 2016$, $\bar{n} = 7750$, respectively). The same analysis is conducted on a $12 \times 4 \times 6$ structure to validate the test on a different modular structure.

The results of the parametric study are presented in a tabular format in Table 3.6, along with the rendering of the module. Once again, we have plotted the most interesting aspects separately. The first aspect we examine is how the volume of the optimized structure is influenced by the module complexity \bar{n} . In Fig. 3.13, we observe that an increase in \bar{n} generally has a beneficial effect on volume. However, this effect becomes less pronounced as complexity increases, and in this particular test case, the volume reduction stagnates after the

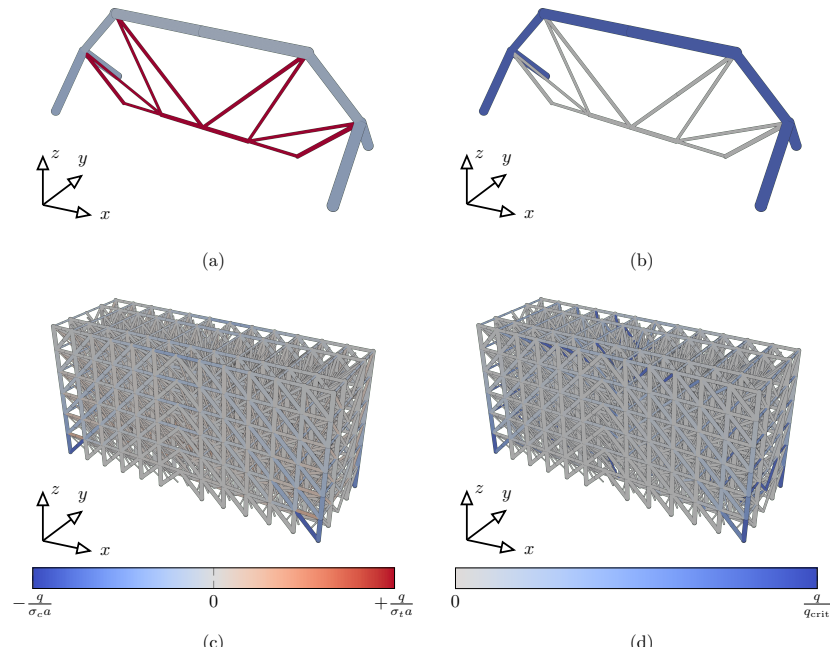


Figure 3.11: Stress (a-c) and local buckling (b-d) failure criteria plotted on the monolithic and the 12x4x6-3x3x3 cases.

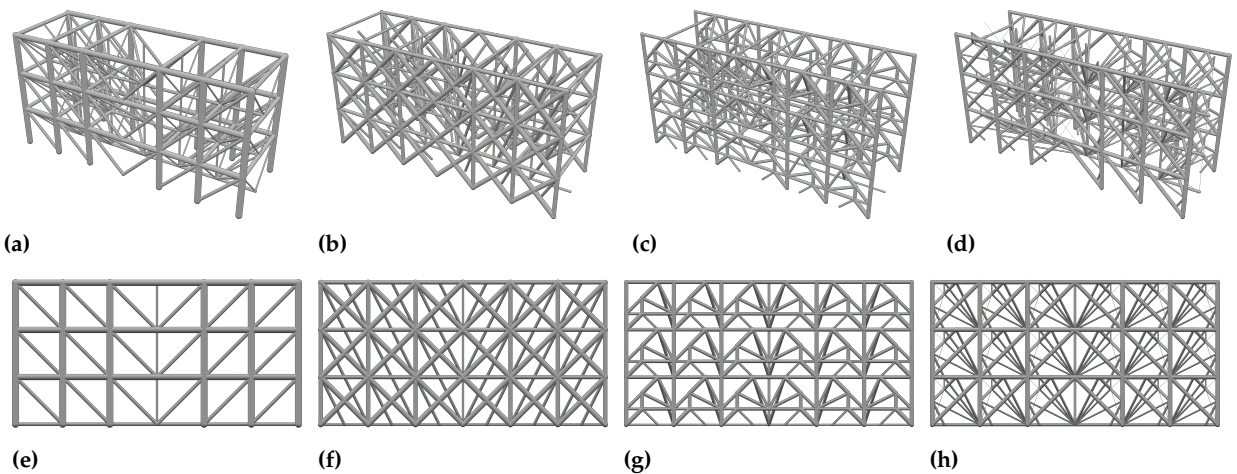
module complexity reaches 4x4x4.

Regarding computational time (see Fig. 3.14), we notice a relationship similar to the one already observed for the submodule scale. The computational time goes up as the module complexity increases. This is understandable because, unlike the case with the number of subdomains, in this scenario, the number of design variables increases along with the number of candidates and, consequently, the constraints.

The 3D renderings of the optimized structures for the 6x2x3 submodules case are presented in Fig. 3.12, allowing the reader to observe the evolution of the module's topology toward greater complexity (from $\bar{n}_{opt} = 9$ to $\bar{n}_{opt} = 88$ for the 2x2x2 and 5x5x5 cases, respectively). While in low complexity, the optimizer prioritizes tensile elements, in more complex cases, we observe the apparition of shorter elements less influenced by local buckling.

Table 3.6: Numeric results of the parametric study on the influence of the module complexity on the optimized structures.

Quantity	6x2x3				12x4x6		
	2x2x2	3x3x3	4x4x4	5x5x5	2x2x2	3x3x3	4x4x4
$\bar{n}_{\text{opt}} (\bar{n})$	9 (28)	19 (351)	88 (2016)	88 (7750)	9 (28)	15 (351)	22 (2016)
N_{sub}	36	36	36	36	288	288	288
$N_{\text{opt}} (N_{\text{el}})$	324 (1008)	468 (12636)	792 (72576)	792 (279000)	2592 (8064)	4320 (101088)	6336 (580608)
$V [\text{cm}^3]$	27.074	24.323	17.098	17.083	70.559	65.723	60.368
$V [\%]$	4.812	4.324	3.040	3.036	12.544	11.684	10.732
$C [\text{J}]$	4.22	3.63	4.49	3.91	3.35	1.84	2.43
$a_{\max} [\text{mm}^2]$	9.40	5.33	3.39	3.77	5.45	2.60	2.97
φ	14.81 %	20.51 %	12.12 %	20.20 %	1.85 %	1.46 %	1.32 %
ψ	0.446	0.327	0.414	0.419	0.178	0.127	0.136
t	6 s	5 m 42 s	14 m 20 s	3 h 17 m	48 s	42 m 50 s	32 h 4 m

**Figure 3.12:** Rendering of the optimized structures with 2x2x2 (a-e), 3x3x3 (b-f), 4x4x4 (c-g), and 5x5x5 (d-h) module complexity. The number of subdomains is 6x2x3.

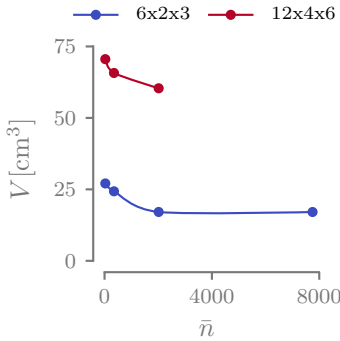


Figure 3.13: Influence of the module complexity on the volume of the optimized modular structure.

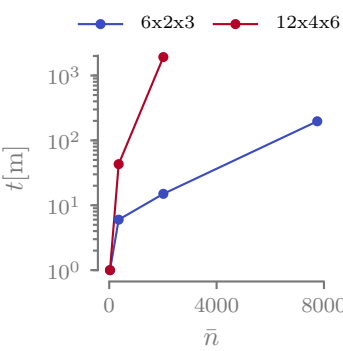


Figure 3.14: Influence of the module complexity on the computational time of the optimization.

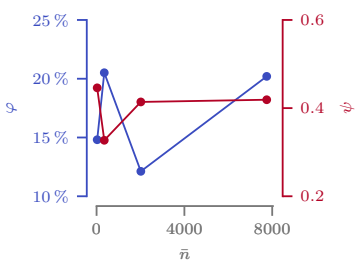


Figure 3.15: Influence of the module complexity on the loading metrics φ and ψ of the optimized structures.

It is interesting to note that the number of active bars in the optimized structure is quite dependent on the complexity of the module. However, in this specific case, we see that it saturates at $\bar{n} = 88$ in the $6 \times 2 \times 3$ case, suggesting that we have reached the convergence of the discretization.

Finally, in Fig. 3.15, we present the numerical values of φ and ψ . Unlike our earlier observations, the trends of these parameters are not monotonic and do not follow an explicit trend. While these indices aid in understanding how much a truss is loaded, they don't necessarily provide clear hints on optimality. A structure loaded to the maximum of the material contributes to achieving a lighter design but is not sufficient, as this example demonstrates.

DESIGN OF EXPERIMENTS With the data gathered thus far, we aim to construct the Design of experiments (DOE) for optimized modular structures. The objective is to monitor how the outcomes vary by introducing a change in the preconditions, represented by one or more independent variables. In our case, the chosen independent variables are the number of subdomains N_{sub} (x_1) and module complexity \bar{n} (x_2), while the observed responses are the total structural volume V and the computational time t . For simplicity, we continue to limit ourselves to cubic cells.

We have chosen to use a quadratic model with interaction (the term $x_1 x_2$) in an attempt to capture a potential interference between x_1 and x_2 , represented as follows:

$$a x_1^2 + b x_2^2 + c x_1 x_2 + d x_1 + e x_2 + f \quad (3.11)$$

The coefficients are determined by solving a least squares system using the data presented earlier in this section.

We present the outcomes of the DOE in Fig. 3.16 for the structure volume V . In the upper part of the image, we display the surface response along with a scatter plot of the optimized structures (a), and additionally, the isovalue lines plot (b). It is noticeable that the volume V is strongly influenced by the number of subdomains N_{sub} , as indicated by the horizontal orientation of the isovalue lines. This suggests that the steepest gradient of the function is in the vertical direction. Less voluminous modular structures tend to be structures with fewer subdomains characterized by high complexity \bar{n} . However, when examining subfigures (c) and (d), representing the surface response for computational time t , it is evident that high module complexity \bar{n} is associated with an elevated computational time.

The coefficients of the quadratic model are given in Table 3.7 and Table 3.8 for the volume and computational time, respectively. We see that for the volume the coefficient that defines the most the behavior

of the response surface is e , the coefficient that relates to the linear term for the number of subdomains. The interaction between the two independent variables – the coefficient c – is low, showing that the two variables do not add up when modified together. This is not true for the computation time, where the interaction coefficient is relevant, together with the two linear terms. Once again, the quadratic coefficients a and b are less important, suggesting in general a linear response.

The coefficients of the quadratic model are presented in Table 3.7 and Table 3.8 for the volume and computational time, respectively. Notably, for the volume V , the coefficient that predominantly influences the behavior of the response surface is e , which corresponds to the linear term for the number of subdomains N_{sub} . The interaction coefficient between the two independent variables, denoted as c , is low, indicating that the two variables do not significantly contribute when modified together. This is in contrast to computational time, where the interaction coefficient is relevant, along with the two linear terms. In the two cases, the quadratic coefficients a and b are relatively less important, suggesting a generally linear response.

Finally, we present the main effects plot for the volume and module complexity in Fig. 3.17. The concept is to plot, for each factor or interaction, the effect (summed with the overall mean) as a function of the level. The advantage of this representation is to offer an immediate visualization of the various effects.

DISCUSSION ON THE DOE We can utilize this DOE as a tool to give general recommendations. While the specific numeric values and their magnitudes just found are tailored to the presented example, we assume that the observed trends are generally correct and applicable to modular structures as a whole. Therefore, we can conclude that in scenarios where minimizing mass is the primary objective, aiming for the fewest possible number of subdomains is preferred. However, additional constraints must be considered. For example, having fewer subdomains implies an increase in the physical size of individual submodules. Yet, there is often a manufacturing maximum size that restricts this increase. Consequently, the recommendation is to achieve the largest possible subdomains that can be produced within the limitations of the chosen manufacturing technology.

Although higher complexity significantly impacts computational time, its influence on optimization outcomes is not substantial. Therefore, opting for a medium complexity, such as 3x3x3 nodes in the module (or 4x4 in 2D), strikes a balance between computational cost and optimization effectiveness.

Coeff.	Value
a	9.00×10^{-8}
b	-1.02×10^{-5}
c	-1.77×10^{-6}
d	-2.64×10^{-3}
e	1.01×10^{-1}
f	2.88×10^1

Table 3.7: Coefficients of the quadratic function used to model how the volume V varies with the number of subdomains N_{sub} and the module complexity \bar{n} .

Coeff.	Value
a	1.55×10^{-3}
b	-2.87×10^{-4}
c	2.90×10^{-1}
d	-2.08×10^1
e	-5.54
f	0.00

Table 3.8: Coefficients of the quadratic function used to model how the computational time t varies with the number of subdomains N_{sub} and the module complexity \bar{n} .

3.2.3 COMPARISON WITH THE OPTIMIZED OCTET-TRUSS

The proposed modular TTO algorithm is benchmarked against one of the most popular cell topologies found in the literature: the octet-truss (see Fig. 3.18). The octet-truss is a cell known for its highly effective mechanical properties, achieving about half the theoretical values of the upper Hashin-Shtrikman bounds [94] for isotropic materials.

To conduct the benchmark, the simply supported 3D beam is divided into $6 \times 2 \times 3$ and $12 \times 4 \times 6$ cubic subdomains, which are then populated with the octet-truss topology. The cross-sectional areas of the cell members are all equal, and the numerical value is determined by performing a parametric optimization. The octet-truss structure is constrained by stress, local buckling, and kinematic compatibility constraints for every member of the structure. The optimization is performed using Altair OptiStruct.

[94]. Deshpande et al. (2001), 'Effective properties of the octet-truss lattice material'

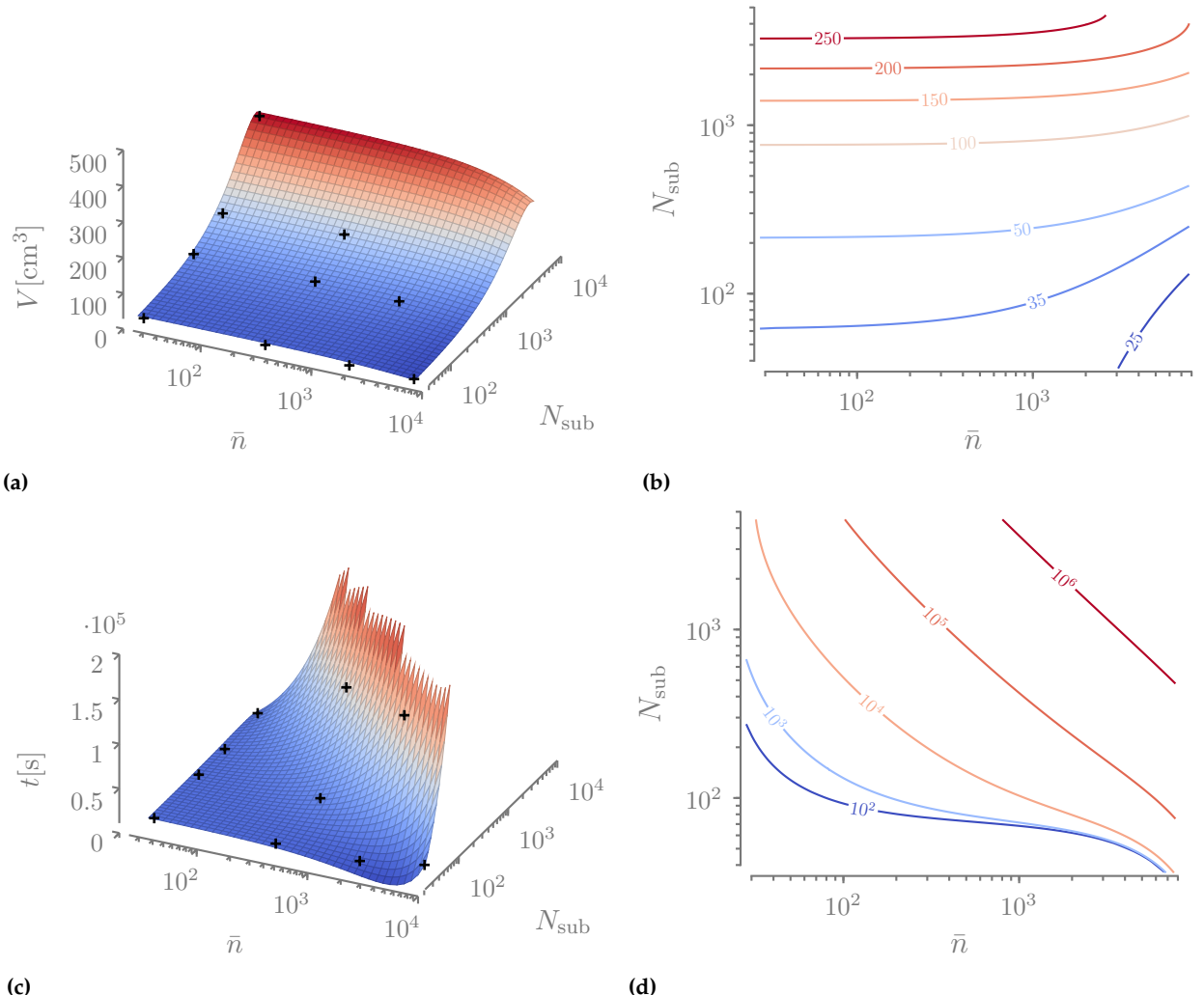


Figure 3.16: Design of experiments (DOE) response curves and isocurves plot for the volume (a-b) and computational time (c-d).

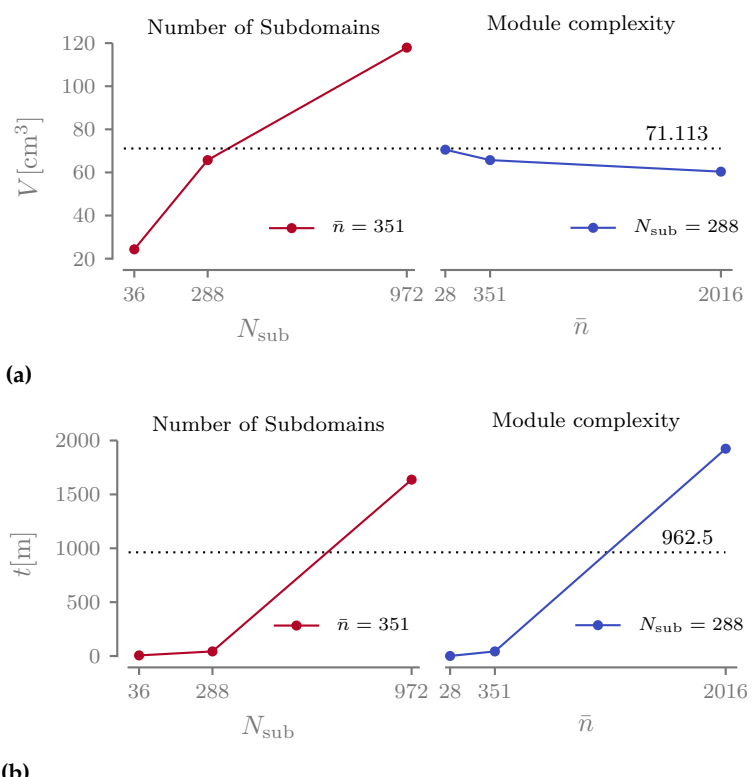


Figure 3.17: Main effects plot of volume (a) and computational time (b).

Fig. 3.19 displays the 3D rendering of the two optimized octet-truss structures (left part of the image) compared to the modular TTO structures (right part of the image). It is noticeable how the TTO algorithm guides the topology of the module toward higher efficiency, creating vertical columns loaded in compression that support thin wires loaded in tension. On the other hand, the octet-truss topology is fixed and exhibits quasi-isotropic mechanical behavior. The octet-truss is a module with good homogenized elastic properties in all directions, thanks to its numerous planes of symmetry. It is, thus, less suitable for structural applications where all the subdomains experience similar loading conditions. In such cases, the module will be equally stiff and strong in every direction, not aligned with the principal stress directions.

We notice that in the octet-truss structure, there are no members orientated exactly along the z axis, while in the TTO optimized cell, they are the most massive. This tells us that this is the most efficient direction to put the material to get a strong cell. On top of that, the upper and lower faces of the cell present a cross design (see Fig. 3.18) that works well for torque but not for tension and compression loading. A new study exploring what happens if we rotate the cell could be interesting.

The numerical results are presented in Table 3.9 and confirm our observations. The volume of the octet-truss structures is approximately three times and twice the volume of the modular TTO optimized structures for the 6x2x3 and the 12x4x6 test cases, respectively. This significant gap between the two types of structures is also evident when examining the values of φ and ψ . These values drop to very low levels because the cross-sectional value of the entire structure is determined by the value at which a bar on the structure becomes critical. For these structures, only four bars are critical (due to symmetry). Better results could have been obtained by providing more design freedom to the optimization of the octet-truss, using multiple cross-sectional design variables, but this approach has not been taken here. It is important to note that the comparison presented here does not account for the weight of fasteners and joints necessary to link the

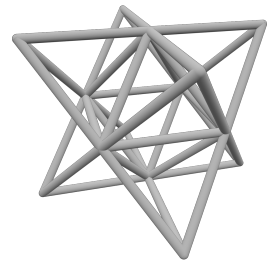


Figure 3.18: Rendering of a single octet-truss module.

Quantity	6x2x3		12x4x6	
	Octet	3x3x3	Octet	3x3x3
N_{sub}	36	36	288	288
$N_{\text{opt}} (N_{\text{el}})$	1008	468 (12636)	7488	4320 (101088)
$V [\text{cm}^3]$	65.752	24.323	121.038	65.723
$V [\%]$	11.692	4.324	21.524	11.684
$C [\text{J}]$	1.67	3.63	1.12	1.84
$a_{\max} [\text{mm}^2]$	3.69	5.33	1.83	2.60
φ	0.39 %	20.51 %	0.05 %	1.46 %
ψ	0.075	0.327	0.026	0.127

Table 3.9: Numerical results of the comparison between octet-truss and TTO structures.

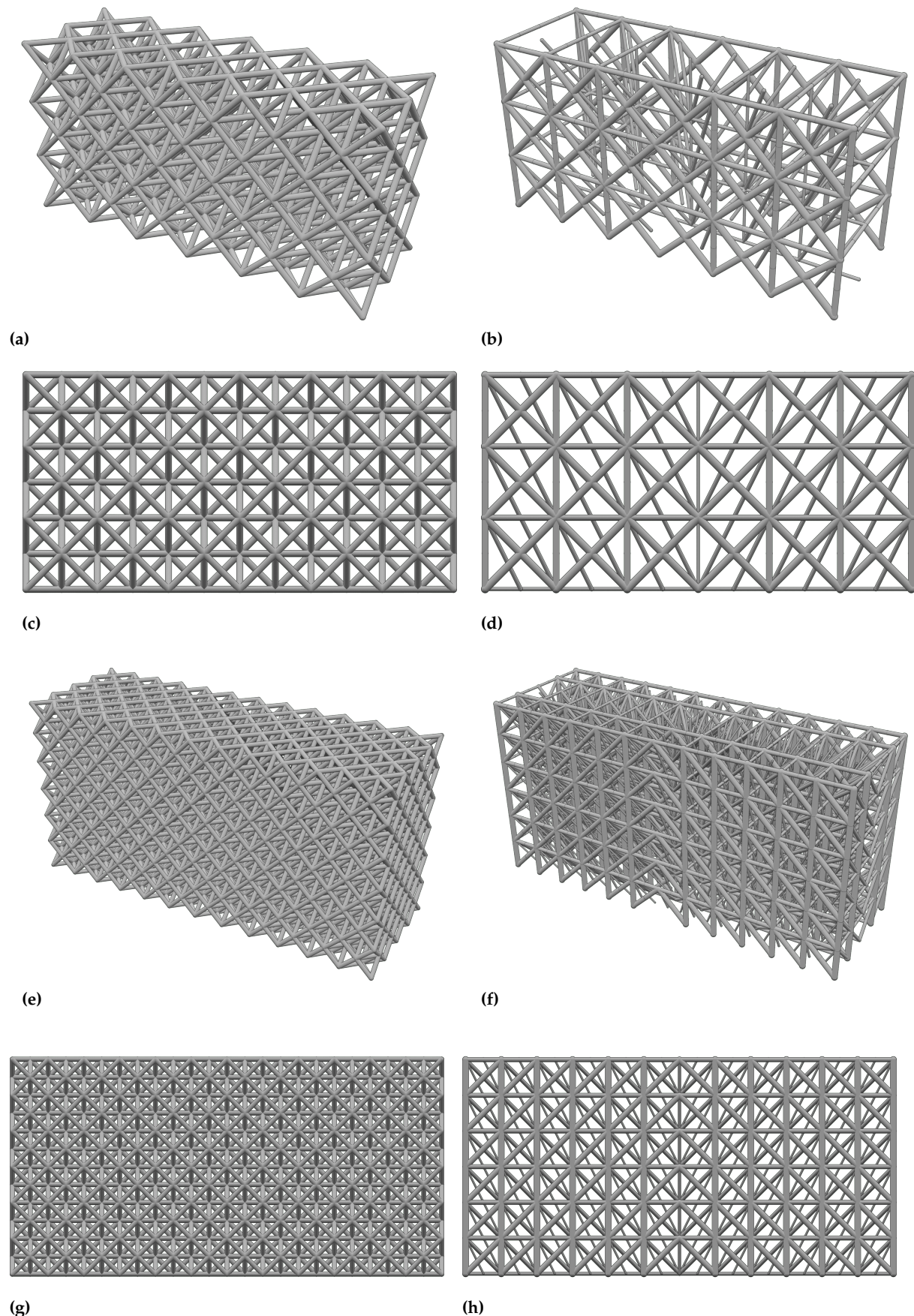


Figure 3.19: Comparison of the octet-truss structures (a-c-e-g) and the TTO structures (b-d-f-h) for two different numbers of submodules, 6x2x3 and 12x4x6.

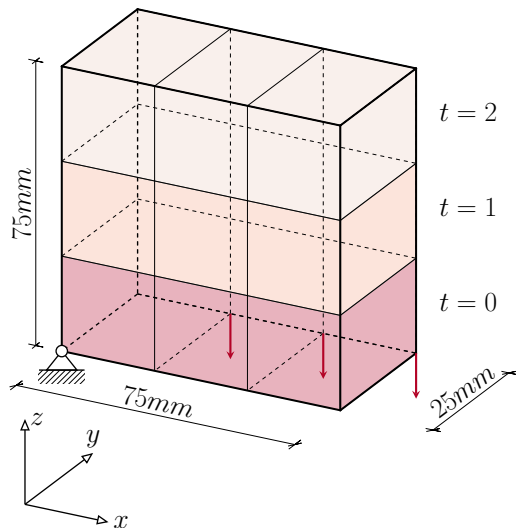


Figure 3.20: Graphical representation of the given module layout for the simply supported 3D beam.

cells together.

3.2.4 USING MULTIPLE MODULE TOPOLOGIES

We have explored two extremes so far – the fully modular and the monolithic structures. Now, we aim to investigate the scenarios in between. Up to this point, our study on modular structures has been limited to a single topology of the module, i.e., $N_T = 1$. This is because, when dealing with multiple module topologies, another crucial question arises: how to optimize the module layout? How should the modules be arranged in the structure to minimize the overall volume of the part? This critical question will be discussed in-depth later in the thesis. For now, as we begin to consider multiple module topologies, we make a significant simplification by determining the layout based solely on good engineering common sense, without an additional optimization process.

Let us reconsider the simply supported 3D beam divided into a grid of $6 \times 2 \times 3$ subdomains. This time, we optimize the structure using three different modules $N_T = 3$. The modules are discretized using an equal fully connected ground structure with $3 \times 3 \times 3$ nodes. The module mapping matrix of the structure is provided as an input for the optimization¹ and it represents the module layout shown in Fig. 3.20.

The optimized structure features an interesting design made by two elongated spars that support multiple tensile members responsible for carrying the given loads. The spars exhibit a design that favors long tensile members, interconnected by compressive bars. The resulting optimized structure is illustrated in Figure 3.21.

We now examine the modules of the optimized structure. Firstly, we observe that the optimizer sets all the cross-sectional areas of module $t = 2$ to zero, judging it as unimportant for the mass optimization of the structure. This highlights the importance of considering the possibility

1: The module mapping matrix is

$$H = \begin{bmatrix} 1 & 0 & 0 \\ 1 & 0 & 0 \\ 1 & 0 & 0 \\ 0 & 0 & 0 \\ 0 & 1 & 0 \\ 0 & 1 & 0 \\ 0 & 1 & 0 \\ 0 & 1 & 0 \\ 0 & 0 & 1 \\ 0 & 0 & 1 \\ 0 & 0 & 1 \end{bmatrix}$$

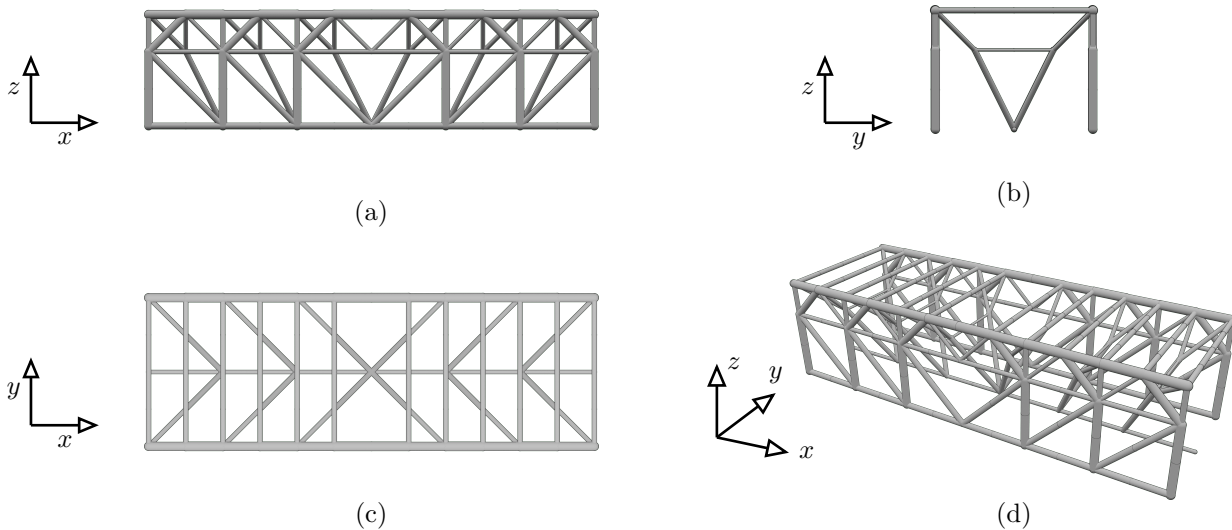


Figure 3.21: Orthographic views of the topology of the optimized modular simply supported 3D beam. (a) XZ plane (b) YZ plane (c) XY plane (d) auxiliary perspective view.

of an empty topology when optimizing the module layout in the structure. Secondly, we note instances where the module is composed of bars that are disconnected e.g. in $t = 0$, potentially necessitating additional post-processing for obtaining a manufacturable design.

The optimized structure with $N_T = 3$ is now compared to the reference monolithic structure and the $6 \times 2 \times 3 - 3 \times 3 \times 3$ structure with $N_T = 3$ to assess the difference in mechanical performance due to the increased number of modules. The results are presented in Table 3.10. Interestingly, the computational time of the $N_T = 1$ solution is lower ($t = 3 \text{ m } 22 \text{ s}$) compared to the $N_T = 3$ structure ($t = 5 \text{ m } 42 \text{ s}$). This comes as a surprise, considering that the $N_T = 1$ optimization problem involves more design variables (as three times the number of cross-sectional areas are optimized). However, it turns out that having more design freedom makes the optimization process easier, as the constraints are more straightforward to satisfy. The trends of the volume and computational time are illustrated graphically in Fig. 3.22.

The volume reduction is attributed to a more efficient utilization of the subdomains' topology, which now varies with the subdomain position. This can be observed by examining the more efficient use of material, with a greater number of bars reaching the mechanical failure limit ($\varphi = 61.90\%$ for $N_t = 3$ compared to $\varphi = 61.90\%$ for $N_t = 1$) and, in general, a more uniform structure loading ($\psi = 0.716$ vs. $\psi = 0.327$). The stress and buckling failure criteria are shown in Fig. 3.23 for further insight.

This study suggests that employing more modules for optimization allows the achievement of less voluminous structures, potentially

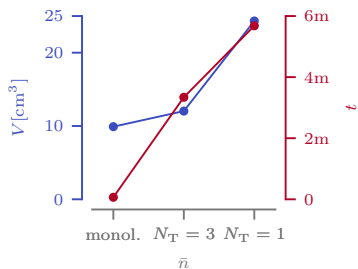


Figure 3.22: Comparison of the volume and computational time of the structure with multiple modules with the monolithic and the fully modular structures.

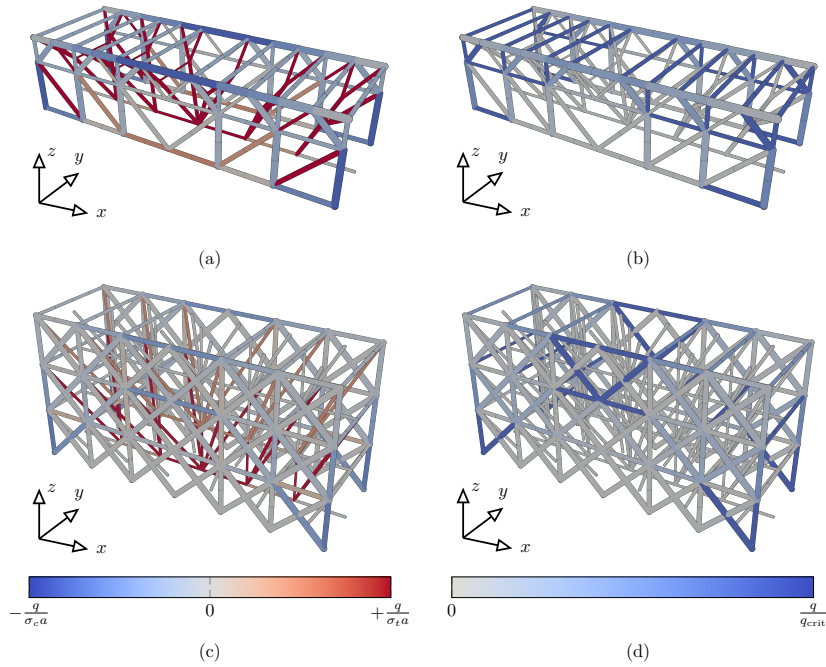


Figure 3.23: Stress (a-c) and local buckling (b-d) failure criteria plotted on the multiple and single module modular structures.

approaching the performance of monolithic structures. However, this introduces a compromise between volume (and consequently mass) and the ease of manufacturing, a topic we will delve into further in the upcoming chapter.

Table 3.10: Numerical results of the comparison between the structure with multiple modules with the monolithic and the fully-modular structures.

Quantity	7x3x4	6x2x3-3x3x3- $N_T = 3$			6x2x3 3x3x3 $N_T = 1$
	-	$t = 0$	$t = 1$	$t = 2$	$t = 0$
	-				
$\bar{n}_{\text{opt}} (\bar{n})$	1984	10 (351)	18 (351)	- (351)	19 (351)
N_{sub}	1		36		36
$N_{\text{opt}} (N_{\text{el}})$	20 (1984)		336 (12636)		468 (12636)
$V [\text{cm}^3]$	9.907		12.032		24.323
$V [\%]$	1.761		2.139		4.324
$C [\text{J}]$	3.71		6.14		3.63
$a_{\max} [\text{mm}^2]$	37.61		7.13		5.33
φ	100.00 %		61.90 %		20.51 %
ψ	1.000		0.716		0.327
t	4 s		3 m 22 s		5 m 42 s

3.3 CONCLUSION

In this chapter, we introduced a modular structure optimization algorithm based on the Truss Topology Optimization (TTO) and variable linking. Initially, we investigated the impact of modularity constraints on the topological buckling phenomenon and sensitivity analysis. Subsequently, we adapted the two-step optimization algorithm with reinitialization presented in Chapter 2 to solve the proposed modular formulation.

The modular TTO algorithm is then tested on multiple two- and three-dimensional test cases. Initially, we observe an equivalence between modular structures and structures loaded with multiple load cases. The utilization of a repeating module throughout the structure significantly impacts the volume, as the module needs to perform well under various loading conditions concurrently. Subsequently, we conducted an extensive parametric analysis of the number of subdomains and module complexity. Based on the results of the Design of experiments (DOE), we provide recommendations: fewer subdomains are generally preferable, with the module as large as manufacturably possible. Module complexity plays a role in volume minimization but has a relatively low impact. Finally, the modular TTO structures are benchmarked against one of the most commonly used module topologies in the literature: the octet-truss lattice.

At the end of the chapter, we conducted a final optimization using multiple module topologies. The incorporation of multiple modules, some of which may have an entirely empty topology, emerged as a crucial factor that contributes to the reduction of modular structure volume. This approach allows modular structures to approach the volume of monolithic structures while offering additional ease of

manufacturing. However, the utilization of multiple modules raises a new question: how are the modules arranged within the different subdomains of the structure?

BIBLIOGRAPHY

- [1] Stragiotti, Enrico, Irisarri, François-Xavier, Julien, Cédric, and Morlier, Joseph, 'Towards manufactured lattice structures: a comparison between layout and topology optimization', *AeroBest 2021 International Conference on Multidisciplinary Design Optimization of Aerospace Systems. Book of proceedings*, Lisbon, Portugal: ECCOMAS, July 2021, pp. 229–244. cited on page 1
- [2] Dorn, W. S., Gomory, Ralph E., and Greenberg, H., 'Automatic design of optimal structures', *J. Mécanique* (1964). cited on pages 1, 12, 13, 26, 36
- [3] Chan, H. S. Y., 'Optimum structural design and linear programming', *College of Aeronautics Report Aero 175* (1964), Publisher: College of Aeronautics Cranfield. cited on pages 1, 12
- [4] Hemp, W. S., 'Optimum Structures'. Clarendon Press, 1973, Google-Books-ID: cJhpAAAAMAAJ. ISBN: 978-0-19-856110-1 cited on pages 1, 11, 12, 26
- [5] Sankaranarayanan, S., Haftka, Raphael T., and Kapuria, Rakesh K., 'Truss topology optimization with simultaneous analysis and design', *AIAA Journal* 32.2 (Feb. 1994), pp. 420–424. doi: 10.2514/3.12000 cited on pages 1, 30
- [6] Bendsøe, Martin Philip and Kikuchi, Noboru, 'Generating optimal topologies in structural design using a homogenization method', *Computer Methods in Applied Mechanics and Engineering* 71.2 (Nov. 1988), pp. 197–224. doi: 10.1016/0045-7825(88)90086-2 cited on pages 1, 16
- [7] Bendsøe, M. P., 'Optimal shape design as a material distribution problem', *Structural optimization* 1.4 (Dec. 1989), pp. 193–202. doi: 10.1007/BF01650949 cited on pages 1, 3, 13, 23
- [8] Sigmund, Ole, 'Materials with prescribed constitutive parameters: An inverse homogenization problem', *International Journal of Solids and Structures* 31.17 (Sept. 1994), pp. 2313–2329. doi: 10.1016/0020-7683(94)90154-6 cited on page 1
- [9] Zhang, Weihong and Sun, Shiping, 'Scale-related topology optimization of cellular materials and structures', *International Journal for Numerical Methods in Engineering* 68.9 (2006), pp. 993–1011. doi: 10.1002/nme.1743 cited on pages 1, 51
- [10] Sigmund, Ole, 'Manufacturing tolerant topology optimization', *Acta Mechanica Sinica* 25.2 (Apr. 2009), pp. 227–239. doi: 10.1007/s10409-009-0240-z cited on page 1
- [11] Brackett, D, Ashcroft, I, and Hague, R, 'Topology Optimization for Additive Manufacturing' (2011), p. 15. doi: 10.26153/tsw/15300 cited on page 1

- cited on page 2
- [12] Tortorelli, D. A. and Michaleris, P., 'Design sensitivity analysis: Overview and review', *Inverse Problems in Engineering* 1.1 (Oct. 1994), pp. 71–105.
DOI: [10.1080/174159794088027573](https://doi.org/10.1080/174159794088027573)
- cited on pages 2, 10
- [13] Martins, J.R.R.A. and Ning, A., 'Engineering Design Optimization'. Cambridge University Press, 2021.
ISBN: [978-1-108-83341-7](#)
- cited on pages 2, 10, 13
- [14] Bendsøe, Martin P. and Sigmund, Ole, 'Topology Optimization'. Berlin, Heidelberg: Springer Berlin Heidelberg, 2004.
ISBN: [978-3-642-07698-5 978-3-662-05086-6](#)
- cited on pages 3, 4
- [15] Wang, Fengwen, Lazarov, Boyan Stefanov, and Sigmund, Ole, 'On projection methods, convergence and robust formulations in topology optimization', *Structural and Multidisciplinary Optimization* 43.6 (June 2011), pp. 767–784.
DOI: [10.1007/s00158-010-0602-y](https://doi.org/10.1007/s00158-010-0602-y)
- cited on page 3
- [16] Bendsøe, M. P. and Sigmund, O., 'Material interpolation schemes in topology optimization', *Archive of Applied Mechanics* 69.9 (Nov. 1999), pp. 635–654.
DOI: [10.1007/s004190050248](https://doi.org/10.1007/s004190050248)
- cited on page 3
- [17] Hashin, Z. and Shtrikman, S., 'A variational approach to the theory of the elastic behaviour of multiphase materials', *Journal of the Mechanics and Physics of Solids* 11.2 (Mar. 1963), pp. 127–140.
DOI: [10.1016/0022-5096\(63\)90060-7](https://doi.org/10.1016/0022-5096(63)90060-7)
- cited on page 3
- [18] Díaz, A. and Sigmund, O., 'Checkerboard patterns in layout optimization', *Structural optimization* 10.1 (Aug. 1995), pp. 40–45.
DOI: [10.1007/BF01743693](https://doi.org/10.1007/BF01743693)
- cited on page 4
- [19] Sigmund, Ole, 'Design of Material Structures using Topology Optimization', PhD thesis, Technical University of Denmark, DK-2800 Lyngby, 1994.
- cited on page 4
- [20] Sigmund, Ole, 'On the Design of Compliant Mechanisms Using Topology Optimization', *Mechanics of Structures and Machines* 25.4 (Jan. 1997), pp. 493–524.
DOI: [10.1080/08905459708945415](https://doi.org/10.1080/08905459708945415)
- cited on pages 4, 16
- [21] Sigmund, Ole, 'Morphology-based black and white filters for topology optimization', *Structural and Multidisciplinary Optimization* 33.4 (Apr. 2007), pp. 401–424.
DOI: [10.1007/s00158-006-0087-x](https://doi.org/10.1007/s00158-006-0087-x)
- cited on pages 4, 15
- [22] Ferrari, Federico and Sigmund, Ole, 'A new generation 99 line Matlab code for compliance topology optimization and its extension to 3D', *Structural and Multidisciplinary Optimization* 62.4 (Oct. 2020), pp. 2211–2228.
DOI: [10.1007/s00158-020-02629-w](https://doi.org/10.1007/s00158-020-02629-w)

- [23] Achtziger, Wolfgang and Kanzow, Christian, 'Mathematical programs with vanishing constraints: optimality conditions and constraint qualifications', *Mathematical Programming* 114.1 (July 2008), pp. 69–99.
doi: [10.1007/s10107-006-0083-3](https://doi.org/10.1007/s10107-006-0083-3)
- [24] Cheng, Gengdong and Jiang, Zheng, 'Study on Topology Optimization with Stress Constraints', *Engineering Optimization* 20.2 (Nov. 1992), pp. 129–148.
doi: [10.1080/03052159208941276](https://doi.org/10.1080/03052159208941276)
- [25] Duysinx, P. and Bendsøe, M. P., 'Topology optimization of continuum structures with local stress constraints', *International Journal for Numerical Methods in Engineering* 43.8 (1998), pp. 1453–1478.
doi: [10.1002/\(SICI\)1097-0207\(19981230\)43:8<1453::AID-NME480>3.0.CO;2-2](https://doi.org/10.1002/(SICI)1097-0207(19981230)43:8<1453::AID-NME480>3.0.CO;2-2)
- [26] Le, Chau, Norato, Julian, Bruns, Tyler, Ha, Christopher, and Tortorelli, Daniel, 'Stress-based topology optimization for continua', *Structural and Multidisciplinary Optimization* 41.4 (Apr. 2010), pp. 605–620.
doi: [10.1007/s00158-009-0440-y](https://doi.org/10.1007/s00158-009-0440-y)
- [27] Verbart, Alexander, Langelaar, Matthijs, and Keulen, Fred van, 'A unified aggregation and relaxation approach for stress-constrained topology optimization', *Structural and Multidisciplinary Optimization* 55.2 (Feb. 2017), pp. 663–679.
doi: [10.1007/s00158-016-1524-0](https://doi.org/10.1007/s00158-016-1524-0)
- [28] Holmberg, Erik, Torstenfelt, Bo, and Klarbring, Anders, 'Stress constrained topology optimization', *Structural and Multidisciplinary Optimization* 48.1 (2013), pp. 33–47.
doi: [10.1007/s00158-012-0880-7](https://doi.org/10.1007/s00158-012-0880-7)
- [29] Silva, Gustavo Assis da, Beck, André Teófilo, and Sigmund, Ole, 'Stress-constrained topology optimization considering uniform manufacturing uncertainties', *Computer Methods in Applied Mechanics and Engineering* 344 (Feb. 2019), pp. 512–537.
doi: [10.1016/j.cma.2018.10.020](https://doi.org/10.1016/j.cma.2018.10.020)
- [30] Rozvany, G.I.N., 'On design-dependent constraints and singular topologies', *Structural and Multidisciplinary Optimization* 21.2 (Apr. 2001), pp. 164–172.
doi: [10.1007/s001580050181](https://doi.org/10.1007/s001580050181)
- [31] Stolpe, Mathias, 'On Models and Methods for Global Optimization of Structural Topology', Publisher: Matematik, PhD thesis, 2003.
- [32] Sved, G. and Ginos, Z., 'Structural optimization under multiple loading', *International Journal of Mechanical Sciences* 10.10 (Oct. 1968), pp. 803–805.
doi: [10.1016/0020-7403\(68\)90021-0](https://doi.org/10.1016/0020-7403(68)90021-0)

- cited on page 7
- [33] Cheng, G. D. and Guo, X., ' ε -relaxed approach in structural topology optimization', *Structural optimization* 13.4 (June 1997), pp. 258–266.
DOI: [10.1007/BF01197454](https://doi.org/10.1007/BF01197454)
- cited on page 7
- [34] Silva, Gustavo Assis da, Aage, Niels, Beck, André Teófilo, and Sigmund, Ole, 'Local versus global stress constraint strategies in topology optimization: A comparative study', *International Journal for Numerical Methods in Engineering* 122.21 (2021), pp. 6003–6036.
DOI: [10.1002/nme.6781](https://doi.org/10.1002/nme.6781)
- cited on page 8
- [35] Kreisselmeier, G. and Steinhauser, R., 'Systematic Control Design by Optimizing a Vector Performance Index', *IFAC Proceedings Volumes*, IFAC Symposium on computer Aided Design of Control Systems, Zurich, Switzerland, 29–31 August 12.7 (Sept. 1979), pp. 113–117.
DOI: [10.1016/S1474-6670\(17\)65584-8](https://doi.org/10.1016/S1474-6670(17)65584-8)
- cited on page 11
- [36] Maxwell, J. Clerk, 'I.—On Reciprocal Figures, Frames, and Diagrams of Forces', *Earth and Environmental Science Transactions of The Royal Society of Edinburgh* 26.1 (1870), Publisher: Royal Society of Edinburgh Scotland Foundation, pp. 1–40.
DOI: [10.1017/S0080456800026351](https://doi.org/10.1017/S0080456800026351)
- cited on pages 11, 13, 58
- [37] Michell, A. G. M., 'The limits of economy of material in frame-structures', *The London, Edinburgh, and Dublin Philosophical Magazine and Journal of Science* 8.47 (Nov. 1904), pp. 589–597.
DOI: [10.1080/14786440409463229](https://doi.org/10.1080/14786440409463229)
- cited on pages 12, 13
- [38] Gilbert, Matthew and Tyas, Andrew, 'Layout optimization of large-scale pin-jointed frames', *Engineering Computations* 20.8 (Dec. 2003), pp. 1044–1064.
DOI: [10.1108/02644400310503017](https://doi.org/10.1108/02644400310503017)
- cited on page 12
- [39] Pedersen, Pauli, 'Optimal Joint Positions for Space Trusses', *Journal of the Structural Division* 99.12 (Dec. 1973), Publisher: American Society of Civil Engineers, pp. 2459–2476.
DOI: [10.1061/JSDEAG.0003669](https://doi.org/10.1061/JSDEAG.0003669)
- cited on page 12
- [40] Achtziger, Wolfgang, 'On simultaneous optimization of truss geometry and topology', *Structural and Multidisciplinary Optimization* 33.4 (Apr. 2007), pp. 285–304.
DOI: [10.1007/s00158-006-0092-0](https://doi.org/10.1007/s00158-006-0092-0)
- cited on page 12
- [41] Descamps, Benoît and Filomeno Coelho, Rajan, 'A lower-bound formulation for the geometry and topology optimization of truss structures under multiple loading', *Structural and Multidisciplinary Optimization* 48.1 (July 2013), pp. 49–58.
DOI: [10.1007/s00158-012-0876-3](https://doi.org/10.1007/s00158-012-0876-3)
- cited on page 12
- [42] He, L. and Gilbert, M., 'Rationalization of trusses generated via layout optimization', *Structural and Multidisciplinary Optimization* 52.4 (Oct. 2015), pp. 677–694.

- DOI: [10.1007/s00158-015-1260-x](https://doi.org/10.1007/s00158-015-1260-x)
- [43] Lu, Hongjia and Xie, Yi Min, 'Reducing the number of different members in truss layout optimization', *Structural and Multidisciplinary Optimization* 66.3 (Feb. 2023), p. 52.
DOI: [10.1007/s00158-023-03514-y](https://doi.org/10.1007/s00158-023-03514-y) cited on page 12
- [44] Parkes, E.W., 'Joints in optimum frameworks', *International Journal of Solids and Structures* 11.9 (Sept. 1975), pp. 1017–1022.
DOI: [10.1016/0020-7683\(75\)90044-X](https://doi.org/10.1016/0020-7683(75)90044-X) cited on page 13
- [45] Watts, Seth, Arrighi, William, Kudo, Jun, Tortorelli, Daniel A., and White, Daniel A., 'Simple, accurate surrogate models of the elastic response of three-dimensional open truss micro-architectures with applications to multiscale topology design', *Structural and Multidisciplinary Optimization* 60.5 (Nov. 2019), pp. 1887–1920.
DOI: [10.1007/s00158-019-02297-5](https://doi.org/10.1007/s00158-019-02297-5) cited on page 13
- [46] Svanberg, Krister, 'The method of moving asymptotes—a new method for structural optimization', *International Journal for Numerical Methods in Engineering* 24.2 (1987), pp. 359–373.
DOI: <https://doi.org/10.1002/nme.1620240207> cited on page 15
- [47] Johnson, Steven G., 'The NLOpt nonlinear-optimization package', <https://github.com/stevengj/nlopt>, 2007. cited on page 15
- [48] Diamond, Steven and Boyd, Stephen, 'CVXPY: A Python-Embedded Modeling Language for Convex Optimization', 2016. cited on pages 15, 37, 56
- [49] Domahidi, Alexander, Chu, Eric, and Boyd, Stephen, 'ECOS: An SOCP solver for embedded systems', 2013 European Control Conference (ECC), Zurich: IEEE, July 2013, pp. 3071–3076, ISBN: 978-3-033-03962-9.
DOI: [10.23919/ECC.2013.6669541](https://doi.org/10.23919/ECC.2013.6669541) cited on pages 15, 37, 56
- [50] Sigmund, Ole, Aage, Niels, and Andreassen, Erik, 'On the (non-)optimality of Michell structures', *Structural and Multidisciplinary Optimization* 54.2 (Aug. 2016), pp. 361–373.
DOI: [10.1007/s00158-016-1420-7](https://doi.org/10.1007/s00158-016-1420-7) cited on pages 16, 23, 27, 60
- [51] Bruggi, Matteo and Duysinx, Pierre, 'Topology optimization for minimum weight with compliance and stress constraints', *Structural and Multidisciplinary Optimization* 46.3 (Sept. 2012), pp. 369–384.
DOI: [10.1007/s00158-012-0759-7](https://doi.org/10.1007/s00158-012-0759-7) cited on page 17
- [52] París, J., Navarrina, F., Colominas, I., and Casteleiro, M., 'Block aggregation of stress constraints in topology optimization of structures', *Advances in Engineering Software*, Advances in optimum engineering design 41.3 (Mar. 2010), pp. 433–441.
DOI: [10.1016/j.advengsoft.2009.03.006](https://doi.org/10.1016/j.advengsoft.2009.03.006) cited on page 17

- cited on page 17
- [53] Norato, Julián A., Smith, Hollis A., Deaton, Joshua D., and Kolonay, Raymond M., 'A maximum-rectifier-function approach to stress-constrained topology optimization', *Structural and Multidisciplinary Optimization* 65.10 (Sept. 2022), p. 286.
doi: [10.1007/s00158-022-03357-z](https://doi.org/10.1007/s00158-022-03357-z)
- cited on page 19
- [54] Lewiński, T., Zhou, M., and Rozvany, G. I. N., 'Extended exact solutions for least-weight truss layouts—Part I: Cantilever with a horizontal axis of symmetry', *International Journal of Mechanical Sciences* 36.5 (1994), pp. 375–398.
doi: [10.1016/0020-7403\(94\)90043-4](https://doi.org/10.1016/0020-7403(94)90043-4)
- cited on page 22
- [55] Munro, Dirk and Groenwold, Albert, 'Local stress-constrained and slope-constrained SAND topology optimisation', *International Journal for Numerical Methods in Engineering* 110.5 (May 2017), pp. 420–439.
doi: [10.1002/nme.5360](https://doi.org/10.1002/nme.5360)
- cited on pages 26, 31
- [56] Reinschmidt, Kenneth F. and Russell, Alan D., 'Applications of linear programming in structural layout and optimization', *Computers & Structures* 4.4 (Aug. 1974), pp. 855–869.
doi: [10.1016/0045-7949\(74\)90049-2](https://doi.org/10.1016/0045-7949(74)90049-2)
- cited on pages 26, 29
- [57] Kirsch, Uri, 'Optimal design of trusses by approximate compatibility', *Computers & Structures* 12.1 (July 1980), pp. 93–98.
doi: [10.1016/0045-7949\(80\)90097-8](https://doi.org/10.1016/0045-7949(80)90097-8)
- cited on page 26
- [58] Oberndorfer, J. M., Achtziger, W., and Hornlein, H. R. E. M., 'Two approaches for truss topology optimization: a comparison for practical use', *Structural Optimization* 11.3-4 (June 1996), pp. 137–144.
doi: [10.1007/BF01197027](https://doi.org/10.1007/BF01197027)
- cited on page 26
- [59] Silva Smith, O., 'Topology optimization of trusses with local stability constraints and multiple loading conditions?a heuristic approach', *Structural Optimization* 13.2-3 (Apr. 1997), pp. 155–166.
doi: [10.1007/BF01199235](https://doi.org/10.1007/BF01199235)
- cited on pages 26, 27, 30
- [60] Achtziger, W., 'Local stability of trusses in the context of topology optimization Part I: Exact modelling', *Structural Optimization* 17.4 (Dec. 1999), pp. 235–246.
doi: [10.1007/BF01206999](https://doi.org/10.1007/BF01206999)
- cited on pages 26, 29, 42–44
- [61] Achtziger, W., 'Local stability of trusses in the context of topology optimization Part II: A numerical approach', *Structural optimization* 17.4 (Dec. 1999), pp. 247–258.
doi: [10.1007/BF01207000](https://doi.org/10.1007/BF01207000)
- cited on page 26
- [62] Stolpe, M., 'Global optimization of minimum weight truss topology problems with stress, displacement, and local buckling constraints using branch-and-bound', *International Journal for Numerical Methods in Engineering* 61.8 (2004), pp. 1270–1309.
doi: <https://doi.org/10.1002/nme.1112>

- [63] Pritchard, T., Gilbert, Matthew, and Tyas, Andrew, 'Plastic Layout Optimization of Large-Scale Frameworks Subject to Multiple Load Cases, Member Self-Weight and with Joint Length Penalties' (Jan. 2005). cited on page 26
- [64] Tyas, A., Gilbert, M., and Pritchard, T., 'Practical plastic layout optimization of trusses incorporating stability considerations', *Computers & Structures* 84.3 (Jan. 2006), pp. 115–126. doi: [10.1016/j.compstruc.2005.09.032](https://doi.org/10.1016/j.compstruc.2005.09.032) cited on pages 26, 27, 44
- [65] Descamps, Benoît and Filomeno Coelho, Rajan, 'The nominal force method for truss geometry and topology optimization incorporating stability considerations', *International Journal of Solids and Structures* 51.13 (June 2014), pp. 2390–2399. doi: [10.1016/j.ijsolstr.2014.03.003](https://doi.org/10.1016/j.ijsolstr.2014.03.003) cited on page 26
- [66] Schwarz, Jonas, Chen, Tian, Shea, Kristina, and Stanković, Tino, 'Efficient size and shape optimization of truss structures subject to stress and local buckling constraints using sequential linear programming', *Structural and Multidisciplinary Optimization* 58.1 (July 2018), pp. 171–184. doi: [10.1007/s00158-017-1885-z](https://doi.org/10.1007/s00158-017-1885-z) cited on pages 26, 32
- [67] Cai, Qi, Feng, Ruoqiang, and Zhang, Zhijie, 'Topology optimization of trusses incorporating practical local buckling stability considerations', *Structures* 41 (July 2022), pp. 1710–1718. doi: [10.1016/j.istruc.2022.05.109](https://doi.org/10.1016/j.istruc.2022.05.109) cited on page 26
- [68] Cheng, G., 'Some aspects of truss topology optimization', *Structural Optimization* 10.3-4 (Dec. 1995), pp. 173–179. doi: [10.1007/BF01742589](https://doi.org/10.1007/BF01742589) cited on page 27
- [69] Guo, X., Cheng, G., and Yamazaki, K., 'A new approach for the solution of singular optima in truss topology optimization with stress and local buckling constraints', *Structural and Multidisciplinary Optimization* 22.5 (Dec. 2001), pp. 364–373. doi: [10.1007/s00158-001-0156-0](https://doi.org/10.1007/s00158-001-0156-0) cited on pages 27, 39, 40
- [70] Stolpe, M. and Svanberg, K., 'A note on stress-constrained truss topology optimization', *Structural and Multidisciplinary Optimization* 25.1 (Mar. 2003), pp. 62–64. doi: [10.1007/s00158-002-0273-4](https://doi.org/10.1007/s00158-002-0273-4) cited on pages 27, 39, 40
- [71] Bendsøe, Martin P., 'Optimization of Structural Topology, Shape, and Material'. Berlin, Heidelberg: Springer Berlin Heidelberg, 1995.
ISBN: [978-3-662-03117-9 978-3-662-03115-5](https://doi.org/10.1007/978-3-662-03117-9_978-3-662-03115-5) cited on page 27
- [72] Zhou, M., 'Difficulties in truss topology optimization with stress and local buckling constraints', *Structural optimization* 11.2 (Apr. 1996), pp. 134–136. doi: [10.1007/BF01376857](https://doi.org/10.1007/BF01376857) cited on page 27

- cited on page 27
- [73] Rozvany, G. I. N., 'Difficulties in truss topology optimization with stress, local buckling and system stability constraints', *Structural optimization* 11.3 (June 1996), pp. 213–217.
DOI: [10.1007/BF01197036](https://doi.org/10.1007/BF01197036)
- cited on page 27
- [74] Ben-Tal, Aharon, Jarre, Florian, Kočvara, Michal, Nemirovski, Arkadi, and Zowe, Jochem, 'Optimal Design of Trusses Under a Nonconvex Global Buckling Constraint', *Optimization and Engineering* 1.2 (July 2000), pp. 189–213.
DOI: [10.1023/A:1010091831812](https://doi.org/10.1023/A:1010091831812)
- cited on page 27
- [75] Kočvara, M., 'On the modelling and solving of the truss design problem with global stability constraints', *Structural and Multidisciplinary Optimization* 23.3 (Apr. 2002), pp. 189–203.
DOI: [10.1007/s00158-002-0177-3](https://doi.org/10.1007/s00158-002-0177-3)
- cited on page 27
- [76] Neves, M. M., Rodrigues, H., and Guedes, J. M., 'Generalized topology design of structures with a buckling load criterion', *Structural optimization* 10.2 (Oct. 1995), pp. 71–78.
DOI: [10.1007/BF01743533](https://doi.org/10.1007/BF01743533)
- cited on page 27
- [77] Ferrari, Federico, Sigmund, Ole, and Guest, James K., 'Topology optimization with linearized buckling criteria in 250 lines of Matlab', *Structural and Multidisciplinary Optimization* 63.6 (June 2021), pp. 3045–3066.
DOI: [10.1007/s00158-021-02854-x](https://doi.org/10.1007/s00158-021-02854-x)
- cited on page 27
- [78] Mela, Kristo, 'Resolving issues with member buckling in truss topology optimization using a mixed variable approach', *Structural and Multidisciplinary Optimization* 50.6 (Dec. 2014), pp. 1037–1049.
DOI: [10.1007/s00158-014-1095-x](https://doi.org/10.1007/s00158-014-1095-x)
- cited on pages 29, 35
- [79] Kirsch, Uri, 'Optimal topologies of truss structures', *Computer Methods in Applied Mechanics and Engineering* 72.1 (Jan. 1989), pp. 15–28.
DOI: [10.1016/0045-7825\(89\)90119-9](https://doi.org/10.1016/0045-7825(89)90119-9)
- cited on pages 29, 35
- [80] Rozvany, G. I. N., Bendsøe, M. P., and Kirsch, U., 'Layout Optimization of Structures', *Applied Mechanics Reviews* 48.2 (Feb. 1995), pp. 41–119.
DOI: [10.1115/1.3005097](https://doi.org/10.1115/1.3005097)
- cited on page 29
- [81] Kirsch, Uri, 'Effect of Compatibility and Prestressing on Optimized Trusses', *Journal of Structural Engineering* 115.3 (Mar. 1989), pp. 724–737.
DOI: [10.1061/\(ASCE\)0733-9445\(1989\)115:3\(724\)](https://doi.org/10.1061/(ASCE)0733-9445(1989)115:3(724))
- cited on pages 37, 56
- [82] Moore, Jason; K. and Mechmotum, 'cyipopt: Cython interface for the interior point optimizer IPOPT', 2018.
URL: <https://github.com/mechmotum/cyipopt>

- [83] Wächter, Andreas and Biegler, Lorenz T., 'On the implementation of an interior-point filter line-search algorithm for large-scale nonlinear programming', *Mathematical Programming* 106.1 (Mar. 2006), pp. 25–57.
doi: [10.1007/s10107-004-0559-y](https://doi.org/10.1007/s10107-004-0559-y)
- [84] Alappat, Christie, Basermann, Achim, Bishop, Alan R., Fehske, Holger, Hager, Georg, Schenk, Olaf, Thies, Jonas, and Wellein, Gerhard, 'A Recursive Algebraic Coloring Technique for Hardware-efficient Symmetric Sparse Matrix-vector Multiplication', *ACM Transactions on Parallel Computing* 7.3 (2020), 19:1–19:37.
doi: [10.1145/3399732](https://doi.org/10.1145/3399732)
- [85] Stragiotti, Enrico, 'Truss Topology Optimization with Topological Buckling Constraints Data Set', May 2023.
doi: [10.17632/BW7XB2W6ST.1](https://doi.org/10.17632/BW7XB2W6ST.1)
, URL: <https://data.mendeley.com/datasets/bw7xb2w6st/1>
- [86] Rozvany, George I. N., 'On symmetry and non-uniqueness in exact topology optimization', *Structural and Multidisciplinary Optimization* 43.3 (Mar. 2011), pp. 297–317.
doi: [10.1007/s00158-010-0564-0](https://doi.org/10.1007/s00158-010-0564-0)
- [87] Guo, Xu, Du, Zongliang, and Cheng, Gengdong, 'A confirmation of a conjecture on the existence of symmetric optimal solution under multiple loads', *Structural and Multidisciplinary Optimization* 50.4 (Oct. 2014), pp. 659–661.
doi: [10.1007/s00158-014-1089-8](https://doi.org/10.1007/s00158-014-1089-8)
- [88] Stragiotti, Enrico, Irisarri, François-Xavier, Julien, Cédric, and Morlier, Joseph, 'Enhanced truss topology optimization (TTO) applied to a cellular wing box', *ASMO-UK 12 / ASMO-Europe 1 / ISSMO Conference on Engineering Design Optimization* (2022), Leeds, United Kingdom, July 2022.
- [89] Cramer, Nicholas B., Cellucci, Daniel W., Formoso, Olivia B., Gregg, Christine E., Jenett, Benjamin E., Kim, Joseph H., Lendraitis, Martynas, Swei, Sean S., Trinh, Greenfield T., Trinh, Khanh V., and Cheung, Kenneth C., 'Elastic shape morphing of ultralight structures by programmable assembly', *Smart Materials and Structures* 28.5 (Apr. 2019), p. 055006.
doi: [10.1088/1361-665X/ab0ea2](https://doi.org/10.1088/1361-665X/ab0ea2)
- [90] Zhou, Shiwei and Li, Qing, 'Design of graded two-phase microstructures for tailored elasticity gradients', *Journal of Materials Science* 43.15 (Aug. 2008), pp. 5157–5167.
doi: [10.1007/s10853-008-2722-y](https://doi.org/10.1007/s10853-008-2722-y)
- [91] Kalamkarov, Alexander L., Andrianov, Igor V., and Danishevskyy, Vladyslav V., 'Asymptotic Homogenization of Composite Materials and Structures', *Applied Mechanics Reviews* 62.3 (Mar. 2009).
doi: [10.1115/1.3090830](https://doi.org/10.1115/1.3090830)

cited on page 51

- [92] Li, Dawei, Liao, Wenhe, Dai, Ning, and Xie, Yi Min, 'Anisotropic design and optimization of conformal gradient lattice structures', *Computer-Aided Design* 119 (Feb. 2020), p. 102787.
DOI: [10.1016/j.cad.2019.102787](https://doi.org/10.1016/j.cad.2019.102787)

cited on page 51

- [93] Wu, Jun, Sigmund, Ole, and Groen, Jeroen P., 'Topology optimization of multi-scale structures: a review', *Structural and Multidisciplinary Optimization* (Mar. 2021).
DOI: [10.1007/s00158-021-02881-8](https://doi.org/10.1007/s00158-021-02881-8)

cited on page 66

- [94] Deshpande, V. S., Fleck, N. A., and Ashby, M. F., 'Effective properties of the octet-truss lattice material', *Journal of the Mechanics and Physics of Solids* 49.8 (Aug. 2001), pp. 1747–1769.
DOI: [10.1016/S0022-5096\(01\)00010-2](https://doi.org/10.1016/S0022-5096(01)00010-2)